MINING MACHINES

2022

volume 40, Issue 4

Quarterly of Science and Technology

e-ISSN 2719-3306

MINING MACHINES

2022, Vol. 40 Issue 4

CONTENTS:

e-ISSN 2719-3306

Quarterly of Science and Technology

December 2022

Publishers and contact

KOMAG Institute of Mining Technology
Pszczyńska 37, 44-101 Gliwice, POLAND

E-mail of Editorial Office: miningmachines@komag.eu

Editor–in–Chief
phone: +48 32 2374600
e-mail: dprostanski@komag.eu

Managing Editor
phone: +48 32 2374612
e-mail: mmacina@komag.eu

http://komag.eu/publications/mining-machines/editorial-office

https://doi.org/10.32056/KOMAG2022.4.1

The effect of the main component ratios in the joint filling on the product quality

Received: 18.08.2022

Accepted: 30.11.2022

Published online: 30.12.2022

Author's affiliations and addresses:

[1] Kahramanmaraş Sütçü İmam University, Department of Geological Engineering, Avşar Kampüsü, TR-46100 Kahramanmaraş, Turkey

*** Correspondence:**

e-mail: tamerrizaoglu@gmail.com

Tamer RIZAOĞLU [1*], Muhammed Ziya KARATAŞ [1], Canberk ÇOŞKUN [1]

Abstract:

When building materials are exposed to environmental and natural factors such as temperature differences, humidity, strong wind and earthquake in the areas where they are applied, irreversible damages such as separation, cracking and level difference occur in structures and building materials. In order to prevent these damages, the joints are left between the building materials and the gaps are filled with filling materials. The composition of the materials filling the joint gaps is also very important. The most important problems encountered in joint fillings are rupture, cracking and therefore permeability. In this study, it is aimed to compare the joint filling materials produced from different proportions of aggregate and white cement against rupture and cracking, and to determine the mixture ratio that exhibits the best performance. Five different recipes were prepared by using calcite powder as aggregate, white Portland cement as binder and water-repellent, volumizing and thickening chemical additives as auxiliary materials. On the prepared test samples; Capillary water absorption, water absorption by weight and volume, unit volume weight, saturated unit volume weight, porosity, compressive strength, bending strength, surface hardness and abrasion resistance tests were carried out. Considering the cost and environmental damage of cement, which is one of the main components in joint filler material, DD2 [Calcite (71.50%)] + White Cement (26.50%) + [Polymer + Cellulose + Plasticizer + Silicone] 2% has been detected as the most appropriate recipe.

Keywords: cement, joint filling, calcite, building materials

1. Introduction

Throughout the history of humanity, the level of use of industrial raw materials has been an indicator of the level of development and welfare of all societies. As a result of its geological position, Turkey is one of the few countries that can meet most of its industrial raw material needs in terms of diversity and reserves. Turkey ranks 28th in the world in mineral production and 10th in the variety of minerals produced [1]. While 13 of the 90 types of mines traded in the world have not been found in Turkey, it is known that 50 of the remaining mines are quite rich or rich as reserves. Nearly 30 mines have insufficient resources in terms of reserves. Turkey is one of the countries rich in marble, boron, magnesite, pumice, gypsum, perlite and calcite [1].

Calcite is used as an industrial raw material in many fields such as construction, paper, plastic pipes, paint industry, glass, agriculture and medicine. There are three characteristics that define the quality of ground calcium carbonate (GCC), which is used as an industrial mineral, namely grain diameter, colour and chemical purity [2, 3]. The purest whiteness in Turkish calcite deposits was determined in the fields located in the Niğde region. It was also used in this study [4, 5]. A joint is a discontinuity between continuities [6]. In ceramics and similar construction materials, changes in volume (expansion-contraction) may occur in the face of temperature differences, humidity, changing weather conditions and physical effects (earthquake effect-mechanical effects-deformation stresses). Therefore, they should definitely be laid with joints in order not to encounter irreversible or even costly consequences [7, 8]. In addition to leaving joints in ceramic coatings, the material used together with the method of application is also an important factor. Otherwise, if the joint gaps are filled with inflexible white cement and similar hard materials without additives, this will have an effect on the building materials in the coating as if they were laid without joints [9]. In order to obtain positive results, in addition to the cement-based filling materials, performance, workability, resistance to cracking, permanent colour due to the chemicals it contains and smooth surface should be preferred [10]. Joint fillers with anti-bacterial properties should be chosen for wet areas. They offer different characteristics according to the regions for cold and hot climates [11, 12]. The main objective of the study is to determine the most accurate ratio, to contribute calcite, which is abundant in nature, to the economy, and to reduce the use of environmentally undesirable cement.

2. Materials

Calcite, which is one of the main components of the filling material used between the joints of the ceramics, which is the floor covering material used in the buildings, was supplied in ground form from Niğtaş company in Niğde-Turkey to be used within the scope of the study. PÇ 52.5 was preferred as the white Portland cement used as the binder and it was obtained from Çimsa company (Fig. 1). Construction chemicals that provide water repellent, thickener and cause impermeability were supplied by the intermediary firm in Kahramanmaraş city (Fig. 1).

Fig. 1. Materials used in combinations

Publisher: **KOMAG Institute of Mining Technology, Poland**

3. Methods

3.1. Determining the mixing ratios

In this study, 24%, 26.5%, 29%, 31.5%, 34% of white cement were added to the total mixture in order to determine the most appropriate ratio of calcite used as aggregate and white cement used as binder in the production of ceramic grouting material. DD1, DD2, DD3, DD4, DD5 samples were prepared (Table 1). In addition to white cement and calcite, in order to obtain the appropriate mixture, polymer as water repellent, cellulose volumizer, plasticizer as thickener and silicone (CA-30) for impermeability were added to the mixture in total 2% (Table 1).

Table 1. The combinations for the prepared joint filler samples

Sample No	Ingredients
DD-1	Calcite (74.00%) + White Cement (24.00%) + [Polymer+Cellulose+Plasticizer+Silicone (2%)]
DD-2	Calcite (71.50%) + White Cement (26.50%) + [Polymer+Cellulose+Plasticizer+Silicone (2%)]
DD-3	Calcite (69.00%) + White Cement (29.00%) + [Polymer+Cellulose+Plasticizer+Silicone (2%)]
DD-4	Calcite (66.50%) + White Cement (31.50%) + [Polymer+Cellulose+Plasticizer+Silicone (2%)]
DD-5	Calcite (64.00%) + White Cement (34.00%) + [Polymer+Cellulose+Plasticizer+Silicone (2%)]

3.2. Sample preparation

Within the scope of joint filler production, white cement, calcite (calcite grain size 100 μ and below) polymer, cellulose, plasticizer and silicone were prepared in the proportions as given in Table 1 and mixed with a mixer to make it homogeneous (Fig. 2a). Then, water was added at a constant rate and mixed with white cement acting as a binder and calcite materials used as aggregate until a homogeneous image was obtained (Fig. 2b). In order to obtain a correct mixture into this homogeneous mortar obtained, water-repellent polymer, cellulose as a volumizer, fluid as a thickener and additionally some silicone to prevent lumps were added to the mixture (Fig. 2c÷d).

Fig. 2. Sample preparation: a) mixing calcite and white cement, b) adding water, c) adding chemicals, d) homogenous mixing of ingredients, e) preparation of molds, f) placing the mixture in the mold

Publisher: **KOMAG Institute of Mining Technology, Poland**

Finally, the joint filler obtained in a homogeneous form was lubricated during the stage of putting the mortar into the mold according to TS EN 12808 Part 3 [13] so that the samples could come out of the mold without any damage (Fig. 2e). In order for the mortar to be completely filled into the mold without any air gaps, the samples were placed with use of the shaking table. The rough surface in the upper part of the mold was removed with the help of a spatula to obtain a flat surface (Fig. 2f). The samples, which were left to dry, were carefully removed from the inserts of the test molds without damaging them after 24 hours.

3.3. Testing Methods

In order to determine some physical and mechanical properties of the joint filler samples obtained at different rates, the samples required for the planned experiments were prepared as required according to TS EN 12808 (2010) (Table 1). All the obtained test samples were subjected to tests after they had been kept in the laboratory environment for 28 days in order to make them usable in the experiments.

3.3.1. Unit volume weight and water absorption

Within the scope of the study, the weight found as a result of drying of the samples obtained for the determination of unit volume weights (UVW) was calculated as W_1. The values obtained by measuring the dimensions of the test samples with a caliper are used in the volume calculation. Unit volume weight and water saturated unit volume weights were calculated according to the equation below.

$$UVW = W_1/V \text{ kg/cm}^3$$

In order to find the amount of water absorption by the samples, that were kept in the laboratory environment for 28 days, were put in an oven at 105° to dry and kept for one day, and then the dried samples were weighed and named as dry weight and W_{dry} was obtained. Then, the samples were left in the curing pool and the samples that were in the water for 24 hours were removed and named as saturated weight, and the W_{sat} was determined. In order to calculate the water absorption by volume, in other words the porosity, the volumes of the samples were calculated with a caliper and expressed as V. Water absorption percentage was calculated by substituting W (%) in the equations below.

$$\text{Water absorption by weight (\%)} = [(W_{sat}-W_{dry}) / W_{sat}] \times 100$$

$$\text{Water absorption by volume (\%)} = [(W_{sat}-W_{dry}) / V] \times 100$$

The samples taken for capillary water absorption test are made in order to determine how much water is absorbed by the sample, which is kept in water for the periods determined according to TS EN 12808 Part 5 [14] (30 min, 240 min). The first weight measurement of the samples was made with use of precision scales and recorded. After the weight measurement, 5 mm and 10 mm markings were made on the clean surface of the samples, which was smoothed with a spatula. Then, the samples were brought into contact with water up to a minimum of 5 mm with the marked surface facing down, and after waiting for 30 minutes, they were removed and the wet surface of the samples was wiped with a cloth and the measurements were taken again with use of precision scales. The sample was put back into the water and kept in water for another 210 minutes to complete 240 minutes, and the experiment was completed by taking the weight values in the same way.

3.3.2. Böhme abrasion test

The wear resistance determination of the joint filler samples, obtained in this study, was carried out according to the standards in the Böhme abrasion test TS 699 [15, 16]. Five samples, representing the mixture for each group, were cut into cubes with a side length of 71 ± 1.5 mm in accordance with mentioned standard and produced with a base area of 50 cm². The Böhme abrasion test is to determine the volume loss that occurs as a result of 16 cycles consisting of a total of 22 cycles by pouring corundum (crystalline Al_2O_3) powder as an abrasive on a rotating steel disc and exposing the sample placed on the rotary table to the pressure of 0.06 N/mm² on the contact surface area.

As the first step, the weights of the samples to be tested are calculated using precision scales (Fig. 3a). Then, 20 ± 0.5 g of abrasive powder are added evenly in a circle on the friction path of the test device (Fig. 3b). The sample to be tested is placed in its slot on the test device and the device is set to run for 22 cycles. The experiment is started, and when the number of cycles is completed, the rotating disc stops automatically, thus completing the 1st cycle (Fig. 3b). The test samples are rotated to 90 degrees and continued until 4 cycles are completed. The test is completed by making 352 cycles in total. Afterwards, the samples are cleaned with a brush without being damaged and then weighed. The obtained values are calculated according to the following formula [15, 16].

$$\text{Abrasion resistance } (cm^3/50cm^2) = \frac{\text{Weight loss after 352 cycles}}{\text{Unit volume weight}}$$

3.3.3. Bending strength

The bending strength of the obtained joint filler materials was determined on samples with dimensions of 40x40x160 mm according to the standard TS EN 12808 Part 3 [13]. The tests were carried out by applying the 50 N load with the "Zwick/ 2010 Universal Test" device, which can perform bending, tensile and compression tests with a capacity of 20 kN. Bending strength was measured by mid-point loading method, adjusting the support span to be 2.5 times the sample height on average. The tests also consisted of 5 repetitions and the averages were taken (Fig. 3c).

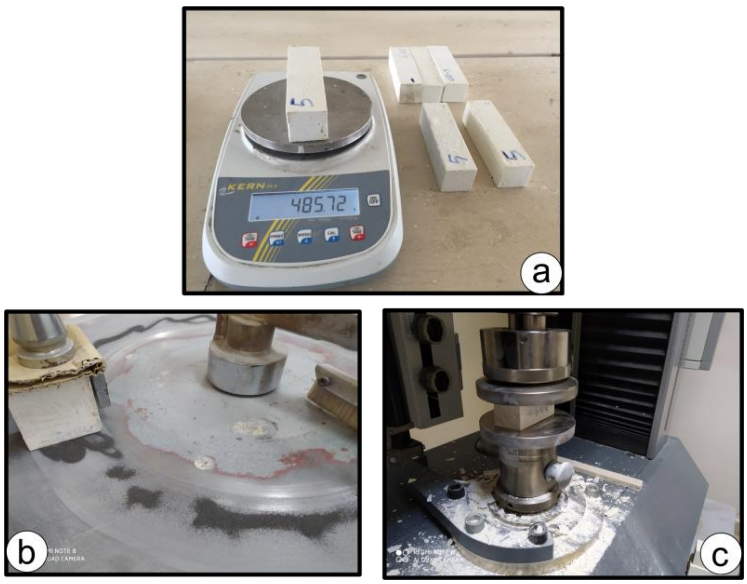

Fig. 3. a) Weighing of samples, b) Böhme abrasion test, c) Bending-compressing strength test

3.3.4. Compressive strength

The samples to be used for the compressive strength test were selected from the pieces that were broken during the bending test, larger than 4×4×4 cm. The loading speed of the samples, placed between the compression jaws, which is the special accessory of the Zwick Roell/2010 Universal Tester, was determined as 2400 N per second. The compressive strength test of the obtained joint fillers was carried out in accordance with TS EN 12808 (2010) Part 3. An analysis was carried out on 5 samples for each combination of the material compiled in accordance with the standard (Fig. 3c).

4. Discussion and results

All of the tests were carried out according to the TS EN 12808 (2010) standard, and the required value ranges according to the aforementioned standard are given in Table 2.

Publisher: **KOMAG Institute of Mining Technology, Poland**

Table 2. Required value ranges in TS EN 12808 (2010) standard for joint filler tests

Experiments	Standard Values	TSE Standard
Water absorption (30 minutes)	≤ 5 g	EN 12808-5
Water absorption (240 minutes)	≤ 10 g	EN 12808-5
Abrasion resistance	≤ 2000 mm^3	EN 12808-2
Shrinkage	≤ 3 mm/m	EN 12808-4
Surface hardness	≥ 40	EN 12808-3
Bending strength	≥ 2.5 N/mm^2	EN 12808-3
Compressive strength	≥ 15 N/mm^2	EN 12808-3

Unit volume weight (BHA) and saturated unit volume weight (DBHA) values of joint fillers are given in Fig. 4, respectively. The specific gravity tests performed on the blocks, on the other hand, were obtained from the DD5 sample with the highest as 1.51 g/cm^3; the lowest value was measured from the samples 1.43 g/cm^3 from DD1 sample (Table 3, Fig. 4).

Table 3. Unit volume weight and water absorption tests results

	Unit volume weight	Saturated Unit volume weight	Water absorption by weight			Water absorption by volume	Capillary water absorption	
			30 minutes	240 minutes	24 hours	24 hours	30 minutes	240 minutes
Standard	*	*	*	*	*	*	5 g	10 g
DD-1	1.43	1.79	16.97	22.42	26.92	38.57	6.2	10.3
DD-2	1.44	1.82	15.44	21.72	25.72	38.41	5.7	9.7
DD-3	1.46	1.84	15.05	20.83	25.57	38.32	4.9	9.3
DD-4	1.48	1.86	14.37	20.04	25.33	38.21	4.6	9.1
DD-5	1.51	1.88	13.59	19.42	24.18	37.98	4.1	8.8

It was observed that the specific gravity increased with the increase of the white cement ratio, while the unit weight values decreased with the increase of the calcite ratio acting as aggregate. When the water-saturated unit volume weights are examined, parallel values with the unit volume weight were observed (Table 3, Fig. 4).

A decrease was observed in the water absorption values of 30 minutes, 240 minutes and 24 hours, respectively, as regards DD1 to DD5, as the amount of cement increased. The maximum water absorption value at the end of 24 hours was 26.92% in DD1, and the minimum was 24.18% in DD5. The water absorption values by volume were measured as 38.57%, 38.41%, 38.32%, 38.21% and 37.98%, respectively, as regards DD1 to DD5. It was observed that the porosity decreased as the specific gravity values of the materials increased depending on the amount of cement (Table 3, Fig. 5).

Publisher: **KOMAG Institute of Mining Technology, Poland**

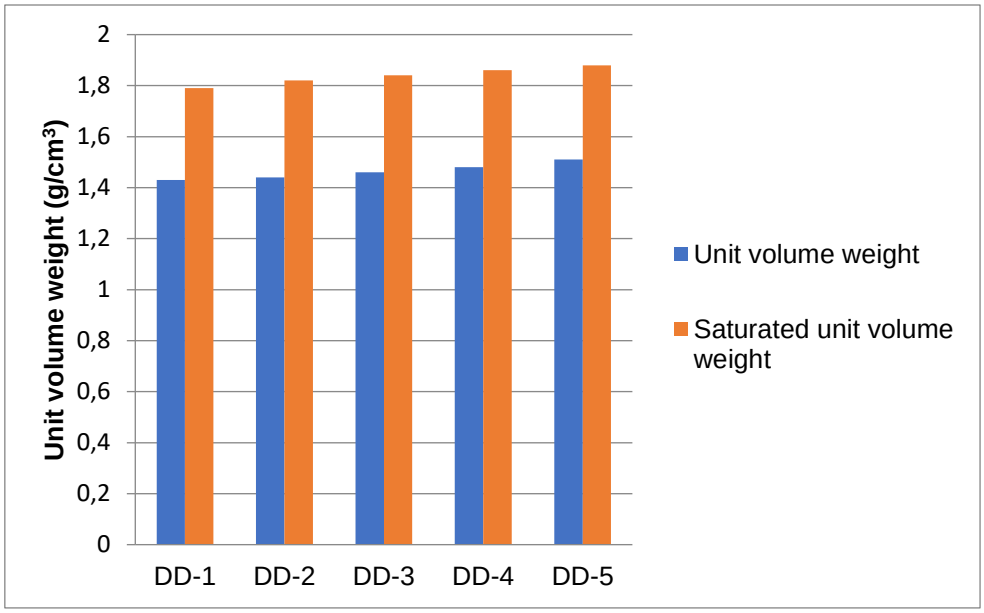

Fig. 4 Unit volume weight of the samples

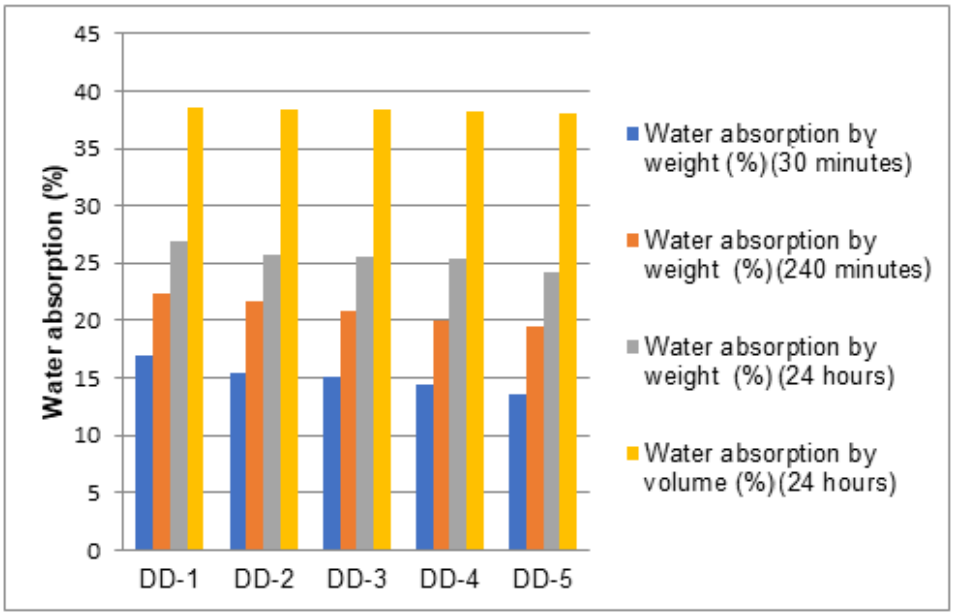

Fig. 5. Water absorption by weight and volume water absorption of the samples

The capillary water absorption rate is a parameter of primary importance in the case of joint filling materials, which is the main subject of this study, and the tests were carried out as specified in TS EN 12808 (2010). It is requested that the capillary water absorption value should not exceed 5 grams within 30 minutes and 10 grams within 240 minutes (Table 2). In Fig. 6, the relationships between DD1 and DD5 water absorption in the joint filling material within 30 minutes and 240 minutes are presented graphically. It was observed that the water absorption amount did not exceed the critical values, except for DD1 and DD2 after 30 minutes, and except for DD1 after 240 minutes. After the obtained joint filling mortars were used in the application area, solidified and hardened, an increase of the cement ratio by reducing the calcite ratio of the total volume significantly increased the capillary water absorption value (Table 3, Fig. 6). By increasing the calcite utilization rate, the water absorption rate of the final product will increase.

Publisher: **KOMAG Institute of Mining Technology, Poland**

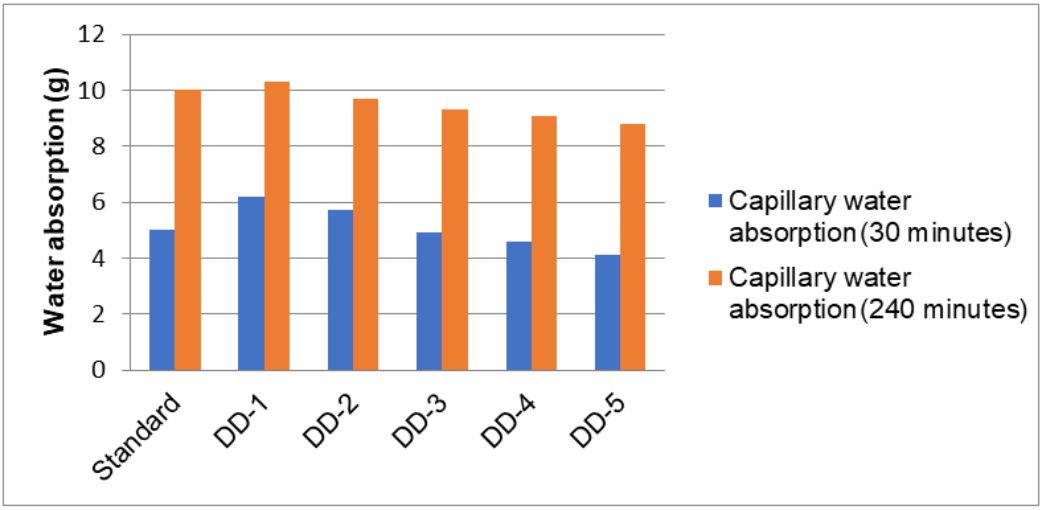

Fig. 6. Capillary water absorption of the samples

Table 4. Abrasion resistance, bending resistance and compressive strength results

	Abrasion resistence		Bending strength			Compressive strength		
	Weight loss (g)	Abrasion resistance ($cm^3/50cm^2$)	3 day	7 day	28 day	3 day	7 day	28 day
Standard	*	*	*	*	2.5	*	*	15.0
DD-1	11.33	31.69	1.88	2.4	3.29	9.31	11.1	15.13
DD-2	7.44	20.64	2.01	2.66	3.78	10.23	12.6	16.61
DD-3	6.84	18.72	2.21	2.87	3.99	12.35	13.9	16.92
DD-4	5.88	15.88	2.29	3.01	4.11	13.13	16.1	18.29
DD-5	4.71	12.44	2.98	3.32	5.12	14.67	17.2	19.91

In Fig. 7, the relationships between the abrasion resistance of the joint filler material and the weight loss are given. While the highest amount of wear was 11.33 g in the DD1 sample, the lowest amount of wear was measured as 4.71 g in the DD5 sample. Abrasion resistances were determined as 7.92, 5.16, 4.68, 3.97, 3.11 in samples DD1, DD2, DD3, DD4 and DD5, respectively. Considering this situation, it is seen that a more durable joint filling material is obtained in terms of abrasion resistance when the calcite ratio in the joint filler material is decreased and the cement ratio is increased (Table 4, Fig. 7).

Publisher: **KOMAG Institute of Mining Technology, Poland**

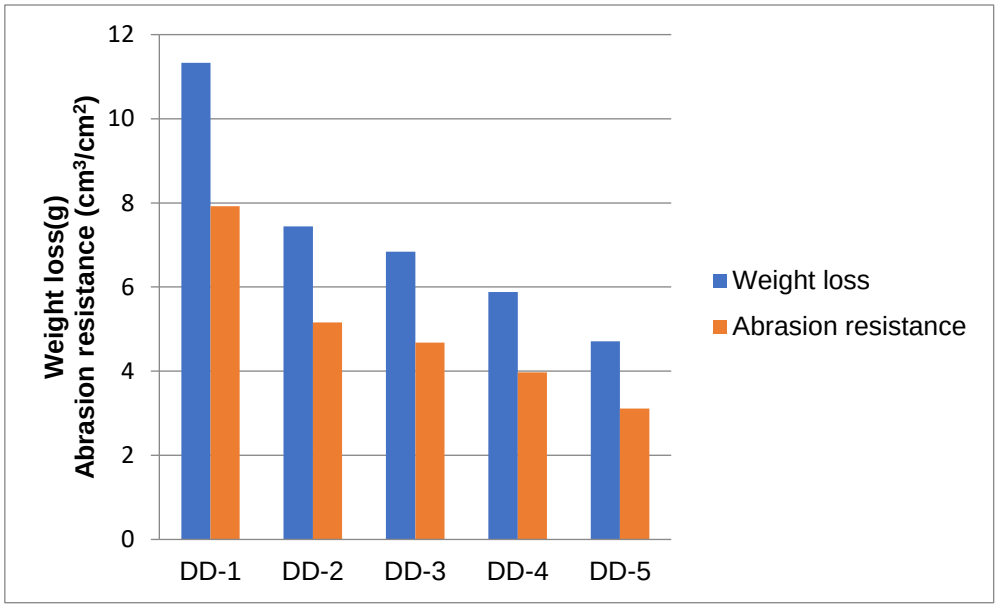

Fig. 7. Abrasion resistance test results of the samples

The results of the bending strength tests are given in Table 4. The tensile strength after 3, 7 and 28 days of bending in the obtained joint filler samples are given in Fig. 8.

According to TS EN 12808 standard, joint filler materials after 28 days are required to have the bending strength of at least 2.5 MPa. According to the results from the 3-day test samples, only DD5 ≥ 2.5 MPa is above the threshold. According to the 7-day test results, all samples except DD1 are within the required range in the standard, and according to the 28-day results, it is observed that all samples are within the required value in the standard. At the end of 28 days, the lowest bending strength was 3.29 MPa in the case of DD1; the highest bending strength value was 5.12 MPa in the case of DD5 (Table 4, Fig. 8).

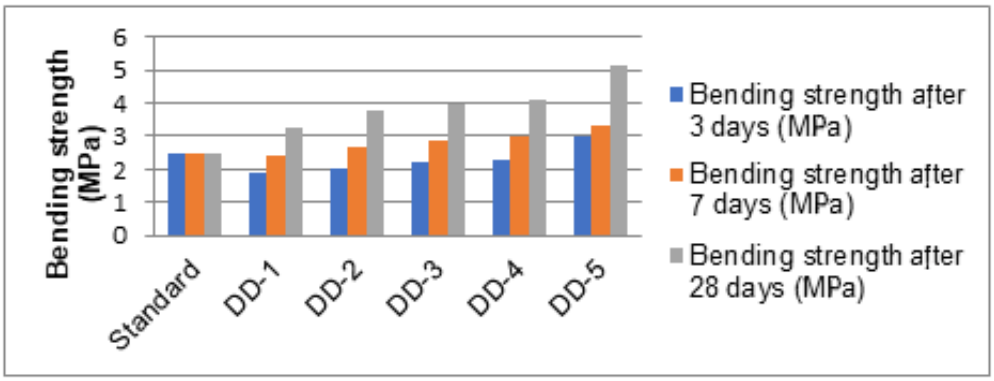

Fig. 8. Bending strength of the samples

As in the case of the bending strength tests, tests on compressive strength were carried out in accordance with Part 3 of TS EN 12808 [13]. Accordingly, the compressive strength of the joint filling material is required to be ≥ 15 MPa or more (Table 2). Compressive strength results after 3 and 7 days for DD1, DD2, DD3, DD4 and DD5 were 9.31÷11.05 MPa, 10.23÷12.62 MPa, 12.35÷13.87 MPa, 13.13÷16.11 MPa and 14.67÷17.24 MPa obtained respectively. For the same samples the 28-day compressive strength values were obtained as 15.13 MPa, 16.61 MPa, 16.92 MPa, 18.29 MPa and 19.91 MPa respectively.

In the case of the 3-day test results, none of the samples are within the required range, while after 7 days DD3 (16.11) and DD4 (17.24) are within the required ranges. According to the 28-day test results,

all of the samples except DD1 are in the range of values (≥ 15 MPa) required in the standard (Fig. 9, Table 4).

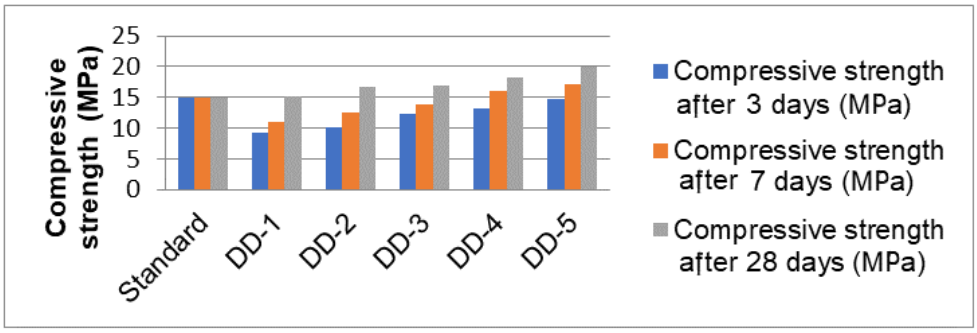

Fig. 9. Compressive strength of the samples

5. Conclusions

As conclusions:

- With the decrease of calcite in the total mixture ratio and the increase of cement, the unit volume weight and saturated unit volume weight values increased, and the water absorption values by weight and volume decreased inversely.
- Considering capillary water absorption, since reducing the use of cement in the joint filling material is among the primary objectives of the study, it can be concluded that the most ideal example was DD3 after 30 minutes and DD2 after 240 minutes; a better joint filling material can be obtained in terms of water absorption.
- An increase of the cement ratio in the mixture increased the wear resistance and it was observed that the sample with the highest wear resistance was DD5.
- According to the 28-day bending test results, it was observed that all the samples were within the required value in the standard, while the 28-day compressive strength was found to be within the required (≥ 15 MPa) values in the standard, except for DD1.
- Even if the sample DD5 gave the best results in compressive strength and bending strength, it would be correct to say that the sample with the most appropriate ratio was DD2, considering the determination of the correct ratios.
- In this study, the use of excess cement was prevented and positive results were obtained both in economic and environmental terms.
- Although it is very important to choose the correct component ratios in the joint filler material, it should be ensured that it contains less water in the mixture by using either direct impermeability additives or water-repellent chemical additives, and thus special joint fillers can be produced.

Acknowledgements

The authors thank Hasan KARAOKUR, who assisted in the procurement of raw materials, Prof. Dr. Hüseyin TEMİZ for allowing them to use the laboratory facilities of Kahramanmaraş Sütçü İmam University, Civil Engineering Department during the sample production process, and managers and staff of the University Industry and Public Cooperation Center (ÜSKİM) Laboratories of KSU for making the experiments possible.

References

[1] ETKB (2014). Enerji ve Tabii Kaynaklar Bakanlığı (ETKB) ile Bağlı, İlgili ve İlişkili Kuruluşların Amaç ve Faaliyetleri, p.302

[2] DPT (2001). Madencilik Özel İhtisas Komisyonu Raporu, Endüstriyel Hammaddeler Alt Komisyonu Genel Endüstri Mineralleri I, 8. Kalkınma Planı, Yayın No: 2618, ISBN 975- 19-2853-2

[3] Şahin, N. (2008). Kalsit Hakkında Bazı Bilgiler. Madencilik Bülteni, 86, pp. 48-5

[4] Delibalta, M.S. (2009). Niğde Ekonomisinde Kalsit ve Endüstriyel Hammaddelerin Önemi.7. Uluslararası Endüstriyel Hammaddeler Sempozyumu ve Sergisi, TMMOB Maden Mühendisleri Odası Yayın No:152, pp. 207-212

[5] Uçurum, M. (2015).Kalsit Madenciliğinin Geleceğinde Optik Ayırma Teknolojilerinin Yeri ve Önemi. Niğde Üniversitesi Mühendislik Bilimleri Dergisi, 4, 1, pp.40-46

[6] Toydemir, N. (1988). Composite Construction Materials. J Compos Constr Compon Insul, *80*, pp. 39-43

[7] Chew, M.Y.L. (1999). Factors Affecting Ceramic Tile Adhesion for External Cladding. Construction and Building Materials,13, pp. 293-296

[8] Silvestre, J. and Brito, J. (2009). Ceramic Tiling İnspection System, Construction and Building Materials, 23, pp. 653–668

[9] Walters, W. (1992). Approaches To a Retrofit, Repair, Refurbishment Situation. Proceedings Conference On Adhesives Technology in The Architectural Application of Ceramic Tiles, Singapore Trade Link Media Pte. Lda

[10] Silvestre, J. And Brito, J. (2010). Inspection and Repair of Ceramic Tiling within a Building Management System. Journal of Materials in Civil Engineering, *22*(1), pp. 39-48

[11] Timellini, G. and Palmonari, C. (1989). Ceramic Floor And Wall Tile. Performance And Controversies. EdiCer, Sassuolo Italy

[12] Navarro, J. and Olmos, F. (2004). Ceramic Tiling As A System. Coding Proposal For Application in İnternal Tiling İn Building Construction. In Qualicer VIII World Congress on Ceramic Tile Quality, Vol. 3. pp. 163-176

[13] TS EN 12808-3, (2014). Derz dolgu malzemeleri – Karolar için – Bölüm 3: Eğilme ve basınç dayanımının tayini, Türk Standartları Enstitüsü, Ankara *(Grouts for tiles - Part 3: Determination of flexural and compressive strength)*

[14] TS EN 12808-5, (2014). Derz dolgu malzemeleri – Karolar için – Bölüm 5: Su emme tayini, Türk Standartları Enstitüsü, Ankara *(Grouts for tiles - Part 5: Determination of water absorption)*

[15] TS 2824 EN 1338. (2005). Zemin Döşemesi için Beton Kaplama Blokları Gerekli Şartlar ve Deney Metotları. TSE., Ankara *(Concrete paving blocks - Requirements and test methods)*

[16] DIN 52108 (2002). "Testing of Inorganic Non-Metallic Materials-Wear Test Using The Grinding Wheel According to Boehme-Grinding Wheel Method, Germany

Publisher: **KOMAG Institute of Mining Technology, Poland**

https://doi.org/10.32056/KOMAG2022.4.2

Technical analysis of fixed screen in coal extraction activities (case study: PT. MAL)

Received: 30.09.2022

Accepted: 07.12.2022

Published online: 30.12.2022

Author's affiliations and addresses:

[1] Mining Engineering Department, Faculty of Engineering, University of Sriwijaya, Palembang, Indonesia

*** Correspondence:**

e-mail: hasjimmachmud@gmail.com

Muhammad Faisal SEPRIZAL [1], Machmud HASJIM [1*], Restu JUNIAH [1]

Abstract:

The extraction of coal is one of the activities involved in mining operations, where drilling, blasting, milling, crushing, sizing, and screening of minerals are performed. At PT. MAL, Indonesia, this extraction activity involves in-pit processing, such as the sizing of coal using a fixed screen. This study aims to analyze the technical sectors regarding the use of fixed screens in coal production activities. This is carried out to reduce the production time and costs, as productivity is expected to increase and completely meet market demands. The challenges involved in the use of fixed screens influenced the availability value of coal. In this case, the use of availability (UA) and effective utilization (EU) values of the utilized excavator were insufficient. These conditions were due to the observation of many challenges in the coal extraction activities. The challenges also affected the performance and production of the excavator, where the solution emphasized the redesign of the fixed screen through the modification of several parameters, such as the angle of repose and screen capacity.

Keywords: extraction of coal, fixed screen, modification, sizing

1. Introduction

Downstream coal products are essential in the mining industry and consistent with the use of the mineral resource in other related sectors. In the steam power plant (PLTU) industry, the use of this mineral is also related to the forecast benefits produced by coal extraction activities. The demand for electricity and energy consumption is found to continue increasing in both developed and developing countries [1]. China, the United States of America (USA), India, Germany, Russia and Japan consume 76 percent of world's coal consumption for energy [2]. Meanwhile, the countries of the Asia-Pacific region are the main consumers of primary energy in the world, where about 44.8% of world energy consumption or 5,921 million toe [3]. Similarly, the need for electricity in the industrial, household and service sectors continues to increase in developing countries, to support socio-economic development activities. This shows that the world electricity generation is expected to continuously increase by 21.6, 25.8, and 36.5 trillion kilowatt-hours (T-kWh) in 2012, 2020, and 2040, respectively [4].

Indonesia has abundant reserves of medium and low-quality coal, as well as presently ranks 9th with approximately 2.2% of the total global reserves, based on the BP Statistical Review of World Energy. About 60% of the country's total reserves contain cheaper (sub-bituminous) and low-quality coal, which has a content of less than 0.0255 MJ/kg. Besides being exported to the giant markets of developing countries such as China and India, medium and low-quality coal is also domestically utilized as fuels for power plants, whose demand is continuously increasing. Based on PLN's recent Electricity Supply Business Plan, the Indonesian coal demand for power generation was estimated to increase from 90 million tons to 150-160 million in 2028-2030 [5]. PT. Manggala Alam Lestari (PT. MAL) is one of the companies supplying coal for the power plants located in Musi Banyuasin Regency, South Sumatra, Indonesia. It also supplies coal to PLTU SUMSEL V, which is operated by PT. DSSP Power. The particle size of this mineral is very important for coal power plants, thus it is expected to meet the required specifications during extraction. In the process of coal production and preparation, it is very important to separate it into fractions for various applications by the screen tools [6,7,8,9].

Some of them also stated that the use of appropriate screens or jigs affected the recovery of mining outputs [10, 11, 12]. According to Lestari et al [13], the size of coal grains should not be fine for supply to coal-fired power plants, i.e., limited to < 3 mm. This was due to the effects of dust on the surrounding environment, which leads to the non-actualization of required specifications.

Additionally, PT. MAL is found to set the mineral's standard size at a maximum acceptable size of 20 cm, for supply to the DSSP Power. Besides the particle size, the quality of coal is also very important in power generation, using proximate and ultimate analyses [14]. Based on the proximate analysis, the quality specifications desired by PT. DSSP Power PLTU SUMSEL 5 are as follows, (1) Total Moisture, 45%, (2) Inherent Moisture, 15%, (3) Ash Content, 9% (ADB), (4) Volatile Matter, 41% (ADB), (5) Total Sulfur 0.4% (ADB), (6) Fixed Carbon, 35% (ADB), (7) HGI 74, and (8) Calorific Values, 14.22 and 21.75 MJ/Kg (AR and ADB). Meanwhile, the coal quality specifications according to the ultimate analysis are as follows, (1) Carbon (C), 56%, (2) Hydrogen (H), 4.25%, (3) Nitrogen (N), 0.90%, (4) Sulphur (S), 0.30%, and (5) Oxygen (O), 15.20% (PT. Manggala Alam Lestari's Archive, 2021).

Coal extraction is one of the activities involved in mining operations. At PT. MAL, the utilized extraction processes involve coal sizing, using a fixed screen. The functions of the fixed-screen tool show that the size of the coal to be crushed needs to be consistent with the required specifications for its easy destruction. During field application, two tools are often used, namely collection and loading excavators. In this case, coal is reportedly obtained by the collection excavator and transferred to the loading machine, which loads and crushes the mineral on a fixed screen, with the escaped residues dropping into the vessel dump truck. Using fixed screens, coal excavation activities have many productivity challenges, such as (1) The coal material stuck in between screens, (2) The screen removal when the front coal is exhausted, (3) The coal load fireplaces, etc. This leads to slower cycle

Publisher: **KOMAG Institute of Mining Technology, Poland**

times, compared to the extraction periods without a screen. Therefore, the réévaluations of these activities are needed for better effectiveness and efficiency, regarding the work performances and products obtained from the fixed screen.

The size reduction activity in coal processing often used crushing tools or comminution, whose standard products are supplied to coal-based power plants. Based on these processes, some previous reviews reported the use of the fixed or grizzly screen in andesite stone processing, after the crushing or comminution activity [15]. With most of them analyzing the use of the grizzly screen on andesite stone, for asphalt mixing plant needs [16], others emphasized the utilization of the fixed-screen tool in Croatia's limestone mining [17]. Irrespective of these results, the use of screen tools or sizing without a crusher is still very rarely carried out in the coal industry. Other previous studies also reported that coal processing was carried out for the stockpile port [18], evaluation of the crushing plant production series plan [19], and pit crushing application potential in Saint Petersburg, Russia [20]. Therefore, this study aims to examine the effectiveness of Fixed Screen Tools in PT. Manggala Alam Lestari (MAL), Indonesia, regarding the activities of coal extraction in the technical and economic sectors. The results obtained are expected to provide updates in the development of the mining science field, especially coal processing.

2. Literature review

2.1. Coal resources and reserves

Coal is one of the most abundant sources of energy in the world [21], as a global reserve estimation of approximately 1,074 billion tons was predicted in 2021 [22]. Due to its overall significance, several reviews were conducted on the sustainability of long-term supply. These included the following, (1) Economic Evaluation Regarding the Use of Indonesian Coal [23], (2) Low-Ranked Indonesian Coal Resources with commercially-efficient UBC Technology [24] and (3) Willingness of Indonesian Coal To Meet The 2050 Demand [25].

Besides future production analysis, more reports were also carried out on the peak manufacture of coal. This indicated that the production peak was expected between 2042 and 2062, at a maximum yield of 4.1-4.9 Gtoe/year [26]. Other studies also predicted the rapid increase of coal production by an average of 2.2% p.a from 2010 to 2030 [27]. The number and location of the world's coal beds are shown in Fig. 1.

Indonesia's coal reserves are the second-largest in South and Central Asia, specifically located on the islands of Kalimantan and Sumatra. This energy source is presently the main supply of electric fuel, with an allocation of 55.6% and it is also expected to achieve an electrification ratio of 98% [25]. Based on the Coal and Geothermal Mineral Resources Centre, Ministry of Energy and Mineral Resources [28], Indonesia's energy resources were estimated at approximately 110,069.91 million tons, mostly located in Sumatra and Kalimantan Islands (Fig.2). Measurable resources reached 41,369.38 million tons, where the potentially mined reserves are estimated at 17,903.92 million tons. In addition, the referenced resources are estimated at 34,350.38 million tons and predicted resources achieved 34,350.15 million tons.

Coal resources are mostly classified as lignite (58.7%), sub-bituminous (26.7%), bituminous (14.3%), and anthracite (0.3%). According to the classification of ASTM, the lignite and sub-bituminous grade "C" resources were categorized as Low-Rank Coal [24].

Publisher: **KOMAG Institute of Mining Technology, Poland**

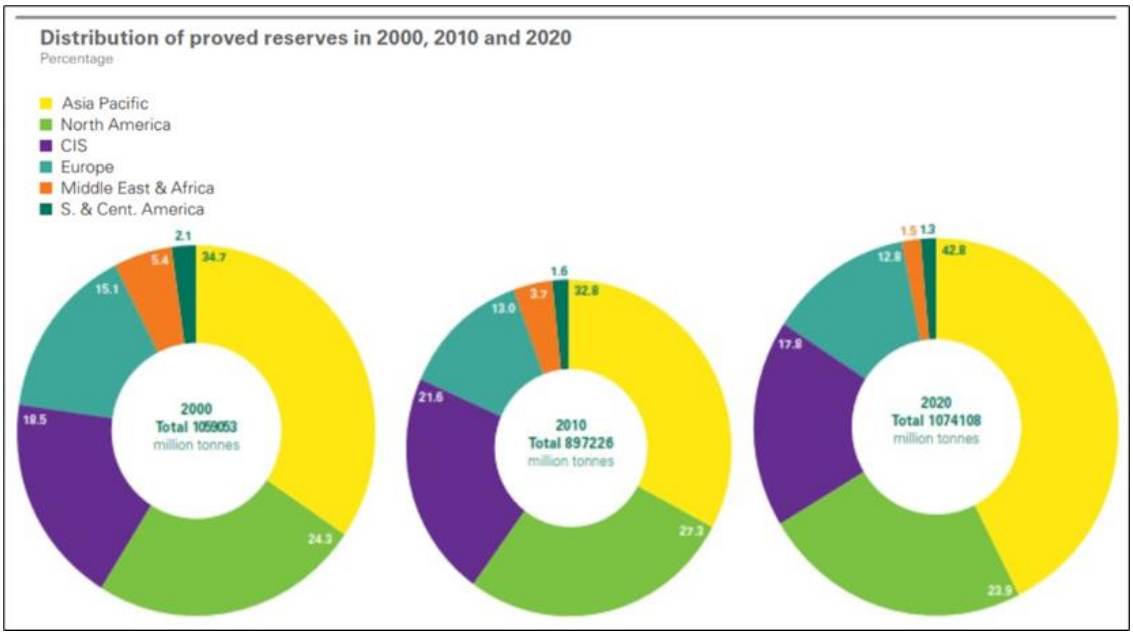

Fig. 1. World Coal Reserves

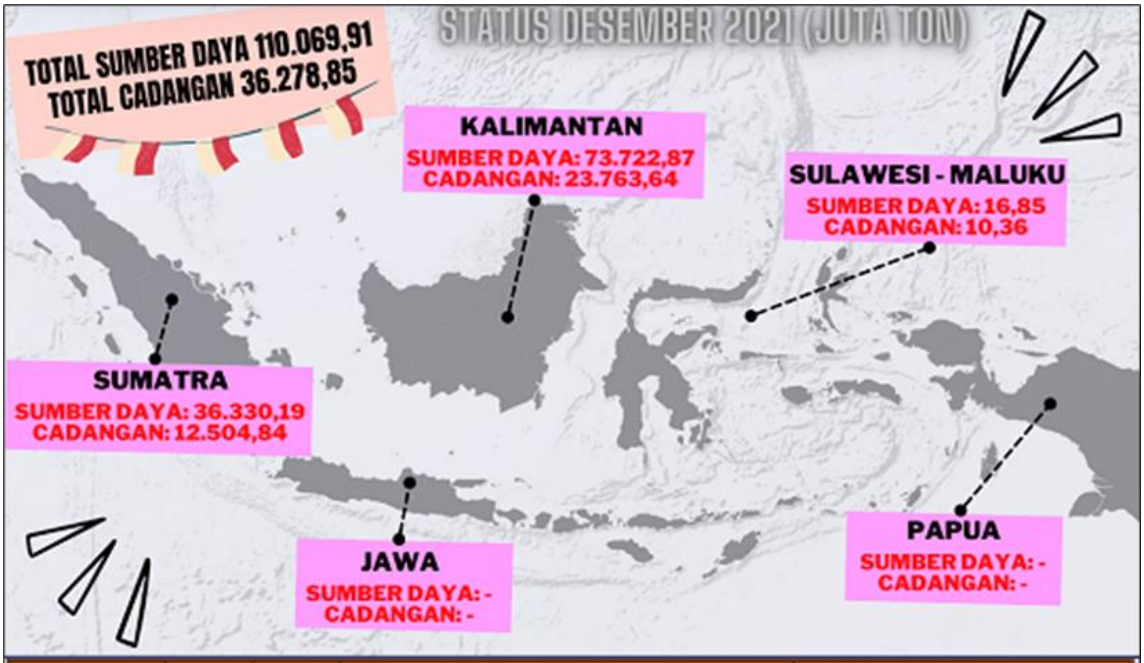

Kualitas	Target Eksplorasi	Total Inventori	Sumberdaya (Juta Ton)					Cadangan (Juta Ton)			
			Tereka	Tertunjuk	Terukur	Total	Total Terverifikasi	Terkira	Terbukti	Total	Total Terverifikasi
Kalori Rendah	417.17	11,252.41	14,961.91	11,979.49	10,402.32	37,343.72	29,703.20	7,523.85	5,401.22	12,925.07	10,869.81
Kalori Sedang	2.06	547.38	14,625.47	18,356.99	26,869.92	59,852.38	51,868.94	9,464.74	11,220.50	20,685.24	18,811.62
Kalori Tinggi	5,040.47	10,717.99	3,368.46	3,135.27	3,228.12	9,731.85	7,246.56	1,139.99	885.96	2,025.95	1,456.17
Kalori Sangat Tinggi	681.42	1,848.07	1,394.31	878.63	869.02	3,141.96	2,787.34	246.34	396.25	642.59	558.02
JUMLAH	6,141.12	24,365.84	34,350.15	34,350.38	41,369.38	110,069.91	91,606.04	18,374.92	17,903.92	36,278.85	31,695.63

Fig. 2. Distribution of Indonesian Coal Resources

The characteristics of coal resources are also shown in Fig. 3, where 8% of the components had high calorific profiles, with the rest mostly categorized as low and medium contents (low-rank coal). With the abundance of these low-ranked resources, the utilization of coal is promoted as fuel for steam power plants in Indonesia.

Publisher: **KOMAG Institute of Mining Technology, Poland**

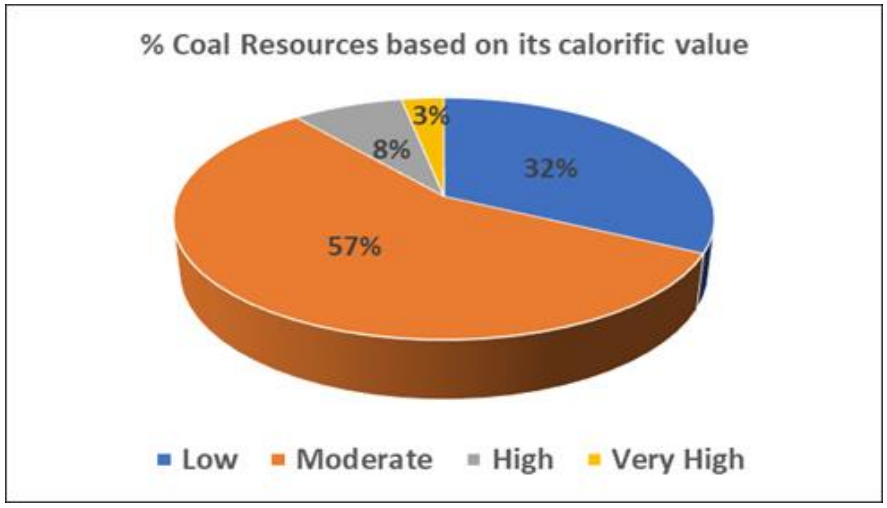

Fig. 3. Indonesian Coal Resources by calorific value

2.2. Coal mining

According to Law No. 3 of 2020 concerning the Amendments of Law No 4 of 2009, mining was partially or totally among the stages of the framework activity, management, and operation of coal. This included the general investigation, exploration, feasibility studies, construction, mining, processing/refining or development/utilization, transportation and sale, as well as post-mining activities [29].

2.3. Coal processing

2.3.1. Comminution

Comminution is the process of reducing specific average particle size to a smaller size, for the separation of impure particles from the existing method.

2.3.2. Sizing

Sizing or grain size uniformization is the process of levelling a sieve dimension according to the desired standards, for the derivation of homogeneous outputs. Based on Ogunmodimu et al [30], the following factors need to be considered in the selection of screen:

a. Methods of feed
   This is to obtain maximum capacity and achieve efficiency, i.e., the material rate should evenly flow over the entire screen surface at a low speed.
b. Angle of slope
   The addition of a suitable slope angle increases the material rate for greater efficiency and capacity, as well as a perfect separation process.
c. Screening surface
   Capacity and efficiency are higher when the screen surface is serially placed between one another, for the flat output of the material.
d. Direction of rotation
   An efficient rotating screen is higher when a rotation is carried out to disrupt the flow of the material rate and the direction of centrifugation.
e. Vibration amplitude and frequency
   The screen's vibration rates and the surface area affect the efficiency of the material. This indicated that higher vibrations and area led to greater efficiency.
f. Screen capacity

Publisher: **KOMAG Institute of Mining Technology, Poland**

Generally depends on the cross-sectional area or track length, load size, and feed properties, such as the specific gravity, water content, temperature, and the type of utilized mechanical screen.

2.4. Correction factors

In loading and digging productivity, the magnitude of the total correction factors includes operator skills, work efficiency, and machine availability [31].

2.4.1. Work efficiency

This is a comparison between productive and available working periods [32]. In this case, effective working time emphasizes the operator and the tools used to carry out production activities [33]. This shows that the available time is realistically unable to be used entirely for production (less than 100%), due to the challenges observed during the mechanical device's operation.

These operational activities include the state of the tool and the working field (mechanical and operating conditions), as well as its human traits as an operator [34]. In addition, the magnitude of the work efficiency value is strongly influenced by the operational condition of the equipment (Table 1).

Table 1. Work efficiency regarding the operational condition

Operating Conditions	Work Efficiency
Good	0.83
Normal – Medium	0.75
Not Good Enough	0.67
Bad	0.58

2.4.2. Machine availability

This indicates the condition and performa+nce of mechanical devices, considering the time lost during the operational period [35].

a. Mechanical Availability (MA)

Mechanical availability shows the readiness (available) of a tool from the time lost, due to instrumental damages or disruptions [34]. The equation used to calculate this factor is shown as follows:

$$MA = W/(W + R)\ x\ 100 \quad (1)$$

where:

MA – Mechanical willingness, %,
W – Working period, hours,
R – Repair period, hours.

The working period is often initiated when the operator mounts an available operational tool. This period is subsequently observed from the recording on the operator's time card or hour meter tool. It also includes delay time [34], which contains the following issues:

1) Loss of time when available to work,
2) Moving time,
3) Lubrication, gasoline filling, and tool maintenance periods,
4) Loss of time due to weather conditions,
5) Safety meeting time,
6) Others.

b. Physical availability (PA).

Publisher: **KOMAG Institute of Mining Technology, Poland**

Physical availability (Operational availability) shows the operational willingness of a tool, by eliminating the loss of time due to various causes [36]. The equation for calculating this factor is shown as follows:

$$PA = (W + S)/(W + R + S)\ x\ 100\ \% \quad (2)$$

where:
PA – Physical Willingness, %,
W – Working period, hours,
R – Repairs period, hours,
S – Standby period or loss of time when the tool is not operated, although is in good condition, hours.

c. Use of availability (UA)

This is the percentage of time used by a tool during operational performances [36]. It was also calculated by dividing the working periods by the sum of operational and standby hours (Eq. 3).

$$UA = W/(W + S)\ x\ 100\ \% \quad (3)$$

where:
W – Working period, hours,
S – Standby period, hours.

d. Effective utilization (EU)

This is the percentage figure of a tool's overall utilization [36], regarding the comparison of working and available periods (Eq. 4). It is also very similar to the utilization of availability, while only inconsistent with working to total periods. Therefore, the EU is the tool utilization in the time available for production activities [34].

$$EU = W/(W + R + S)\ x\ 100\ \% \quad (4)$$

where:
EU – Effective Use, %,
W – Working period, hours,
R – Repair period, hours,
S – Standby period, hours.

2.4.3. Bucket fill factor

The bucket fill factor is a comparison between the actual volume and the theoretical ability of a material. This shows that softer materials cause higher fill factors while forming a state of disrespect on the bucket. However, a hard material leads to many cavities and inadequate material contents. The value of this factor also emphasizes the natural nature of the evacuated material [37]. Based on material conditions, the bucket-fill factor values are determined, as shown in Table 2.

Table 2. Bucket-Fill Factor

Excavating Condition		Bucket Fill Factor
Easy	Excavating the natural ground of clayey, clay, or soft soil	1.1-1.2
Average	Excavating the natural ground of sandy and dry soil	1.0-1.1
Rather Difficult	Excavating the natural ground of sandy soil with gravel	0.8-0.9
Difficult	Loading blasted rock	0.7-0.8

However, the current bucket fill factor value was searched by dividing the current bucket content and the theoretically heaped material (Eq. 5).

$$BF = \frac{Vessel\ Capacity}{Actual\ charging\ amount\ x\ Theoretical\ Heaped\ material} \quad (5)$$

2.4.4. Swell factor

The swell factor is a transformational process, regarding the addition and subtraction of the material volume from its original form [31]. This is divided into three states, namely Bank, Loose, and Compact Conditions. The value of this factor is also calculated by dividing the bank and loose volumes (Eq. 6).

$$SF = \frac{(Bank\ Volume)}{(Loose\ Volume)} \quad (6)$$

2.5. Productivity of excavator

The equation involved in this analysis is shown as follows,

$$\mathbf{TP} = \frac{KB\ X\ BF\ \ X\ SF\ X\ 3600\ X\ FK}{CT} \quad (7)$$

where:

TP – Estimated production, BCM/hour,
KB – Bucket Capacity, m^3,
BF – Bucket Factor,
SF – Swell Factor,
FK – Correction Factor, i.e., tool x work x operator efficiencies,
CT – Cycle time, seconds.

2.6. Efficiency and calculation of loose screen

The amount of material passing at a specific screen size is often expressed in percent (%), as shown in the following equation.

$$\mathbf{Eff}\ \ Screen = \frac{Product\ Weight}{Feed\ Weight}\ x\ 100\% \quad (8)$$

Using the material balance formula, the losses in a processing circuit were subsequently calculated [38].

$$Qin = Qout + Losses \quad (9)$$

where:

Qin – Incoming Material, tons/hour,
Qout – Material Out, tons/hour,
Losses – Loss Factor, tons/hour.

3. Research methods

This experimental analysis was carried out by developing coal without a comminution process and redesigning the screening tool used in the extraction activities. Quantitative methods were also used to calculate the efficiency of a screen, through the challenges encountered in using a fixed-screen tool. Subsequently, these methods were used in comparing the costs of crushing and screen activities in the coal extraction. Irrespective of these conditions, the survey method was carried out to directly observe extraction processes in PT. Manggala Alam Lestari, Musi Banyuasin, South Sumatra, Indonesia.

3.1. Data collection techniques

Data collection was carried out using two methods : primary and secondary. The primary data was obtained through the following methods:

(1) Direct observations in the coal mining field of PT Manggala Alam Lestari, Indonesia. The parameters obtained included : (a) the weight of coal entering the fixed screen as a feed, (b) the weight of coal escaping the filter, (c) the coal retained in the filter,
(2) Recording the time of digging, loading, and transporting,
(3) Conducting calculations to obtain efficiency, capacity, fixed screen productivity, and economic feasibility data,
(4) Field documentation,
(5) Conducting interviews with selected participants, to obtain data on tool production costs, life, and availability, as well as coal extraction process,
(6) Redesigning the fixed screen model efficient and effective for coal extraction,
(7) Other necessary related data.

Secondary data were also obtained through literature and instasional studies. Through the publication of national and international journals, the previous literature emphasized existing analyses, reviews, and other sources related to experimental problems. Meanwhile, the instasional studies were obtained through PT. Manggala Alam Lestari or other related agencies. In this case, the parameters obtained included :

(1) The map of the study location,
(2) Coal production,
(3) Tool feasibility,
(4) Fixed-screen tool specifications, and (5) Other data.

3.2. Data processing and analysis techniques

Data processing was carried out through the utilization of primary and secondary data, to determine the efficiency of screen work. This was subsequently conducted challenges of fixed screen utilization in coal extraction activities. The cost of crushing and screen activities of this mineral production were also compared. This should be conducted based on the obtained raw data, which need to be subsequently processed in deriving the work efficiency of fixed screen tools. They should also be used in redesigning an efficient and effective fixed screen model for coal extraction. In addition, data analysis was descriptively carried out using existing calculations, regarding the analysis of an efficient and effective screen model.

4. Results and discussion

Coal extraction is one of the activities in mining operations, where in-pit processing involved the sizing of this mineral using a fixed or grizzly screen (Figs. 4 & 5). The functions of the fixed screen tool show that the size of the coal to be crushed was consistent with the required specifications for easy destruction. During field application, two tools are often used, namely collection and loading excavators.

Publisher: **KOMAG Institute of Mining Technology, Poland**

Fig. 4. Coal Extraction with In-pit Processing

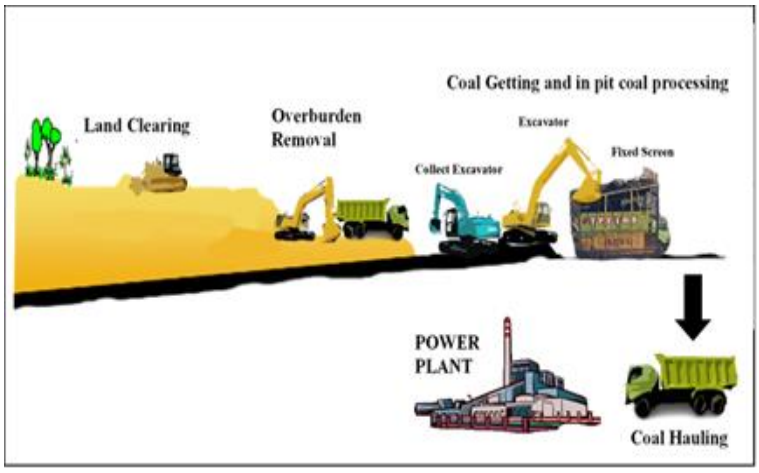

Fig. 5. Mining Process in PT. MAL

4.1. Availability analysis

The important factors, contained MA, PA, UA, and EU representing mechanical availability, physical availability, use of availability, and effective utilization production of the machine were analysed. In PT. MAL, the MA and PA values of the loading excavator were excellent, showing that the average mechanical and physical availability scores were 89 and 92%, respectively in 2021. Based on the MA value, the loading and unloading tools were adequately maintained and rarely damaged. In this case, such loading tools are relatively new or under two years old. For the PA value, non-mechanical resistance such as P2H, diesel lubrication and filling, rain, safety talk, moving unit, and overshift, did not greatly affect the performance of the loading and unloading tool.

However, the UA and EU values of these tools were inadequate in PT. MAL, with the average use of availability and effective utilization values being 67 and 62%, respectively in 2021, respectively. These were due to the encounter of several challenges in the coal extraction activities, including :
(1) The DT queues in the stockpile,
(2) The screen removal when the front coal was exhausted,
(3) The coal material stuck between the screens,
(4) The coal load fireplace,
(5) Awaiting the material feed from the coal collection excavators.
Additionally, the challenges ultimately affected the performance and production of loading and digging tools.

Publisher: **KOMAG Institute of Mining Technology, Poland**

4.2. Excavator productivity

The productivity of the excavator had a difference, which was observed between the screen and in the direct (in the vessel dump truck) coal loading activity. The following Table 3 shows a comparison of productivity and cycle time track length.

Table 3. Comparison of Productivity and Cycle Time

No.	Excavator	Productivity (Tons/h)		Cycle Time (s)	
		Screening	Direct Loading	Screening	Direct Loading
1.	Ex PC210 (TPE-04)	104.87	143.67	26.55	19.02
2.	Ex PC210 (TPE-05)	96.75	134.68	27.06	19.44
3.	Ex PC210 (TPE-11)	97.32	138.89	27.33	19.38
4.	Ex SK200 (TPE-16)	99.39	131.77	27.18	20.50

Based on Table 3, the cycle time of the excavator was slower during screen loading than the direct activity, leading to smaller excavator productivity. Furthermore, the productivity of loading and unloading tools was influenced by the EU and bucket fill factor. This showed that the working efficiency of the PC210 Excavator was insufficient at an average of 62%. Irrespective of this condition, the current bucket fill factor of the digging tool had a value of 1.0, indicating an easy collection of the excavated material. Therefore, cycle time is the main factor affecting the productivity of loading and unloading tools, as the screening process was slower than that of the direct activity due to several challenges. From these obstacles, the resistance of the coal stuck in between the screen and the mineral grinding above the fixed-screen tool was highly effective (Fig. 6). For productivity to be more optimal, engineering performances were importantly needed for the minimization of the material resistance stuck in between these screens. This confirmed that a fixed screen needs improvement and its redesign.

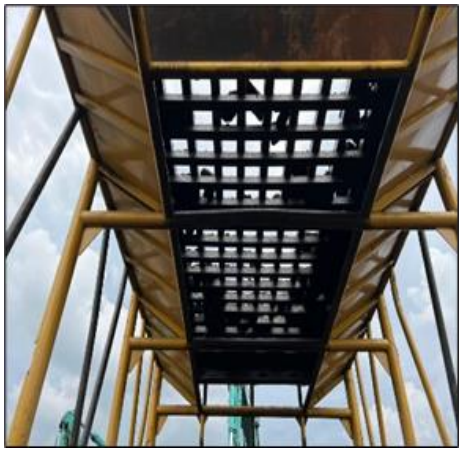

Fig. 6. Coal Stuck in the Sidelines of Fixed Screen

4.3. Fixed screen efficiency

When redesigning the fixed screen in PT. MAL, several parameters used as references were observed, namely the slope angle and the screen capacity, which emphasized the track length.

In this process, the utilized angles included 5°, 15°, 25°, 35°, and 45°, while the lengths were 80, 110, and 140 cm. From these parameters, a fixed screen with a scale of 1:10 was used according to the original size specification in PT. MAL. Experiments were also conducted to obtain the most optimal screen efficiency (Figs. 7 & 8).

Publisher: **KOMAG Institute of Mining Technology, Poland**

Fig. 7. Fixed Screen Scale 1:10

Fig. 8. Fixed Screen Trial Process

The following data (table 4) are the experimental results obtained by using the 1:10 scale fixed screen, 10 kg amount of feed and screen size at approximately 10x10 cm.

Table 4. The fixed screen experiments regarding the scale of 1:10

No.	Parameters		Feed Total Weight (kg)	Feed Weight Pass Screen (kg)	Screen Efficiency (%)	Flow Rate Time (s)
	Length (cm)	The angle of Slope (º)				
1.	80	5	10	7.63	76.3	2.98
		15	10	7.69	76.9	2.78
		25	10	7.86	78.6	2.76
		35	10	8.23	82.3	2.70
		45	10	8.71	87.1	2.82
2.	110	5	10	7.68	76.8	3.01
		15	10	7.79	77.9	2.84
		25	10	8.04	80,4	2.79
		35	10	8.34	83.4	2.84
		45	10	8.91	89.1	2.73
3.	140	5	10	7.77	77.7	3.06
		15	10	7.87	78.7	3.11
		25	10	8.08	80.8	2.81
		35	10	8.42	84.2	2.92
		45	10	9.13	91.3	2.56

Publisher: **KOMAG Institute of Mining Technology, Poland**

Based on Table 4, the most optimal fixed screen had the length, angle, efficiency, and flow time of 140 cm, 45°, 91.3%, and 2.56 s, respectively. However, the screen length needs to be adjusted to that of the dump truck during the field application, to prevent coal material from inappropriately dropping or hitting the roof of the vehicular vessel. From these descriptions, the most optimal fixed screen used in the field had the length, angle, efficiency, and flow time of 80 cm, 45°, 87.1%, and 2.82 s. This results was used to adjust the screen capacity of the dump truck.

5. Conclusions

1. The results obtained were recommended to PT Manggala Alam Lestari and other coal mining industries.
2. The MA and PA values of the coal excavator were approximately 89% and 92%, respectively. This showed that mechanical and non-mechanical resistances such as P2H, lubrication and solar contents, rain, safety talk, moving units, overshifts, etc, did not greatly affect the performance of the loading-digging tools.
3. The UA and EU values of the excavator were also 67% and 62%, respectively, indicating the occurrence of some challenges in coal extraction activities.
4. These coal activity challenges caused a slower cycle time for the excavator, leading to less productivity.
5. To overcome these challenges, the fixed screen should be redesigned by emphasizing the following parameters as references :

   (a) The repose angle,

   (b) The screen capacity.
6. Based on the experimental results, the most optimal fixed screen had the length, angle, efficiency, and flow-rate time of 140 cm, 45°, 91.3%, and 2.56 s, respectively.
7. To adjust toward the length of the dump truck, the most optimal fixed screen used in the field had the length, angle, efficiency, and flow-rate time of 80 cm, 45°, 87.1%, and 2.82 s, respectively.

Acknowledgements

The authors are grateful to the management of PT. Manggala Alam Lestari, for providing the opportunity to conduct a study survey on the mining business permit location.

References

[1] Juniah R., Sastradinata M.: Study benefit value of utilization water resources for energy and sustainable environment. AIP Conference Proceedings 2017. 1903(1)

[2] Lei Y., Li L., Pan D.: Study on the relationships between coal consumption and economic growth of the six biggest coal consumption countries: with the coal price as a third variable. Energy Procedia 2014. 61(2014), pp. 624–634

[3] Komarova A. V., Filimonova I. V., Kartashevich A. A.: Energy consumption of the countries in the context of economic development and energy transition. Energy Reports 2022. 2022(8), pp. 683-690

[4] U.S. Energy Information Administration, International Energy Outlook 2016 with Projections to 2040. Washington DC: U.S. Department of Energy 2016

[5] Arinaldo D., Adiatma J. C.: Dynamics of Indonesian coal: Towards a just energy transition. Jakarta: Institute for Essential Services Reform 2019

[6] Wang Z., Peng L., Zhang C., Qi L., Liu C., Zhao Y. Research on impact characteristics of screening coals on vibrating screen based on discrete-finite element method. Energy Sources, Part A: Recovery, Utilization, And Environmental Effects 2019. 42(16), pp. 1-14

[7] Zhao G., Wang X., Yu C., Liu S., Zhou J., Zhu G.: Research on Static and Dynamic Characteristics of Shear Spring of The Vibrating Flip-Flow Screen. Symmetry Journal 2020. 12(10), pp. 1644

[8] Yu C., Wang X., Pang K., Zhao G., Sun W.: Dynamic characteristics of a vibrating flip-flow screen and analysis for screening 3 mm iron ore. Hindawi Journal: Shock and Vibration 2020. 2020(7), pp. 1-12.

[9] Mohanty M. K.: Fine coal screening performance enhancement using the pansep screen. Int. J. Miner. Process 2002. 69(2003), pp. 205– 220

[10] Haryono A., Rubiono G., Qiram I.: The effect of vibrating screen tilt angle on sieve performance. Journal V-Mac 2020. 5(1), pp. 13-16

[11] Susanto R., Nasrudin D., Sriyanti: Comparative analysis of vibrating screen dimensions in sand mining in PT. Mitra Lintas Persada, Giri Mukti Village, Saguling district, West Bandung regency, West Java province. Proceedings of Mining Engineering 2016. 4(1), pp. 343-351

[12] Selviyana F., Hasjim M., Juniah R.: Kajian teknis pengaruh ketebalan lapisan bed pada pan american jig terhadap recovery timah di Tb 1.42 Pemali PT. Timah (Persero) Tbk, Bangka Belitung. Jurnal Ilmu Teknik Unsri 2015. 3(1), pp. 1-7

[13] Lestari S. D., Asy'ari M. A., Hidayatullah R.: Coal geochemistry for some industries. Journal of Engineering Axis 2016. 8(1), pp. 48-54

[14] Budiman A. A., Anshariah: Determination of coal quality in enrekang regency based on proximate and ultimat analysis. Journal of Geomine 2017. 5(2), pp. 53–58

[15] Cahya R. N., Hasjim M., Ningsih Y. B.: Performance study of andesite stone crushing plant unit PT. Sumber Gunung Maju. Unsri Mining Journal 2020. 4(1), pp. 27-36

[16] Juniardi F., Adiansyah J. S.: Production target of andesite stone aggregate crushing plant results for asphalt mixing plant needs (PT. Intention of the Work). Ulul Albab Journal 2020. 24(1), pp. 60-64

[17] Klanfar M., Vrkljan D.: Benefits of using mobile crushing and screening plants in quarrying crushed stone. AGH Journal of Mining and Geoengineering 2012. 36(3), pp. 167-175

[18] Panjaitan D.D.I., Virgiyanti L., Wiryanto Y. H.: Cost coal processing at stockpile port muara bengalun PT. Mitrabara Adiperdana, Tbk Malinau Village, Malinau City, Malinau District, Malinau Regency, North Kalimantan Province. Journal of Teknika 2018. 2(1), pp. 68-76

[19] Endarto R., Juniah W., Herlina: Evaluation of concatenation planning of crushing plant production system using analytic hierarchy process (AHP) method at PT. Buana Eltra Coal Processing Unit, South Sumatra. Indonesian Journal Of Environmental Management And Sustainability 2018. 2(1), pp. 1-6

[20] Mikhailov A.V., Garmaev O.Z., Garifullin D.R., Kazakov Y.: A potential application of in-pit crushing-conveying and dewatering system in Peat Mining Saint Petersburg, Russia. IOP Conference Series: Earth And Environmental Science 2019. 378(2019), pp. 1-5

[21] Zhengfu B., Hilary I. I., John L. D., Frank O., Sue S.: Environmental issues from coal mining and their solutions. Mining Science and Technology 2010. 20(2), pp. 215-223

[22] Statistical Review of World Energy 70th Edition, London: BP p.l.c 2021

[23] Soelistijo U. W., Suganal: The economic evaluation of research based Indonesian coal utilization. Indonesian Mining Journal 2013. 16(1), pp. 1-17

[24] Daulay B., Santoso B., Sodikin I.: Indonesian low rank coal resources to wich ubc technology is commercially applicable. Indonesian Mining Journal 2007. 10(08), pp. 18–23

[25] Hudaya G.K., Madiutomo N.: The availability of Indonesian coal to meet the 2050 demand. Indonesian Mining Journal 2019. 22(2), pp. 107–128

[26] Maggio G., Cacciola G.: When will oil, natural gas, and coal peak? Fuel 2012. 98, pp. 111-123

[27] Bauer N., Mouratiadou I., Luderer G., Baumstark L., Brecha R.J., Edenhofer O., Kriegler E.: Global fossil energy markets and climate change mitigation-an analysis with remind. Climatic Change 2016. 136(1), pp. 69-82

[28] Coal and Geothermal Mineral Resources Centre. Ministry of Energy and Mineral Resources of Indonesia 2021

Publisher: **KOMAG Institute of Mining Technology, Poland**

[29] Rahmi S. D., Juniah, R.: Utilization study of void mine for sustainable environment of the limestone mining sector at PT Semen Baturaja (Persero) Tbk. Indonesian Journal of Environmental Management and Sustainability 2019. 3(2019), pp. 54-59

[30] Ogunmodimu O., Govender I., Mainza N.A., Franzidis P.J.: Development of a mechanistic model of granural flow on vibrating screen. Minerals Engineering 2021. 163(5)

[31] Tenriajeng A. T.: Mechanical Soil Removal. Jakarta: Gunadarma Publishers 2003

[32] Kadir, E.: Mechanical Soil Removal. Palembang: Sriwijaya University 2008

[33] Pramana G. D., Sudiyanto A., Setyowati I., Titisariwati I.: Technical study of the production of digging-loading equipment and conveyances to meet the production target of coal mining overburden stripping pt. Image of Tobindo Sukses Perkasa, Sarolangun regency, Jambi province. Journal of Mining Technology 2015. 1(2), pp. 61-68

[34] Indonesianto, Y.: Mechanical soil removal. Universitas Pembangunan Nasional "Veteran" Yogyakarta 2005

[35] Zega R. A.: Analysis of the achievement of mining planning based on reconciliation of mining blocks to achieve limestone production target of 1,800,000 tons per year in Kuari Pusar in PT. Semen Baturaja (Persero), Tbk. Thesis, Faculty of Engineering: Sriwijaya University 2016

[36] Partanto P.: Mechanical Soil Removal. Bandung: Bandung Institute of Technology 1996

[37] Komatsu Ltd: Specification and Application Handbook, 30th Edition. Komatsu 2009

[38] Munandar F. A., Sriyanti: Yuliadi, Performance evaluation of the andesite stone crushing plant unit at PT silva andia utama in Giri Asih village, Batujajar district, Bandung regency, West Java province. Journal of Proceedings of Mining Engineering UNISBA 2018. 4(2), pp. 486-494

Publisher: **KOMAG Institute of Mining Technology, Poland**

https://doi.org/10.32056/KOMAG2022.4.3

Constructional changes of pneumopercussion machines for improving their efficiency

Received: 19.09.2022

Accepted: 29.12.2022

Published online: 30.12.2022

Author's affiliations and addresses:

[1] Institute of Geotechnical Mechanics of National Academy of Sciences of Ukraine, 2a Simferopilska str., 49000, Dnipro, Ukraine

[2] Dnipro University of Technology, 19 Yavornytskoho Ave., 49005, Dnipro, Ukraine

[3] Energy Economy Research Institute of the Polish Academy of Sciences, J. Wybickiego 7A, 31-261, Kraków, Poland

*** Correspondence:**

e-mail: arturdyczko@gmail.com

Volodymyr ANTONCHIK [1], Kostiantyn ZABOLOTNYI [2], Valentyn HANKEVICH [2], Vira MALTSEVA [1], Oleksandra KUTS [1], Artur DYCZKO [3*]

Abstract:

Pneumopercussion machines (pneumatic impact machines) are widely used in all areas of human activity. Also, they are widely used in the mining industry. Unfortunately, their operation is characterized by a low efficiency of compressed air energy usage. In some cases, this level of efficiency is calculated as 15-20%. Such a situation increases the cost of drilling operations significantly. In this article, due to an implementation of a new construction of the equipment, the efficiency of the pneumopercussion machines was increased. This problem is solved by combining the most effective thermodynamic processes of compressed air in the working chambers of machines. Also, a new technical solution for the construction of pneumopercussion machines is suggested by the Authors. The proposed new design is realized by a combination of the most effective thermodynamic processes in the chambers of pneumatic impact machines. A new pneumatic hammer is presented, which allows to reduce compressed air consumption twice during an operation on the surface (in comparison with hammers available on the market). The operation of pneumopercussion machines and the method of calculating geometric parameters are described. The economic performance of the equipment confirms the correctness of the proposed technological solutions.

Keywords: pneumopercussion machines, thermodynamic processes, hammer, compressed air

1. Introduction

One of the most important indicators of the efficiency and operational cost of pneumatic hammers is a consumption of compressed air, the cost of which is up to 50% of the cost of a running metre of a well drilled with a pneumatic hammer. Their usage is caused by the need to introduce small mechanization in production. They are also quite often used in the mining industry [1]. Economical, technical and technological application of this equipment is indispensable in the complex use of mining equipment. Energy reserve as regards the parameters of parallel power active compensators is also very important for increasing the efficiency of the equipment operation in mining [2].

Available pneumopercussion machines, having a small, about 15-20%, efficiency, require a significant consumption of compressed air which increases the cost of drilling. One of the most promising ways to increase efficiency of pneumopercussion machines includes an improvement of their thermodynamic parameters. This can be done by increasing the useful work of thermodynamic processes and combining such processes into cycles [3]. The correct economic evaluation of the proposed technical and technological solutions, which are adopted in mining, is also important [4].

In available hammer designs compressed air is used twice for a full cycle of movement of the striker (hammer) - to accelerate the striker (hammer) at the stage of the working stroke, followed by the exhaust of compressed air into the atmosphere and to return the striker (hammer) to its original position, during the reverse stroke, with subsequent exhaust of compressed air into the atmosphere [5]. Thus, the full cycle of movement of the striker (hammer) of available pneumatic hammers consists of cycles of compressed air operation at the stage of isobaric and adiabatic expansion and acceleration of the striker (working stroke), followed by the exhaust of portions of compressed air into the atmosphere and cycles of isobaric and adiabatic expansion and acceleration of the striker in the opposite direction (reverse stroke) with the subsequent exhaust of portions of compressed air into the atmosphere [6]. Thermal processes, occurring during the operation of the equipment, can be presented using the Neumann principle [7]. This principle was also used for a determination of maximum stresses [8]. The required frequency of strikes of the striker, determined by the drilling process, does not enable a full expansion of compressed air to the atmospheric pressure in the known designs of pneumatic hammers due to a short period of acceleration of the striker. In this regard, a significant part of the compressed air, both during the working and reverse strokes of the striker, is emitted into the atmosphere after the striker reaches the required speed [9].

2. Methods

The essence of the method for increasing the thermodynamic efficiency of pneumopercussion machines is described below. The highest thermodynamic efficiency of pneumopercussion machines is achieved due to thermodynamic processes in their working chambers by combining them into one cycle. Full acceleration of the striker (at the stage of the working stroke) is carried out only by an isobaric expansion of compressed air from the high-pressure line without exhausting any part of it into the atmosphere [10]. After the striker strikes the drilling bit, pressurized air should be supplied to the reverse stroke chamber and the striker should be accelerated to the required speed by an isobaric expansion in the opposite direction. After that, it is necessary to shut off the supply of compressed air to the reverse stroke chamber and continue moving the striker in the opposite direction by an adiabatic expansion of the compressed air remaining in the reverse stroke chamber. When the speed of the striker is sufficient to return it to its original position, the striker, moving by inertia, opens the exhaust holes and a portion of compressed air from the return chamber is released into the atmosphere [11]. Thus, the full cycle of operation of the pneumatic hammer can be carried out with two isobaric and one adiabatic expansion of compressed air, followed by one exhaust of its portion into the atmosphere.

The pneumatic hammer design that implements the specified cycle of thermodynamic processes must have the following design features:

– the compartment for the translational movement of the accelerator in the high-pressure chamber, where an isobaric expansion of compressed air occurs at the stage of the striker's working stroke;

Publisher: **KOMAG Institute of Mining Technology, Poland**

- the compartment for the translational movement of the striker in the reverse stroke chamber, in which first isobaric, and then - adiabatic expansion of the portion of compressed air occur at the striker's reverse stroke stage;
- the striker movement section should be divided by the striker into two isolated chambers;
- the striker reverse stroke chamber and low-pressure chamber, which is permanently connected to the atmosphere by a through-passage channel;
- the accelerator must rigidly join with the striker during the working stroke of the striker to accelerate the striker together with the accelerator to the required speed, as well as at the stage of the striker's reverse stroke to decelerate it after the striker reaches the required reverse stroke speed and until the striker with the accelerator stop completely.

3. Results

3.1. The pneumatic hammer design that implements a new way of operation

The design of the DTH hammer (down-the-hole hammer) for an implementation of the specified method of operation is shown in Fig. 1.

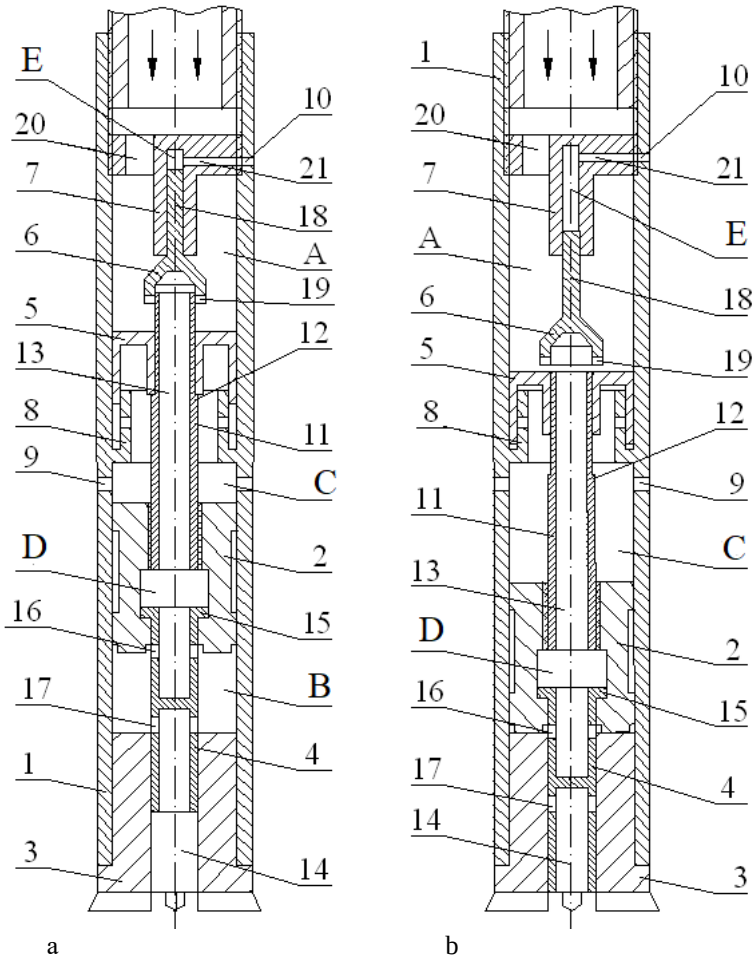

Fig. 1. DTH pneumatic hammer: a – original position, b – striker at the impact moment

The DTH hammer consists of body 1, striker 2, drill bit 3, bushing 4, accelerator 5, valve 6, valve stop 7, accelerator stop 8. Body 1 has discharge holes 9, 10. Striker 2 has a shank 11 rigidly connected to it with an annular shoulder 12 and the axial bore of the shank 13. The drill bit 3 has an axial bore of the bit 14. The bushing 4 has an annular ledge 15, inlet holes 16 and outlet holes 17. The valve 6 has a stem 18 and a cylindrical ledge with radial slots 19. The valve stop 7 has feed holes 20 and discharge channel 21.

Publisher: **KOMAG Institute of Mining Technology, Poland**

The hammer has a high-pressure chamber A, a reverse stroke chamber B, and a low-pressure chamber C. Striker 2 has a cavity D. Valve stop 7 has a cavity E.

3.2. The DTH hammer operation

The hammer works in the following manner. In the original position, the shank of the striker 11 with an annular ledge 12 butts with the accelerator 5 and the valve 6, which closes the axial bore of the shank 13 and the supply of compressed air to the reverse stroke chamber B (Fig. 1a). Bushing 4 is in the uppermost position. After supplying compressed air to the hammer through the supply holes 20 at the stop of the valve 7, due to the difference in air pressure between the high-pressure chamber A and chambers B and C (where the pressure is atmospheric, since they are connected to the atmosphere by the outlet holes 17, the axial bore of the bit 14 and hole 9), the compressed air in chamber A expands and accelerates the accelerator 5 (which abuts against the annular ledge 12 of the shank 11) together with the striker 2, the shank 11 and the valve 6 in the direction of chambers B and C, making a working stroke. Air from chamber B through the outlet holes 17 of the bushing 4 and the axial bore of the bit 14 is exhausted into the atmosphere. During the acceleration of the striker 2, the bushing 4 remains in the extreme upper position when the outlet holes 17 remain open and connected to the atmosphere (Fig. 1a). The distance between the accelerator 5 and the stop of the accelerator 8 is calculated so that the accelerator 5 stops at the stop of the accelerator 8 at the moment when the striker 2 has received the required speed and impact energy (Fig. 1b). Further, the striker 2 together with the valve 6 move until the valve 6 collides with the accelerator 5. After that, the valve 6 stops, and the striker 2, having passed another 3 mm, collides with the drill bit 3 (Fig. 1b). At the moment of separation of the valve 6 from the shank 11, the striker 2 with the end wall of the cavity D pushes the bushing 4, which, having received an impulse, moves in the outlet channel 14 of the drill bit 3, blocking the outlet holes 17 and subsequently the air outlet from the reverse chamber B. After separating the valve 6 from the shank 11, compressed air from the high pressure chamber A through the cylindrical ledge with radial slots 19 and the axial bore 13, the shank 11 enters the cavity of the striker D and presses the annular ledge 15 of the bushing 4 to the wall of the cavity D of the striker 2, opening the inlet holes 16 of the bushing 4, and leaves it in this ledge at the moment the striker 2 hits the drill bit 3. At the moment of impact of the striker 2 on the drill bit 3, compressed air from the high-pressure chamber A through the axial bore of the shank 13, the cavity of the striker D and the inlet holes 16 of the bushing 4 enters the reverse stroke chamber B, where the air pressure increases to a high pressure equal to the pressure in the line compressed air supply [9].

Due to the difference in air pressures in chambers B and C (where the air pressure is atmospheric), an unbalanced force appears from the side of the reverse chamber B, which accelerates the striker 2 in the opposite direction. Valve 6 after collision with accelerator 5 and separation from the shank 11 due to the difference in air pressures in the high-pressure chamber A and the cavity E in the stop of the valve 7 (where the air pressure is atmospheric, since the cavity E is constantly connected to the atmosphere by the discharge channel 21 and the discharge hole 10), starts to move in the opposite direction, compressing the air in cavity E. The distance between the annular ledge 12 of the shank 11 of the striker 2 and the accelerator 5 is calculated so that they join at the moment when the striker 2 receives speed and kinetic energy sufficient to complete the reverse stroke. Further, the striker 2 with the accelerator 5 (which move faster than the valve 6) catch up with the valve 6 and the shank 11 joins the valve 6, blocking the flow of compressed air into the reverse chamber B. Further movement of striker 2 with shank 11, accelerator 5 and valve 6 occurs by inertia and under the action of adiabatic expansion of a portion of compressed air in chamber B. On the other side, in the high-pressure chamber A, the accelerator 5 and valve 6 are acted upon by the high-pressure force of compressed air, which breaks the accelerator 5 together with the striker 2, the shank 11 and the valve 6 (Fig. 1 a).

At the stage of the reverse stroke, the striker 2 pulls the bushing 4 by the annular ledge 15 and at the end of the reverse stroke, the bushing 4, leaving the axial bore of the bit 14, opens the outlet holes 17 through which the compressed air from chamber B is exhausted into the atmosphere. The kinetic energy of striker 2, shank 11 with accelerator 5 and valve 6, together with the total action of compressed air pressure forces on them in chambers A and B, are calculated so that at the end of the reverse stroke, striker 2 with shank 11, accelerator 5 and valve 6 return to the original position considering the exhaust

Publisher: **KOMAG Institute of Mining Technology, Poland**

of compressed air from chamber B into the atmosphere. After that, the cycle of the working and reverse stroke is repeated.

3.3. Calculation of the geometric parameters of the pneumatic hammer

The calculation of the geometric dimensions of the hammer is made by successive solving of the equations of motion of the striker 2 and the accelerator 5 and the valve 6 at different stages of the thermodynamic cycles of the compressed air expansion. Since the time of the working cycle of the striker (working and reverse stroke of the striker) is approximately 0.03-0.05 s, the energy losses of the compressed air due to the transfer of heat to the environment can be neglected due to their small value, therefore the process of expansion of the portion of compressed air in the reverse stroke chamber B of the hammer can be considered adiabatic [12]. Small volumes of the hammer chambers in comparison with the volume of the compressed air supply line, as well as the speed of propagation of compressed air (in the order of the speed of sound) in the hammer cavity allows the process of striker acceleration with the expansion of compressed air permanently supplied from the line to be considered isobaric [13].

The diameter of the hammer and the dimensions of the cross-sections of its parts, bores, cavities and chambers are set constructively, based on the diameter of the drilled hole. The linear dimensions of the accelerator 5 are also set constructively. The linear dimensions of the body 1, striker 2, bit 3 and bushing 4 and valve 6 are specified after determining the working and reverse stroke of striker 2, accelerator 5 and valve 6.

An acceleration of striker 2 with accelerator 5 and valve 6 to a given speed and impact energy from the initial position at the stage of isobaric expansion of compressed air is determined as follows:

$$K_{\mathrm{c}} = \int_0^V p_m\,(V)dV \tag{1}$$

$$K_c = K_y + K_b + K_k \tag{2}$$

where:

K_{c} - the total kinetic energy of striker 2, accelerator 5 and valve 6 at the end of striker acceleration, J;

K_k - kinetic energy of the valve at the end of the acceleration of the striker, J;

K_y - kinetic energy of the accelerator at the end of the acceleration of the striker, J;

K_b - kinetic energy of the striker 2 required to hit the drill bit and destroy the rocks, J. This value is set depending on the hardness of the rocks. Knowing the mass of the striker from the formula: $K_b = \frac{m_b \vartheta_b{}^2}{2}$;

where: m_b - weight of the striker, kg; ϑ_b - the speed of the striker at the moment of its impact on the drill bit.

The kinetic energies of the accelerator 5 and the valve 6 are determined by the speed of the striker with which they have the same speed. The masses of the accelerator 5 and the valve 6 are determined constructively based on the dimensions and materials of these parts.

Considering that in the isobaric process $p_m = const$, as well as for the cylindrical shape of the impactor chambers $V = S \cdot X$, we obtain:

$$K_{\mathrm{c}} = p_m \int_0^{V_1} dV = p_m(V - 0) = p_m \cdot S_y \cdot X_P \tag{3}$$

$$X_{\mathrm{p}} = \frac{K_{\mathrm{c}}}{p_m \cdot S_y} \tag{4}$$

where:

p_m - pressure of supplied compressed air, Pa;

V - volume of compressed air in the thermodynamic cycle of its expansion, m^3;

S_y - the cross-sectional area of the accelerator, m^2;

X_P - the path traveled by the striker together with the accelerator and valve, m.

A determination of the return stroke of the striker in an isobaric expansion of compressed air in chamber B of the return stroke is determined by the formula:

$$K_0 = \int_0^{V_1} p_m\,(V)dV \tag{5}$$

$$K_0 = p_m \int_0^{V} dV = p_m(V - 0) = p_m \cdot S_b \cdot X_1 \tag{6}$$

where:

K_0 - the kinetic energy of the striker at the end of the section of isobaric expansion of compressed air, J;

S_b - the area of the butt end of the striker in the return chamber B, m^2;

X_1 - the return path of the striker in isobaric expansion of compressed air in the return chamber B, m.

A determination of the reverse stroke of the striker with accelerator 5 and valve 6 in adiabatic expansion of compressed air in the reverse stroke chamber B.

From the moment valve 6 docks with the striker shank, the compressed air supply to the return chamber B stops and the striker 2 with accelerator 5 and valve 6 moves under the action of the following forces: from the side of chamber B - the force of adiabatic expansion of compressed air in chamber B and the inertia force that the striker 2 with accelerator 5 acquired at the stage of their acceleration due to the isobaric expansion of compressed air in chamber B, and on the other hand, the pressure force of compressed air in the line and energy incoming air flow from the high pressure line, which was formed as a result of the consumption of compressed air to fill the return chamber B.

The movement of the striker with the accelerator at this stage is described by the following equation:

$$A_a + K_o = A_m + K_g \tag{7}$$

where:

A_a - work of the adiabatic expansion of compressed air in chamber B of the reverse stroke.

K_o - kinetic energy of the striker and accelerator by the beginning of the adiabatic expansion cycle.

A_m - the work of pressure forces of compressed air in the line.

A_g - kinetic energy of the dynamic pressure of compressed air on the striker 2 and the accelerator 5.

Equation (1) can be rewritten as:

$$\int_{V_1}^{V_2} P_a\,(V)dV + \int_0^{V_1} P_m\,dV = \int_{V_1}^{V_2} P_m\,dV + \frac{\dot{m}\vartheta^2}{2}t_2 \tag{8}$$

where:

V_1 - volume of compressed air in chamber B at the beginning of the adiabatic expansion, m^3;

V_2 - volume of compressed air in chamber B by the end of the adiabatic expansion, m^3;

P_a - current value, pressure in chamber B during adiabatic expansion, Pa;

$\dot{m}$ - mass flow rate per second of compressed air, kg/s;

ϑ- compressed air flow rate, m/s;

t_2 - the time of the return stroke of the striker with the accelerator 5 and the valve 6 at the stage of the adiabatic expansion of the compressed air in the chamber B.

After integrating the terms of equation (8), we obtain:

$$\frac{P_1V_1}{k-1}\left[\frac{(V_2)^{k-1}-(V_1)^{k-1}}{(V_2)^{k-1}}\right] + P_mV_1 = P_m(V_2 - V_1) + \frac{\dot{m}\vartheta^2}{2}t_2 \tag{9}$$

where: k - adiabatic exponent (dimensionless quantity).

For the adiabatic expansion of a gas (air), an equality is true, which is the Poisson equation.

$$P_1(V_1)^k = P_2(V_2)^k = P_3(V_3)^k = \cdots = const \tag{10}$$

Based on this:

$$\frac{P_1}{P_2} = \left(\frac{V_1}{V_2}\right)^k \tag{11}$$

In the known designs of the pneumatic hammer, the stealing pressure decreases before the exhaust by 2.5-2.7 times, which, in accordance with (10), corresponds to an increase in the initial volume of compressed air by about 2 times, i.e.

$$V_2 = 2V_1 \tag{12}$$

Substituting in (8) instead V_2 of its value from (11) we get:

$$\frac{P_1V_1}{k-1}[(V_2)^{k-1} - (V_1)^{k-1}] + P_mV_1(V_2)^{k-1} = P_m(2V_1 - V_1)(2V_1)^{k-1} + \frac{\dot{m}\vartheta^2}{2}t_2 \tag{13}$$

$$\frac{P_1{V_1}^k}{k-1}[(2)^{k-1} - 1] + P_m2^{(k-1)}{V_1}^k = P_m2^{k-1}{V_1}^k + \frac{\dot{m}\vartheta^2}{2}t_2 \tag{14}$$

As you know, from gas dynamics, the one-time second flow rate of gas (air) is equal to:

$$\dot{m} = \rho\vartheta S \tag{15}$$

where:

ρ - density of the gas (compressed air), kg/m^3;

ϑ - gas flow rate, m/s;

S - cross-sectional area of the gas flow, m^2.

The air flow rate is equal to the speed of the air coming from the line into the chamber B (return stroke of the striker) and is equal to the speed of the striker at the end of the section X_1 of the isobaric expansion of compressed air.

According to the well-known formulas of mechanics at $\vartheta_0 = 0$,

$$\vartheta = at_2 \tag{16}$$

where:

a - acceleration of the object, m/s^2; ($a = F/m_b$, where: F- force acting on the striker, N; m_b- weight of the striker, kg);

t - time of movement of the object with a given acceleration, s;

ϑ_0 - initial speed, m/s.

In section X_1 of the isobaric expansion of compressed air:

$$F = p_mS_b \tag{17}$$

where is the line pressure p_m

$$\vartheta = \frac{p_mS_b}{m_b}t_2 \tag{18}$$

where S_b - area of the butt (cross-section) of the striker, m^2.

Substituting (16) and (17) into (15) and further into (14) we get:

$$\dot{m} = \rho\frac{p_mS_b}{m_b}t_2S \tag{19}$$

In our case, the cross-sectional area of the gas flow is equal to the area of the end face of the cross-section of the striker, taking this into account, we obtain:

$$\dot{m} = \rho\frac{p_mS_b}{m_b}t_2 \tag{20}$$

As you know, the cycle of operation of the hammer striker consists of the time of forward and reverse stroke of the striker. The working stroke time of the striker is equal to the time of its acceleration and is determined as follows:

$$t_c = t_\text{p} + t_{obp} \tag{21}$$

where the time t_c of one cycle of movement of the striker is set from the drilling conditions. Since the striker with the accelerator and the valve moved from a state of rest, then:

$$\vartheta_{kr} = a_pt_p, \text{ from this } t_p = \frac{\vartheta_{kr}}{a_p} \tag{22}$$

where:
t_p - acceleration time of the bike with the accelerator 5 and the valve 6 to the set speed, s;
a_p - acceleration of the accelerator bike and the valve at the stage of the working stroke m/s^2;
ϑ_{kr} - the final specified speed of the accelerator striker and valve at the stage of the working stroke, m/s;

$$\vartheta_{kr} = \sqrt{\frac{2K_b}{m_b+m_y+m_{kl}}} \tag{23}$$

At $F = p_m S_y$, where: F - pressure force of compressed air on the accelerator, N; S_y - end area of the end section of the accelerator, m^2. We get from here $a_p = \frac{F}{m_b+m_y+m_{kl}} = \frac{p_m S_y}{m_b+m_y+m_{kl}}$, where m_y - mass of the accelerator, kg; m_{kl} - valve weight, kg.

Substituting (23) into (22) we get:

$$t_p = \frac{\sqrt{\frac{2K_b}{m_b+m_y+m_{kl}}}(m_b+m_y+m_{kl})}{p_m S_y} \tag{24}$$

The striker return time consists of the acceleration time with isobaric expansion of compressed air - t_1 and the movement time of the striker with adiabatic expansion of compressed air - t_2.

Based on the known formulas of mechanics:

$$X_1 = \frac{a_{obp1} {t_1}^2}{2} \tag{25}$$

from here

$$t_1 = \sqrt{\frac{2x_1}{a_{obp}}} \tag{26}$$

for $a_{obp} = \frac{F}{m_b}$ and $F = p_m S_b$, we get:

$$a_{obp} = \frac{p_m S_b}{m_b} \tag{27}$$

where:
X_1 - striker path at the stage of isobaric expansion of compressed air, m;
a_{obp1} - striker acceleration at the stage of isobaric expansion of compressed air, m/s^2.
t_1- time of movement of striker on the segment, s;
F- force of action on the striker, N.

Substituting (27) into (26) we get:

$$t_1 = \sqrt{\frac{2X_1 m_b}{p_m S_b}} \tag{28}$$

Striker return time:

$$t_{obp} = t_1 + t_2 \tag{29}$$

Consists of t_1- time of movement in the section, X_1- path in the section of the adiabatic expansion of compressed air.

From (21) we obtain t_{obp} and from (29) t_2 we obtain:

$$t_2 = t_{obp} - t_1;\ t_2 = t_c - t_p - t_1 \tag{30}$$

Substituting into (13) the values m, ϑ and t_2 from formulas (17), (20) and (30) we obtain:

$$\frac{P_1 {V_1}^k}{k-1}[2^{k-1}-1] + P_m 2^{(k-1)} {V_1}^k = P_m 2^{k-1} {V_1}^k + \rho \frac{\dot{p_m} {S_b}^2}{m_b} t_2 \left(\frac{\dot{p_m} {S_b}^2}{m_b}\right)^2 t_2 \cdot 0{,}5 \tag{31}$$

Given that $V_1 = S_b X_1$ and substituting into (31) instead V_1 of its value $S_b X_1$ we obtain (32).

$$\frac{P_1 (S_b X_1)^k}{k-1}[2^{k-1}-1] + P_m 2^{(k-1)} (S_b X_1)^k = P_m 2^{k-1} (S_b X_1)^k + \\ +0{,}5\rho \left(\frac{\dot{p_m} {S_b}^2}{m_b}\right)^3 \left(t_c - \frac{\sqrt{\frac{2K_b}{m_b+m_y+m_{kl}}}(m_b+m_y+m_{kl})}{p_m S_y} - \sqrt{\frac{2x_1 m_b}{p_m S_b}}\right) \tag{32}$$

There X_1 is only one unknown in this equation.

This equation does not have an analytical solution and is solved by numerical methods. Having obtained X_1 the value from relation (11), we obtain $X_2$and the entire length of the reverse motion of the bike, from where $V_2 = 2V_1,\ x_2 = 2x_1.\ L_{obp} = x_2 + x_1 = 3x_1.$

Knowing the acceleration time of the striker with the accelerator and the valve, as well as their acceleration, we determine the path of the bike acceleration.

Accelerator striker acceleration path and valve: $L_{\text{p}} = \frac{a_p(t_p)^2}{2} = \frac{1}{2}\frac{p_m S_y}{m_b+m_y+m_{kl}} \cdot \frac{K_b(m_b+m_y+m_{kl})}{(p_m S_b)^2}$;

$$L_{\text{p}} = \frac{K_b}{p_m S_b} \tag{33}$$

Next, the linear dimensions of all parts of the DTH hammer can be determined.

The valve motion equation is compiled based on the knowledge of its location by the time of docking with the striker and accelerator. The path traveled by the valve from the moment of its cutoff to the moment of docking with the striker shank is equal to:

$$X_k = a_k {t_k}^2/2 \tag{34}$$

where:

X_k - path traveled by the valve from the moment of its cut-off to the moment of docking with the striker shank, m;

a_k - valve acceleration, m/s^2;

t_k - valve movement time from the moment of its cut-off to the moment of docking with the striker shank, s;

presenting $a_k = F/m_k$ and substituting into equation (9) we get:

$$F/m_k = 2X_k L {t_k}^2 \tag{35}$$

where:

F_k - resulting force acting on the valve, H;

m - mass of the valve, kg.

To fulfill the equality, the ratio of the resulting force acting on the valve to its mass is selected. The resulting force acting on the valve is controlled by changing the flow area of the discharge channel 21 (in the stop of the valve 7), and the mass of the valve by selecting the material from which it is made.

4. Conclusions

The problem of increasing the efficiency has been solved pneumatic impact machines due to a combination of thermodynamic cycles of compressed air expansion in the working chambers of pneumatic impact machines. A fundamentally new design of a down-the-hole hammer has been developed, in which a theoretically substantiated combination of thermodynamic cycles of compressed air expansion is implemented.

The use of simple and effective improvements in constructions makes it possible to increase the efficiency of pneumopercussion machines. These solutions are especially relevant for the mining industry. Within the limited geometrical parameters of the mine workings, it is possible to increase the efficiency of small-scale mechanization significantly, to reduce the cost of final products, and to obtain a sufficient economic effect. The advantages of the innovative solution are as follows:

1. The proposed design of the pneumatic hammer makes it possible to reduce the compressed air consumption by 1.7-1.9 times at the same values of the frequency and energy of blows as in the available pneumatic hammers.

Publisher: **KOMAG Institute of Mining Technology, Poland**

2. Based on this technical solution, DTH pneumatic hammers, rock drills, and other pneumopercussion machines can be created, the use of which in various fields of industry can reduce the cost of drilling and of other types of work significantly.

References

[1] Griadushchiy Y., Korz P., Koval O., Bondarenko V., Dychkovskiy R.: Advanced Experience and Direction of Mining of Thin Coal Seams in Ukraine. Technical, Technological and Economical Aspects of Thin-Seams Coal Mining, International Mining Forum 2007: 2-7. https://doi.org/10.1201/noe0415436700.ch1

[2] Kolb A., Pazynich Y., Mirek A., Petinova O.: Influence of voltage reserve on the parameters of parallel power active compensators in mining. E3S Web of Conferences 2020, 201: 01024. https://doi.org/10.1051/e3sconf/202020101024

[3] Hankevich V., Moskalova T., Kabakova L., Livak O.: The feasibility evaluation of using cyclic thermal effect in the rock-cutting tools during drilling hard rock. E3S Web of Conferences 2019, 109: 00026. https://doi.org/10.1051/e3sconf/201910900026/

[4] Dychkovskyi R.O., Avdiushchenko A.S., Falshtynskyi V.S., Saik P.B.: On the issue of estimation of the coal mine extraction area economic efficiency. Naukovyi Visnyk Natsionalnoho Hirnychoho Universytetu2013, 4: 107-114

[5] Lipin A.A.: Down-the-hole hammers with combined air distribution. Machine science 2007, 2: 43-47

[6] Nadutyi V. P., Kurilov V. S., Cholyshkina O. G., Hankevych V. F.: Analytical studies on constrained particle settling velocity in a water suspension of fly ash from thermal power plants. Naukovyi Visnyk Natsionalnoho Hirnychoho Universytetu 2021, 1: 32–38. https://doi.org/10.33271/nvngu/2021-1/032

[7] Dychkovskyi R.O.: Forming the bilayer artificially created shell of georeactor in underground coal well gasification. Naukovyi Visnyk Natsionalnoho Hirnychoho Universytetu 2015, (5): 37–42

[8] Golovchenko A., Dychkovskyi R., Pazynich Y., Edgar C. C., Howaniec N., Jura B., Smolinski A.: Some Aspects of the Control for the Radial Distribution of Burden Material and Gas Flow in the Blast Furnace. Energies 2020, 13(4): 923. https://doi.org/10.3390/en13040923

[9] Alekseev S.E., Repin A.A., Pyatnin A.A.: Creation and introduction into production of powerful DTH pneumatic hammers. Machine science2007, 2: 9-13

[10] Dychkovskyi R., Tabachenko M., Zhadiaieva K., Dyczko A., Cabana, E.: Gas hydrates technologies in the joint concept of geoenergy usage. E3S Web of Conferences 2021, 230: 01023. https://doi.org/10.1051/e3sconf/202123001023

[11] Kosolapov D.V.: Features of dynamic calculations of details of downhole pneumatic hammers. Safety and survivability of technical systems 2009, 9: 171-175

[12] Sobolev V., Bilan N., Dychkovskyi R., Caseres Cabana E., Smolinski A.: Reasons for breaking of chemical bonds of gas molecules during movement of explosion products in cracks formed in rock mass. International Journal of Mining Science and Technology 2020, 30(2): 265–269. https://doi.org/10.1016/j.ijmst.2020.01.002

[13] Lipin A.A.: Promising pneumatic hammers for drilling wells. Physical and technical problems of mining. 2005, 2: 176 -199

Publisher: **KOMAG Institute of Mining Technology, Poland**

https://doi.org/10.32056/KOMAG2022.4.4

Stress measurements at load-bearing components of the shaft steelwork and the mine hoist frame in the Regis Shaft of the Wieliczka Salt Mine

Received: 06.10.2022

Accepted: 17.11.2022

Published online: 30.12.2022

Author's affiliations and addresses:

[1] Elektrometal S.A.,
Stawowa 71, 43-400 Cieszyn,
Poland

[2] Wieliczka Salt Mine S.A.
Daniłowicza 10, 32-020 Wieliczka,
Poland

[3] AGH University of Science and Technology, The Department of Machinery Engineering and Transport Faculty of Mechanical Engineering and Robotics,
al. Mickiewicza 30,
30-059 Krakow, Poland

*** Correspondence:**

e-mail: konewecki@gmail.com

Artur KONEWECKI [1, 3*], Krzysztof ROZWADOWSKI [2], Rafał PASEK [2], Szymon MOLSKI [3]

Abstract:

The study summarises the selection of dedicated techniques and procedures for measuring real stresses arising in shaft steelwork components due to car-shaft steelwork interactions as well as stresses at critical points of the car frame in the elevator installation in the Regis Shaft of the Wieliczka Salt Mine. The implemented solution and operational parameters of the hoisting installation in the Regis Shaft of the Wieliczka Salt Mine are summarised, the adopted measurement method and dedicated equipment are presented, focusing on the procedure for locating the critical points on the car frame and shaft steelwork. The purpose-built measurement set-up as well as the adopted stress measurement procedure and results are explained in detail.

Keywords: measurements, hoisting installation, mine elevator, stress, shaft steelwork, elevator car frame

1. Introduction

With the plans to open a new tourist route "The Miners' Route", in anticipation of growing numbers of visitors to the site and aiming at improving the visitors' comfort and to adapt the facility to the needs of disabled visitors, the managers of the Wieliczka Salt Mine were in quest for safer and more economic means of transportation for visitors.

Following an in-depth analysis of formal requirements as well as technical and financial aspects, the management had two independent, single-door men-riding elevators installed in place of the traditional mine shaft hoist. This solution ensured better safety for passengers and well performed its function as a facility providing the effective transport of tourists in groups of 15, visiting the newly-opened site and entering through the Regis Shaft [1]. Two elevators were therefore installed in the shaft, each having the load-bearing capacity of 1600 kg or 21 persons. These are automatic, self-service elevators, and the access and maintenance operations are supervised via a dedicated electronic access-control system.

Since the elevators, installed in the Regis shaft, replaced the previously operated mine shaft hoist, all maintenance jobs, shaft inspections and testing of wall-mounted equipment in compliance with the current mining law are conducted whilst the elevator is running on inspection mode with the servicemen riding on top of the elevator car, and the travel is controlled from the control console on top of the car. A canopy is provided to shield the servicemen during the shaft inspection and equipment testing on top of the elevator cars.

2. Research methods

2.1. Elevator construction

Two PT21/40-19 elevators, used for hoisting personnel and materials, were installed in the northern and southern sections of the shaft [2].

The main components of each elevator facility include:

- Machine room 4400 mm in length, 4280 mm in width and 2700 mm in height, located on the level +9.27, with two identical drive units comprising a gearless winch MX18 with the friction pulley 690 mm in diameter, the LCE control panel, the drive panel MLB, two sets of rope slings for each elevator and overspeed governors for adjusting the speed of both the elevator car and counterweights;
- Elevator car-slide-guided on two rigid guide bars with roller guides;
- Counterweight sliding on two rigid guide bars with roller guides,
- 6 hoisting ropes to handle the elevator car, having the structure 8x19S-NCF 1570 PAWO F3 and diameter of 13 mm,
- 7 tail ropes in the hoisting machine 8x19 W 1570 PAWO F7, Ø16 mm in diameter.

In order that the shaft top facility should remain as a heritage asset, the conservation officer decreed that the winding tower +24.26 m high, located on the level +21.05 m and housing rope pulleys, should be brick-lined and maintained as a piece of architecture (Fig. 1).

Fig. 1. The top of the Regis Shaft [3]

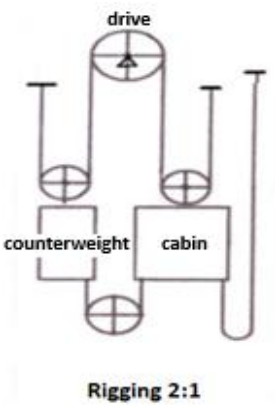

Fig. 2. Kinematic diagram of the elevator [3]

Publisher: **KOMAG Institute of Mining Technology, Poland**

The elevator in the northern-end section has three stops: on pit bank level +0.00 m, in the pit bottom on the level of rope drive sheave at -106.96 m, on the pit bottom level III at -127.65 m. The elevator system in the south-end of the shaft has four stops: at the shaft top at +3.42 m, on the pit bank level at +0.00 m, in the pit bottom level I at -57.94 m and level III at 127.65 m. A simplified kinematic diagram of elevators installed in the two shaft compartments is shown in Fig. 2.

A general view of the machine room is shown in Fig. 3 and the hoist shaft with wall-mounted equipment is shown in Fig. 4. Fig. 5 gives a vertical cross-section of the top part of the hoist tower, a view of the machine room and the upper section of the shaft.

Fig. 3. Machine room with installed gearless winches MX18 with the friction pulleys 690 mm in diameter [3]

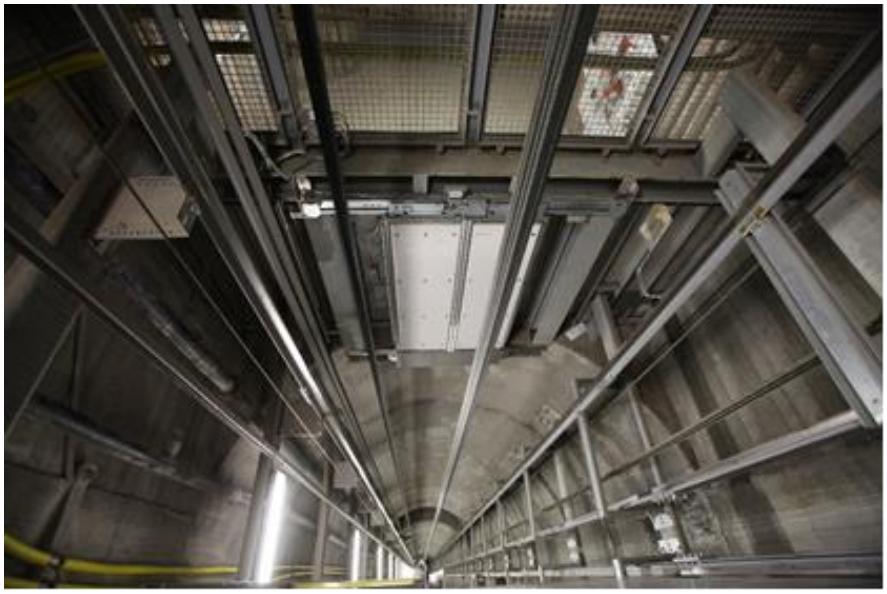

Fig. 4. The shaft with mounted guide bars – general view [1]

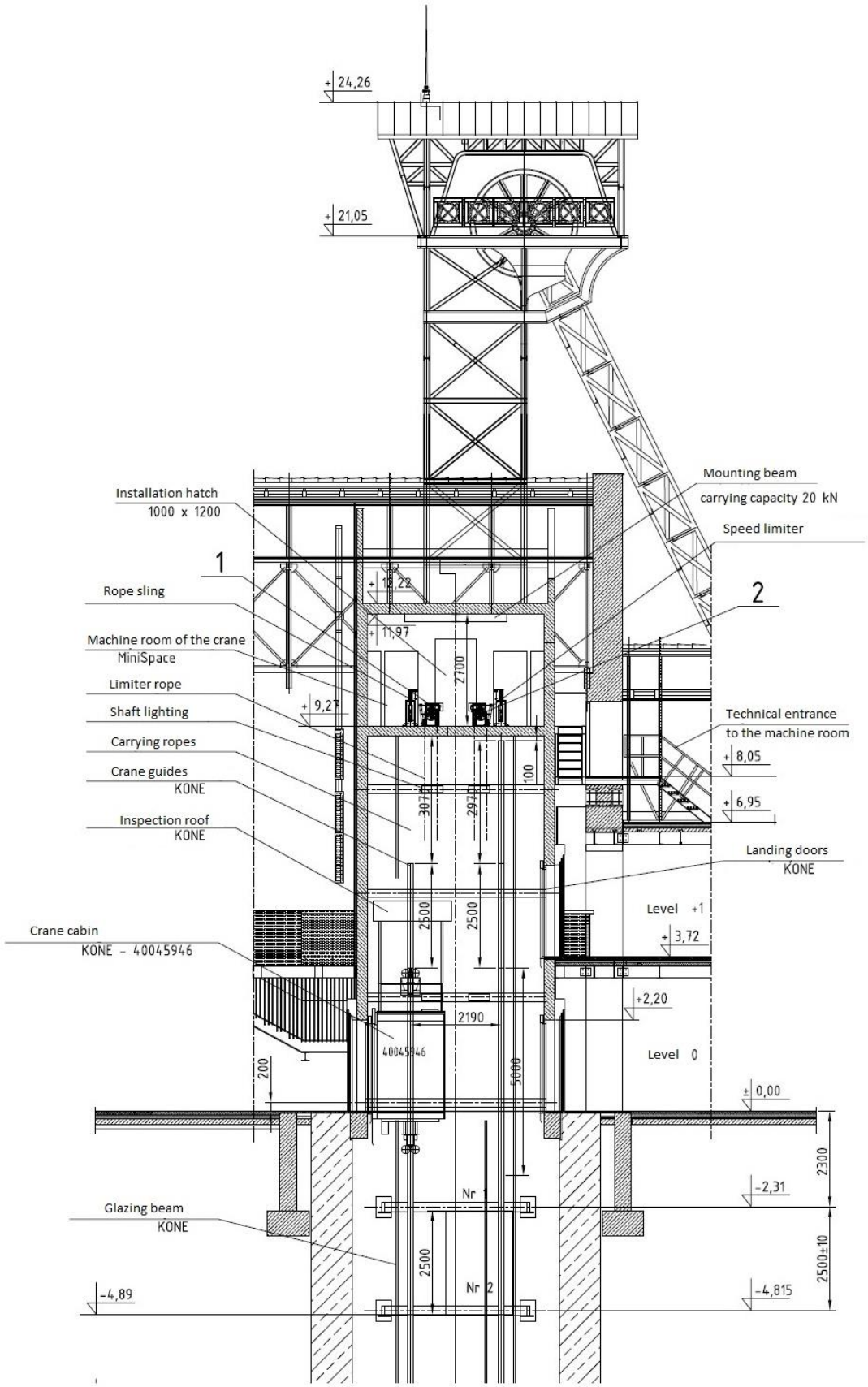

Fig. 5. Vertical section of shaft top facility and machine room [4]

2.2. Shaft steelwork

The shaft steelwork and wall-mounted equipment in the Regis Shaft are designed to support the guide bars to enable the slide-guiding of elevator cars and counterweights and to hold the station doors of KONE elevators for hoisting personnel and materials between the shaft bottom levels I, II, III.

The present positions of the elevator cars and counterweights and wall-mounted equipment within the shaft are shown in Fig. 5.

The critical components of the steelwork structure in the Regis Shaft between the pit bank level (+0.00 m) down to the level III (-127.65 m) are buntons spaced every 2.5 m, a safety deck on the shaft sump level (-132.12 m) with reversal stations for balance ropes provided with tension weights and devices used to keep the elevator car and counterweight overspeed governor ropes under tension, a control deck on the shaft sump level (an artificial shaft bottom) on the level -135.43 m.

Other components of the steelwork structure in the Regis Shaft include:

- chair mechanism on the pit bottom level I;
- shaft entry lock with the load-bearing structure on the level IIw,
- chair mechanism on the pit bottom level IIn;
- chair mechanism on the pit bottom level III;
- ladder compartment from level III to IV;

The diagram cross-section of the Regis shaft with wall-mounted equipment is shown in Fig. 6. The shaft with installed guide bars and other shaft fittings is shown in Fig. 4.

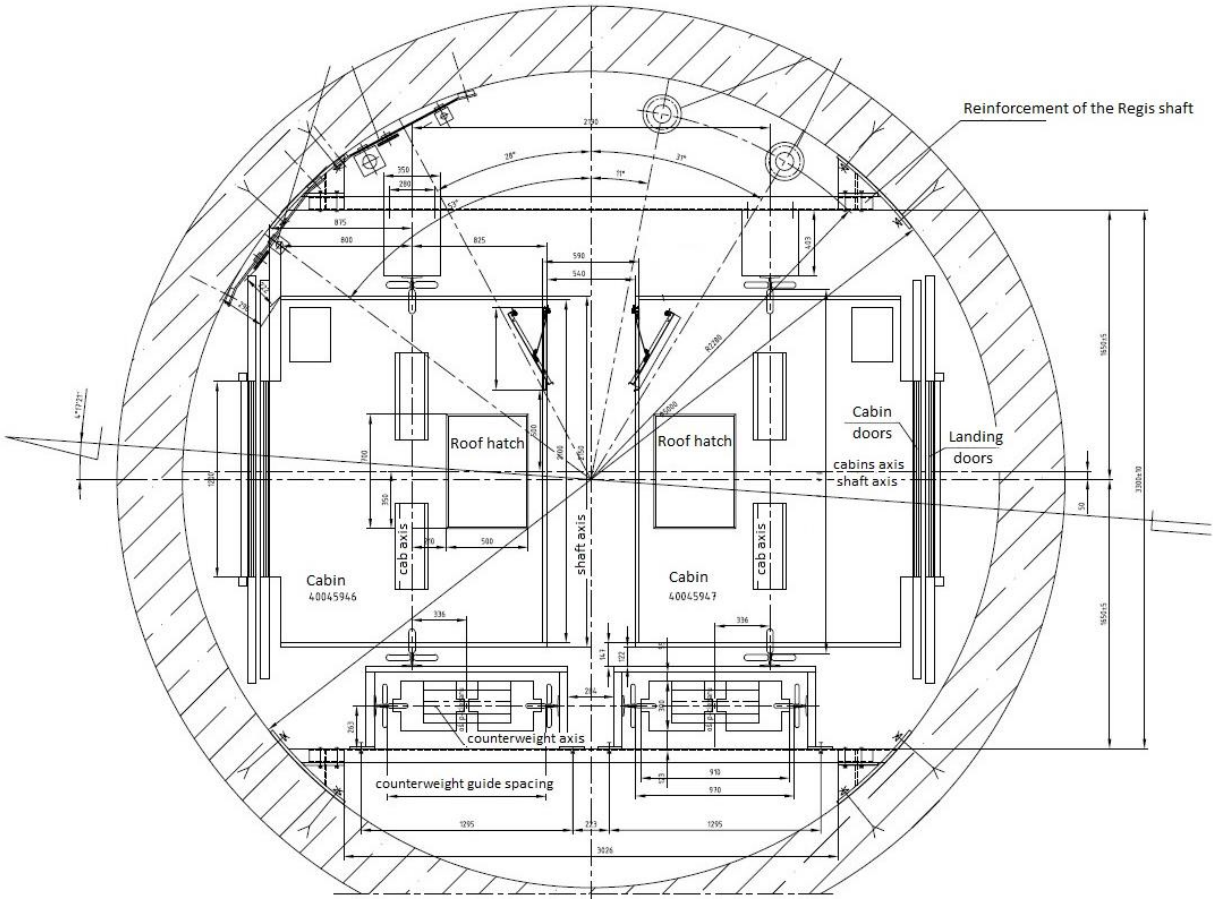

Fig. 6. Cross-section of the Regis Shaft with wall-mounted equipment [5]

2.3. Technique selection

In the course of research work the underlying assumptions relating to structural durability and endurance of the hoist frame and supporting beams in the Regis Shaft had to be verified. It was established that measurements with the use of electric resistance wire strain gauges would be the optimal technique for measuring stresses, displacements and deformations of the hoist frame structure or the supporting beams. Since the hoist mainframe and the guiding system are encased within a vertical pit alongside the elevator carrying the visitors and operated in the continuous mode, all laboratory methods of stress measurement had to be abandoned.

Obvious advantages of electric resistance strain gauges and feasibility of using a recorder equipped with a signal amplifier rendered this measurement set-up an optimal option for use in conditions prevailing in the Regis Shaft of the Wieliczka Salt Mine. An electric resistance strain gauge is firmly attached to the surface of the structure under testing with dedicated glue that is sufficiently elastic to allow an undisturbed operation of the strain gauge and an interaction with the surface under testing.

The measurement set-up, deployed in the shaft, was based on the CL460 recorder (model 1.51) designed to perform simultaneous high-precision measurements and recording of physical quantities to be converted into electrical signals with the use of strain gauges in the quarter-bridge configuration, current transducers with 4-20 mA output or potentiometer sensors [6]. Data analysis was supported by a dedicated software for recording and visualisation of signals. The device had 16 analogue channels to interconnect 16 adapters of strain gauges in the quarter-bridge configuration. Fig. 7 shows the position of analogue channel outputs. A resolution of measurements, conducted in the quarter-bridge configuration is 1μm/m, allowing infinitesimal stress changes to be registered.

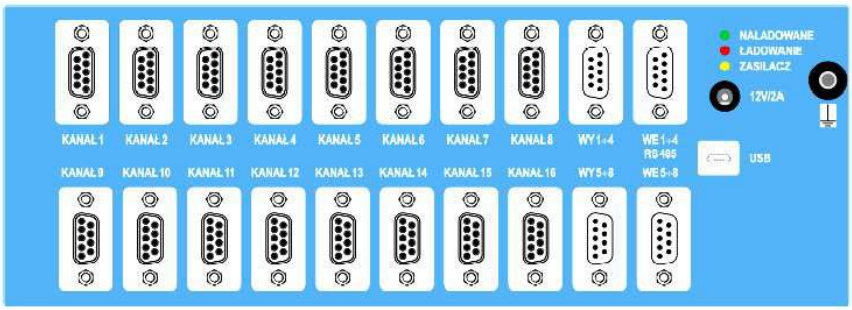

Fig. 7. Rear side of the CL460 recorder [7]

Measurements were taken with BCM strain gauges with the resistance 350.9 Ω and constant sensitivity 2.12+1%. The strain gauge in the quarter-bridge configuration was connected via a cable DY LIFYDY 4x0.04 mm^2. Adapters were directly connected to one of the 16 analogue channels equipped with RS-485 connectors, the present configuration of the strain gauge connection is shown in Fig 8.

The measurement set-up did not provide for compensation of the effects of temperature because the ambient temperature in the proximity of the hoisting installation remained stable, between 15 and 16°C.

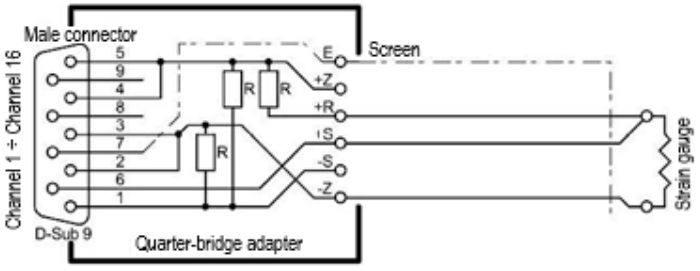

Fig. 8. Schematic diagram of the strain gauge connection to the quarter-bridge adapter [6]

2.4. Selection of measurement points

The elevator car frame is the CF25(TP) model complete with two rope sheaves. Preliminary FEM analyses revealed the critical points on the car frame where maximal stress concentrations should be anticipated. In the first place an array of strain gauges was attached to the roof beam in the elevator car frame (item 1 in Fig. 9). Three strain gauges fixed at this point are mounted at 120° in relation to each other. The second test point was located on the pull rod (item 2 Fig. 9), the third point on the car frame is located on the floor beam (item 3 Fig. 9). Designations of strain gauges mounted on the car frame are summarised in Table 1.

Table 1. Designations of strain gauges mounted on the car frame

Designation	Device	Position
P1	Strain gauge 1	Roof beam (item 1 Fig. 9)
P2	Strain gauge 2	
P3	Strain gauge 3	
P4	Strain gauge 4	Pull rod (item 2 Fig. 9)
P5	Strain gauge 5	Floor beam (item 3 Fig. 9)
P6	Strain gauge 6	
P7	Strain gauge 7	

Alongside strain measurements in the elevator car frame, measurements of increasing stresses on supporting beams were taken as well. In the tested elevator, there are two beams T125xB2x16B supporting the elevator car, made of material with the strength Rm=440 MPa. They support the guide bars and transmit loads onto the buntons whence they are directly transferred to the shaft lining. The supporting beams must be capable of bearing the maximum loads acting on the guide bars. Positions of selected control points on the supporting beam are shown in Fig. 10 and designations of mounted strain gauges are summarised in Table 2.

Table 2. Designations of strain gauges mounted on the supporting beam

Designation	Device	Position
Q1	Strain gauge 1	See Fig. 10, item 4
Q2	Strain gauge 2	
Q3	Strain gauge 3	
Q4	Strain gauge 4	See Fig. 10, item 5

Before the strain gauges were attached to the elevator car frame and to the supporting beams, the corrosion–protection coating had to be removed from their surface by polishing with silicon carbide sandpaper, grit range from 100÷400, to achieve as smooth and even surface as possible, free from corrosion pits and mechanical losses. All strain gauges, being attached at selected points, their leads were soldered to the quarter-bridge adapter. A view of strain gauges fixed at selected points on the car frame and supporting beam is shown in Fig. 11.

Publisher: **KOMAG Institute of Mining Technology, Poland**

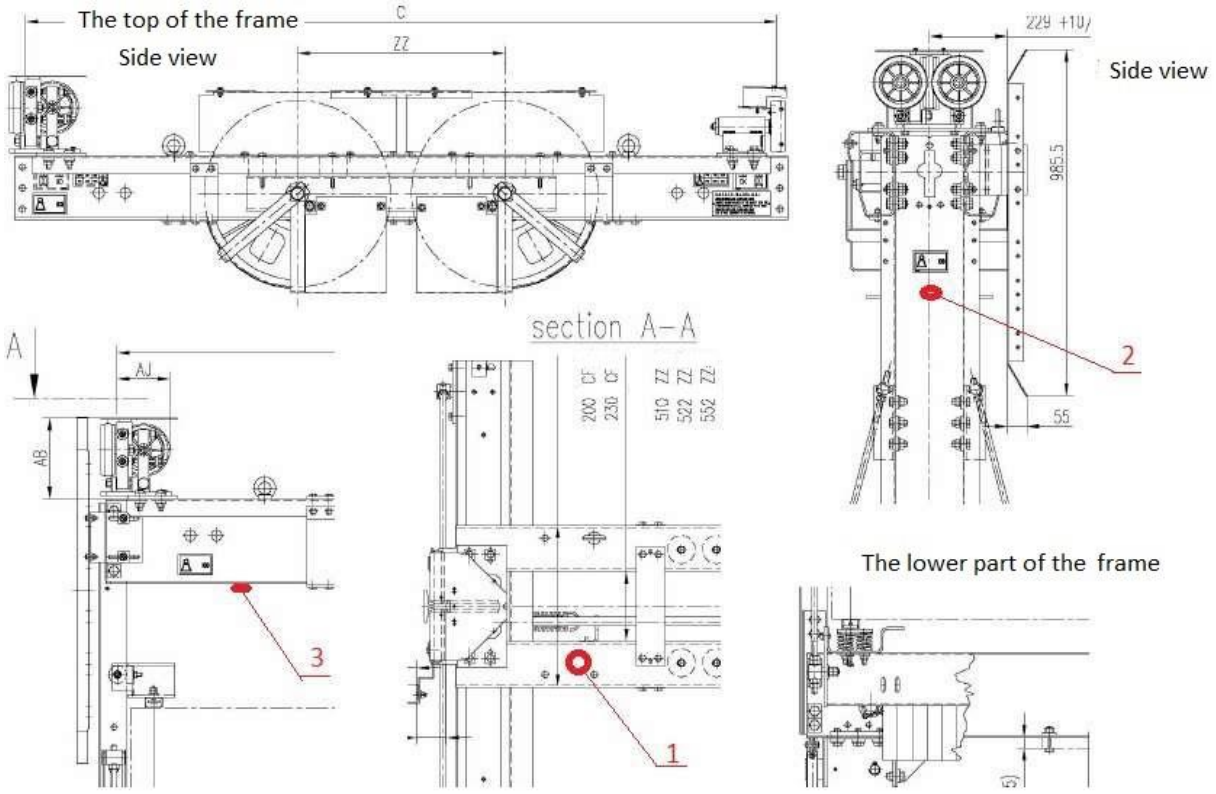

Fig. 9. Positions of control points on the frame of the elevator car (model CF25(TP) [3]

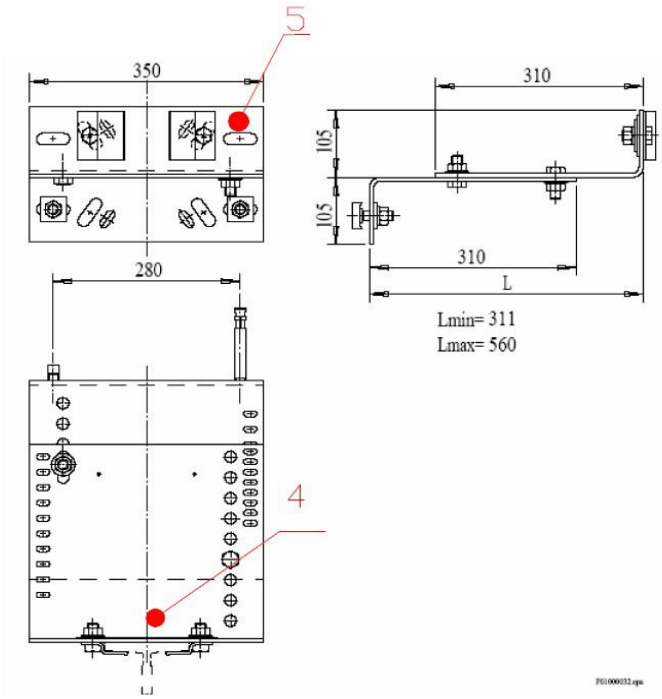

Fig. 10. Positions of control points on the east-end supporting beam [3]

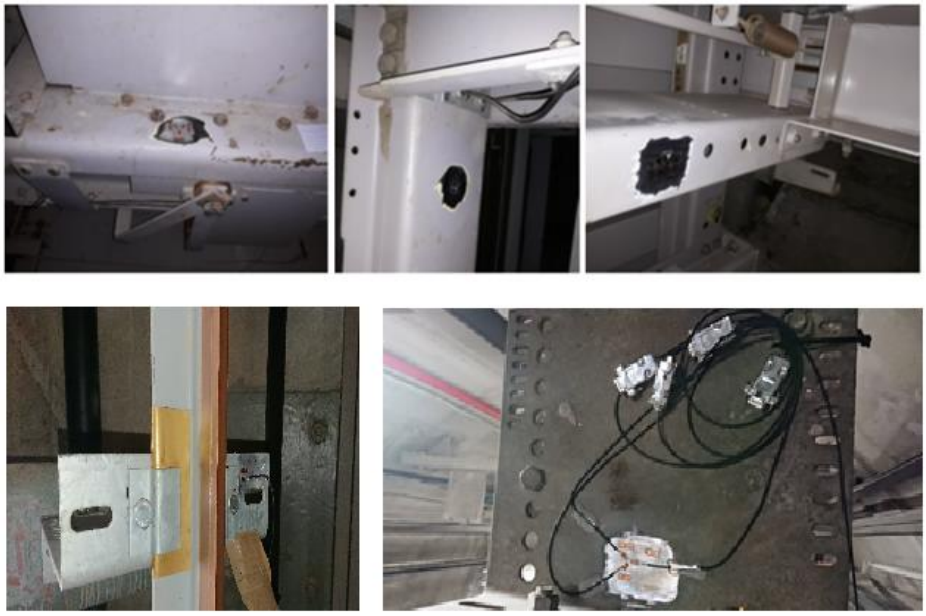

Fig. 11. Strain gauges attached to the selected points on the car frame and east-end supporting beam [3]

3. Measurement results

An array of strain gauge was mounted on the car frame at points shown in Fig. 9 and anticipated stress increases were defined accordingly. The first place, where the strain gauges, were attached was the roof beam in the car frame (item 1 in Fig. 9), with three strain gauges designated as P1, P2, P3 mounted at 120° in relation to each other. A stress increase is anticipated at this point due to the action of the gravity force, the weight of the car frame with fittings and the rope self-weight load. The second measurement point has one strain gauge, designated as P4, mounted on the pull rod in the car frame (item 2 in Fig. 9). The third point is located on the floor beam in the car frame, where three strain gauges, designated as P5, P6, P7, were mounted at 120° in relation to each other (item 3 in Fig. 9).

Locations of measurement points on the supporting beam are shown in Fig. 10.

Measurement points, located on the supporting beam, are shown in Fig. 10. Strain gauge positions were defined in a similar way to those on the car frame, i.e. in terms of anticipated stress increases. On the supporting beam an array of three strain gauges were mounted at 120° in relation to each other at point 4 (see Fig. 10). At point 5 (Fig. 10) there is a single strain gauge mounted on the front surface of the support beam. A view of fully mounted and connected strain gauges is given in Fig. 11. It is anticipated that during the standard elevator operation the forces normal to the car frame might arise at this point and that the supporting beam might be subject to bending and torsion. Besides, the forces acting on the sides of guide shoes, which may cause the beam to bend in the opposite direction, might arise.

The first series of car frame tests were conducted during the ride at nominal speed. The standard hoisting speed during the normal operation was 4 m/s, with no load carried Q=0.0 kg. Fig. 12 plots the stress increase registered by individual strain gauges during the ride from the bank level station 1 down to the level – 135 m.

Publisher: **KOMAG Institute of Mining Technology, Poland**

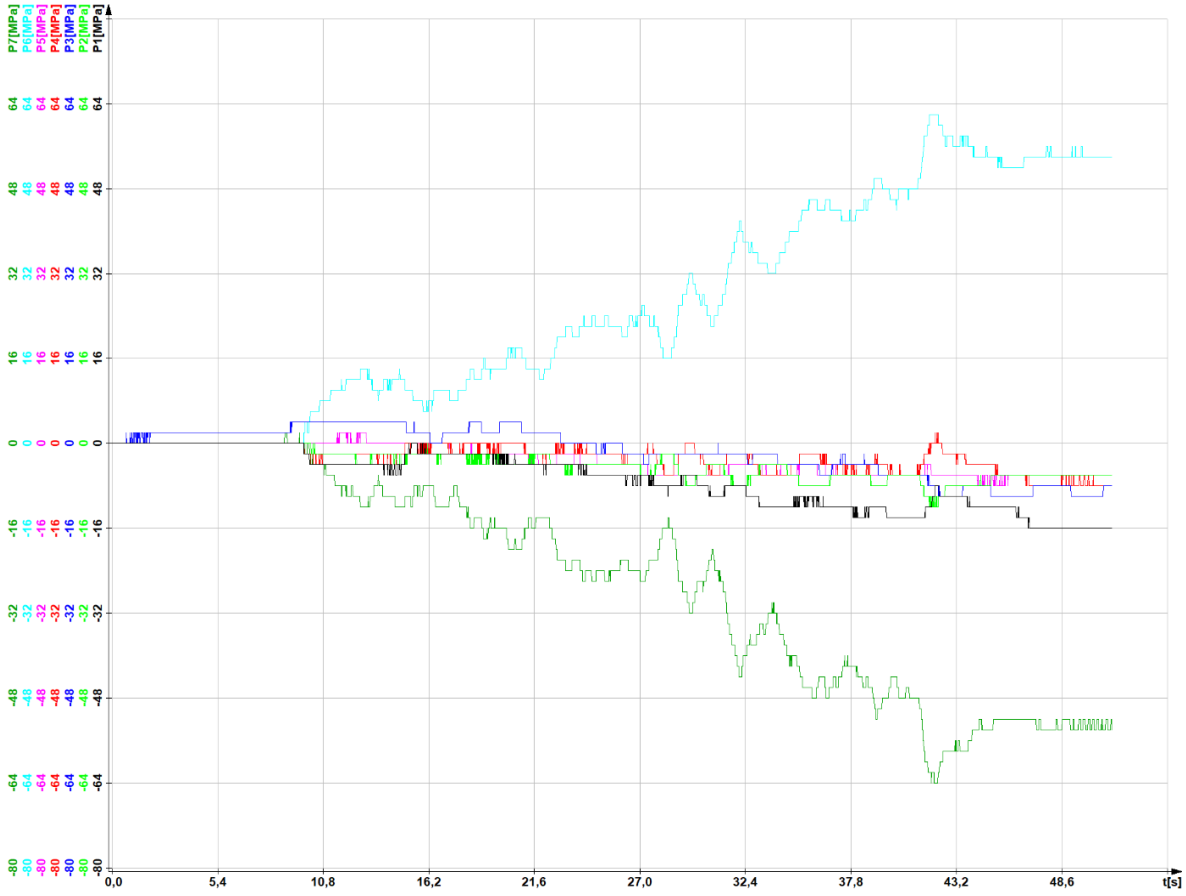

Fig. 12. Downward ride of the elevator car at 4 m/s, with no load [7]

During the first 9 seconds minor stress changes are registered by strain gauge 3, that is the time when the car doors and station doors are opened and closed. Afterwards, the elevator is started and the car begins to ride downward. Successively, with the metres travelled the stress tends to increase, which is registered by strain gauges P6 and P7. These stress increases result from the changes in loading due to the tail rope self-weight and the floor beam may experience slight bending and torsion. Forces and moments of forces that cause this effect are due to the changes of tail rope weight and tail rope motions. In the period from 43rd and 47th second, the car decelerates before reaching the bottom level station. Between the 47th and 49th second an opening of car doors occurs. The further part of the graph does not need to be considered because it reveals disturbances associated with the servicemen entering the car.

In the second series of tests, the elevator car travelled with the maximal load in the standard ride mode at 4 m/s, carrying the load of Q=1600 kg. Fig. 13 shows the results registered throughout 10 cycles of the car ride with the maximal values of operating parameters designed for this model of the elevator.

Publisher: **KOMAG Institute of Mining Technology, Poland**

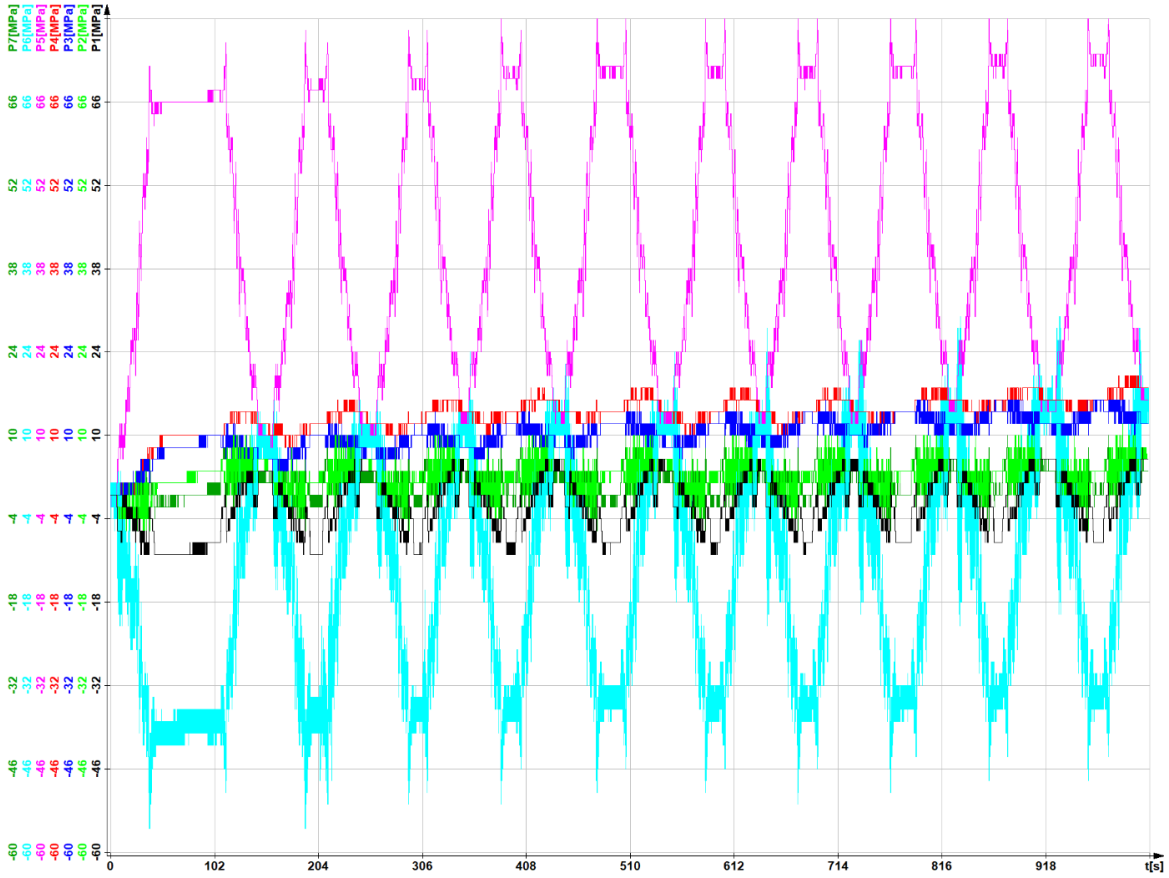

Fig. 13. 10 cycles of elevator car ride at v=4 m/s, with full load [7]

It is worthwhile mentioning that the maximal stress increases were registered again by strain gauges mounted on the floor beam, especially by P5 and P6, which is indicative of torsional moments arising due to tail rope self-weight load, and of the acting bending forces due to elevator car loads. The maximal stress increases tend to oscillate, fully revealing the impacts of the dynamic behaviour of the system. While the elevator stops, the stress tends to decrease until the momentary change of sign in the final stage of deceleration, which is readily apparent between the duty cycles, especially in readouts from strain gauge P6.

With regard to the supporting beam, measurements were taken during the elevator car ride at full speed v=4 m/s and with full load Q=1600 kg. Fig. 14 plots the results registered throughout 10 cycles of the car ride from the bank level station 1 (0.00 m) down to -135 m, with the maximal values of operating parameters designed for this model of the elevator. Apparently, stress variation patterns, registered by the strain gauge Q4 mounted on the front surface of the supporting beam, agree well with the made assumptions relating to the occurrence of forces acting perpendicularly to the shaft axis, causing the vertical plane of the support beam to bend. The maximal values of registered stress variations are about 28 MPa. On the horizontal plane of the supporting beam, where strain gauges Q1, Q2, Q3 are installed, the most significant stress changes were registered by strain gauge Q1 (around 50 MPa). This stress component gives rise to the beam torsion in the direction coinciding with the elevator ride and that is also in line with the underlying assumptions.

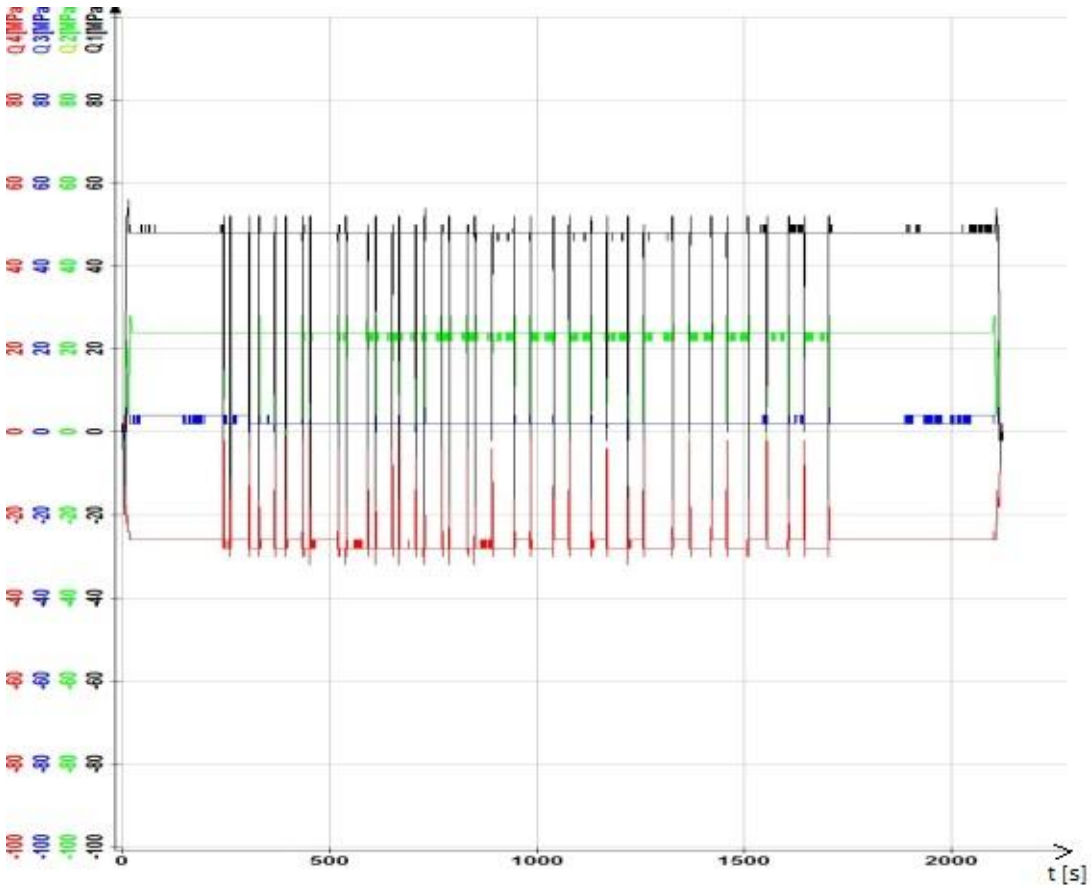

Fig. 14. 10 cycles of elevator car ride at v=4 m/s, with full load [7]

4. Conclusions

The analysis of measurement results reveals slightly increased stress levels in the examined structural components of the elevator installation. In most cases stress increases, registered in the car frame during the hoisting operation, should not exceed 60 MPa, whilst the stresses in the beam supporting the guide shoe rise by about 50 MPa, generating the bending and torsion effect.

Apparently, increased stress levels can also result from a misalignment of the guide string, and this parameter ought to be taken into account in structural integrity and fatigue endurance calculations. Considering the specifications of the car frame material and the fact that the supporting beam is made of carbon steel, grade S235JR (according to PN-EN 10025), with Re=235 MPa and Rm=340 MPa, it is reasonable to hypothesise that the examined car frame and supporting beam should operate well below the endurance limit, (see the S-N curve for the given steel grade).

To verify this hypothesis, computer-assisted model tests are required, based on the FEM approach in the linear range [8].

Should the stress components exceed the respective values Zgo=153 MPa, Zro=112 MPa, Zso=85 MPa, the full endurance analysis of the car frame and the supporting beam will be useful. In such a case the endurance analysis will help to determine the life of the tested system in relation to the number of repeated loading cycles.

References

[1] Zuski Z, Czyżowski J, Wójcik M.: Man/material hoists for transportation in vertical shafts in the Wieliczka Salt Mine. Part II: Installation and commissioning of man/material hoists for transportation in vertical shafts, in the Regis shaft of the Wieliczka Salt Mine (in Polish)

Publisher: **KOMAG Institute of Mining Technology, Poland**

[2] KONE Ltd. Engineering specification of man/material hoists, project No 6203620. Warsaw, 2009 (in Polish)

[3] Rozwadowski K., Konewecki A., Molski Sz., Pasek R., Zuski Z.: Aspekty metrologiczne procesów pomiarowych wybranych elementów instalacji dźwigowej zaimplementowanej w szybie górniczym *(Metrological aspects of measurements of selected structural elements of the hoisting installation implemented to mine shaft),* In: KOMTECH 2020, Innowacyjne techniki i technologie dla górnictwa. Bezpieczeństwo - Efektywność - Niezawodność, Instytut Techniki Górniczej KOMAG, Gliwice 2020, pp. 93-110, ISBN 978-83-65593-22-1 (in Polish)

[4] Project No P 191/2009 "Reconstruction and modernisation of the pit head in the Regis shaft" developed by Architectural Project Agency (Agencja Projektowa Architektury) EKSPO SC, Kraków (in Polish) (unpublished)

[5] Krupa P.: Commissioning documentation for special transport facilities in the Regis Shaft. Wieliczka Salt Mine, 2012.International Conference in Safety of Mine Hoist Installations, Ustroń 2012. (In Polish)

[6] Rozwadowski K., Konewecki A., Molski Sz., Pasek R.: Analiza pomiarów zmian naprężeń ramy kabiny i wybranych elementów zbrojenia szybowego instalacji dźwigowej zabudowanej w szybie górniczym „Regis" w Kopalni Soli Wieliczka *(Analysis of the results of measurements of changes in the stresses of the cabin frame and selected elements of the shaft reinforcement of the lift implemented in the "Regis" mining shaft in the Wieliczka Salt Min),* In: KOMTECH 2021, Innowacyjne techniki i technologie dla górnictwa. Bezpieczeństwo - Efektywność - Niezawodność, Instytut Techniki Górniczej KOMAG, Gliwice 2021, pp. 24-35, ISBN 978-83-65593-27-6 (in Polish)

[7] User's Manual for the CL 460 recorder (ZEPWN) (in Polish); https://www.cms.zepwn.com.pl/zepwn/_media/products/pdf-pl/karta_cl460_2015_02_10.pdf [accessed: 20.09.2022]

[8] Lonkwic P., Molski S.: Zastosowanie numerycznej metody wykorzystującej punkty aktywne w obliczeniach naprężeń spawalniczych (*Application of the numerical method based on active points to welding stress calculations*). Obróbka metalu, 2019, 3, 56-59 (in Polish)

https://doi.org/10.32056/KOMAG2022.4.5

A tool for determining the number of bends and places of accumulation of potential wear of steel ropes operating in the luffing systems of basic opencast mining machines

Received: 04.11.2022

Accepted: 06.12.2022

Published online: 30.12.2022

Author's affiliations and addresses:

[1] AGH University of Science and Technolology, Faculty of Mechanical Engineering and Robotics, Department of Machinery Engineering and Transport, al. Mickiewicza 30, 30-059 Krakow, Poland

*** Correspondence:**

e-mail: olszyna@agh.edu.pl

Grzegorz OLSZYNA [1*], Andrzej TYTKO [1]

Abstract:

This article presents the issues of the wear of steel ropes operating in the lowering systems of the largest wheel excavators (BWE), type SchRs, Rs, KWK operating in KWB Bełchatów. Sudden degradation of these ropes may lead to the complete shutdown of the BWE-Belt-Stacker system from operation. However, this can be avoided by regular visual inspections of hoist ropes. Unfortunately, the rope systems in each excavator are different, and their availability is difficult. In order to simplify this task, the authors of this paper have developed an IT tool that allows the modelling of a given multi-pulley rope system and the indication of critical places on the rope for given working conditions. A simplified description of this tool is the subject of the article.

Keywords: opencast mining, steel ropes, rope modelling, rope wear

1. Introduction

In the last few years, in the European Union, as well as in Poland, the discussion on thermal energy based on coal raw materials has definitely shifted towards low-carbon and renewable sources. In Poland according to the Central Statistical Office [1] and forecasting for the future [2], almost 50% of electricity is produced from lignite, including pprox. 24% in the Bełchatów power plant and mine complex. There is a clear retreat from these classic carriers, while the government of the Republic of Poland does not outline at least short development prospects how to do it.

The outbreak of war and the economic consequences of the Russian Federation's attack on Ukraine radically changed the European and global approach to the problems of energy production in general. The discussion on coal-based energy is no longer so radically negative. Nevertheless, several years of uncertainty regarding the future of lignite mining, the complete lack of investment and the inevitable ageing of the unique set of basic machines [3] for lignite mining may lead to various failures in the future.

This article presents the issue of wearing the steel ropes used in the lowering systems of the largest wheel excavators (BWE), type SchRs, Rs, KWK working in KWB Bełchatów mine. Fig. 1 shows one such a machine with a rigging system of the lifting system of the cutting wheel boom.

Fig. 1. Bucket-wheel excavator SchRs4600 of KRUPP

Degradation of the hoisting ropes may eliminate the excavator-belt conveyor-stacker (KTZ) system from operation. However, this can be avoided by regular visual inspections of the rope hoisting systems [4]. Fig. 2 shows the kinematic diagrams of such machines together with the rigging systems.

Publisher: **KOMAG Institute of Mining Technology, Poland**

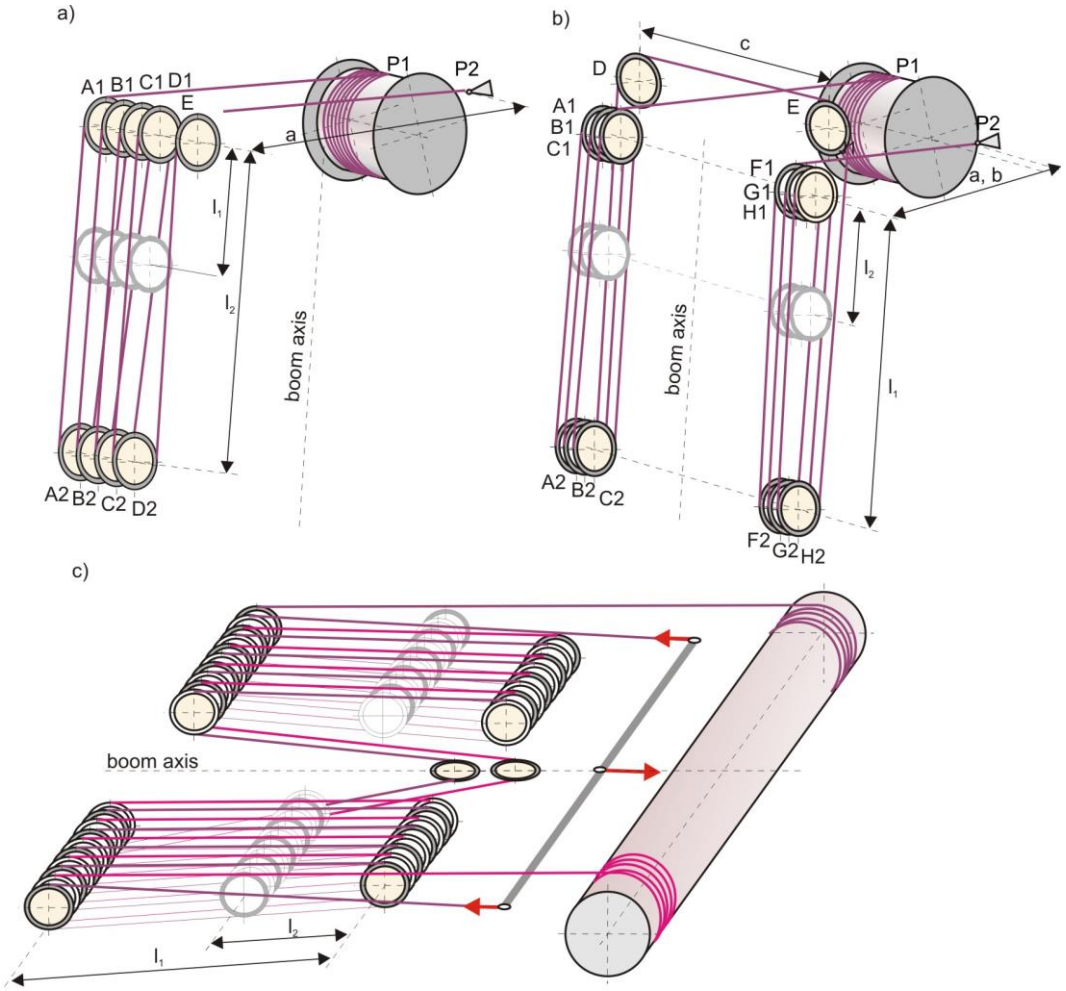

Fig. 2. Kinematic diagrams of rigging systems for machines with a cutting wheel: a) excavator SchRs1200, b) excavator SchRs4000, c) excavator SRs2000 [5]

Unfortunately, the hoisting rope systems in each excavator have a different geometry and number of pulleys [4], and the accessibility of ropes in the hoisting systems for visual assessment is difficult. Periodic magnetic tests are not carried out, and the condition of the ropes is assessed on the basis of random visual inspection of a foreman or a person authorized by the surveillance unit. But this inspection is made only from easily accessible locations, and these do not always include high-loaded parts which are subjected to wear and tear. A simplification of this task is an IT tool developed by the authors of this article in the form of a calculator, which allows modelling the given pulley system on the basis of identified critical places on the lines for the given working conditions. A simplified description of this tool [6] is the article subject.

Publisher: **KOMAG Institute of Mining Technology, Poland**

2. Testing methodology

2.1. Reasons for the wear of hoisting ropes in the luffing systems of excavators in the opencast mining industry

Roller pulley systems are the systems for lifting or lowering masses suspended from movable pulley blocks, moving with the use of steel ropes, wound on driving drums and rolling on rope sheaves (wheels). In these systems, the steel ropes, while rolling on the rope sheaves, contact the sheave through the raceway of the appropriately shaped groove. In these systems, we deal with the action of longitudinal forces in the ropes, bending of the rope on the pulleys and phenomena in the area of the rope contact with the pulley groove raceway. In addition, there are loads, mainly of a random nature, from vibrations that are damped at the entrance of each rope section to the pulley. Such action gives rise to three wearing symptoms. The most important is the mass loss wear of the rope, characterized by a local change in the rope cross-section area. In fact, these are the abrasions of its external wires due to friction against the raceway of the rope sheave. The abrasion is visible as an ellipse formed on the wire surface, which affects the strength properties of the wire [7]. Abrasive wear also occurs inside the rope as a result of the movement of strands and wires with the simultaneous occurrence of point contact pressure (Hertz pressure). This process is largely influenced by the cleanliness and quality of the lubricant [8]. The second extremely important cause of the wear of lifting ropes are plastic deformations caused by increased pressure between the rope and the groove of the rope pulley. The pressure leads to abrasive wear and also to plastic deformation wear, leading to wire breakage (crushing). These deformations in specific contact conditions can also lead to the formation of such high pressures that martensitic structures are formed on the outer layer of the outer wires. Due to their brittleness, these structures can cause premature fatigue cracks in the outer wires of the rope. This damage has a different effect on the weakening of the rope. The loss in the metal rope cross-section area due to the abrasion processes may not exceed 2% of the original rope cross-section area [9]. Abrasive wear is closely related to the operating conditions of the ropes and to the pulleys linings. The process of abrasive wear is more noticeable on hard and abrasion-resistant wires [10]. In opencast mining excavators, due to their short operation and good lubrication, no corrosive mass losses nor excessive fatigue wear leading to premature disqualification of the rope were observed.

Another important factor leading to rope wear in the hoisting system of an excavator cutting wheel is cyclical deformation of the rope geometry during lifting the cutting wheel, when the length of each rope branches between the upper and lower pulleys is shortened during lifting. The stroke length of the working rope is reduced. This reduction may lead to the occurrence of a torque moment which, by eliminating the frictional forces on the pulley, may transfer to the next rope branch outside the pulley. As a result, these changes accumulate, and in some sections of the rope there may be accumulations of changes in the length of the stroke. This phenomenon is shown in Fig. 3. This applies to practically all double lay rope designs operating in a pulley system. This mechanism influences the changes in the angle of inclination of the wires in the strands and also introduces additional variable tangential stresses, which accelerate the fatigue wear process.

The main disadvantage of the pulley system are large dimensions and masses of components, depending mainly on the diameter of the ropes used. The design of the ropes has a great impact on the service life of the entire rope system [11].

Publisher: **KOMAG Institute of Mining Technology, Poland**

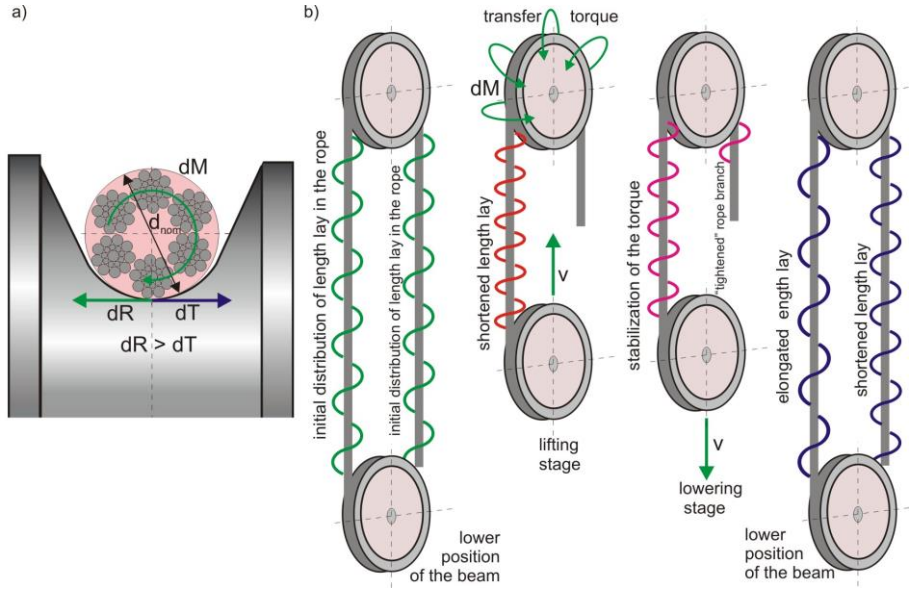

Fig. 3. Phenomenon of differentiation in stroke length of ropes operating in pulley systems:
a) friction forces and torque of the turn-off moment,
b) variation in rope stroke length during lifting and lowering [5]

Therefore, the cyclic change in the stroke length has a significant impact on the local fatigue damage. The change in the stroke length in a given branch is dynamic and results from the operating range of the pulley system. This leads to local damage on the sections where the stroke length changes most [12].

As in excavators' lowering systems, ropes with a steel core coiled in the opposite direction to that of the rope are most often used, this may lead to the formation of a large torque in the layers inside the rope. This moment is cyclical. In the phase of lowering the cutting wheel, the stroke lengths of the outer strands are lengthened and the stroke lengths of the core strands are shortened. In the lifting phase, the phenomenon is opposite. This creates a fatigue machine which, in the event of high friction between the core and outer strands, can lead to twisting of the inner rope layers. Unfortunately, this happens in such a way that it is invisible to an outside observer. Such phenomena were observed multiple times and always when the inner part of the rope was practically destroyed due to fatigue. Fig. 4 shows such an extreme situation.

Fig. 4. Degradation of the metal core of the lifting rope of the SchRs excavator lifting system as a result of the torque (photo A. Tytko)

Publisher: **KOMAG Institute of Mining Technology, Poland**

The figure shows a metal-core rope removed from the excavator, in which the steel core has practically been ground. The only effect visible on the outside was a change in the diameter of the rope over a short distance, and the two outer strands collapsed. As the rope was well covered with grease, the damage was hardly visible. The effect of all these wear factors is the reduction of the rope diameter. In Polish conditions, for ropes in opencast mining, a decrease in the rope diameter by 7% in relation to the nominal diameter disqualifies the rope for further operation. This moment is very difficult to observe. Moreover, this degradation occurs on a very short, difficult-to-find section of a rope that is several hundred meters long. The wear mentioned above occurs on the sections of the rope that are most often bent, therefore the information about the number of bends that the rope (or, in fact, its sections) makes during one work cycle is crucial for the correct diagnosis of these devices. Rope reliability and reducing the likelihood of its sudden failure in operation are important issues in rope inspection and testing [13].

Rope may also be damaged as a result of improper design or operation of rope pulleys. This applies in particular to the geometry of the grooves of each rope pulley, seizure of the bearings and the wrong angles of the rope slope on each pulley. The correct geometry of the pulley system structure and diagnostics of the rope condition during its operation always lead to the extension of the rope operation time, and thus the operation time of the entire device.

2.2. Rope operation cycle in a multi-pulley system of bucket-wheel excavators

In the case of opencast mining machines, the pulley systems are the key mechanical unit determining the quality and safety of their work. The operation of ropes in these systems is cyclical, but in each case it is determined by the design of a given pulley system. Parameters characterizing a given pulley system include: the number of pulleys of the movable and stationary pulleys, the distance of the rope section between the drum and the first pulley, and the rope distance between the last pulley (so-called dead pulley) and the rope attachment. However, the basic parameter determining which sections of the rope are most loaded are the distances by which each rope branch moves. Depending on the lifting and lowering height of the multi-pulley system (for each configuration of the system), a characteristic course can be determined during one cycle. This is the number of bends that each section of the rope experiences during the full work cycle to the height of lifting and lowering the cutting wheel. The work is the result of geological conditions in which a given machine works. Characteristics of the number of bends as a function of rope length is a basic indicator that can be used to indicate places on the rope that are potentially subject to wear. Opencast mining machines used in Poland have very large dimensions, and access to each rope section is difficult. Therefore, for a given machine, with a specific design of a multi-pulley system, operating in a specific work regime, access to particularly sensitive places is difficult. Main disadvantage of the pulley system are large dimensions and masses of components, depending mainly on diameter of the ropes used. Design of ropes has a great impact on service life of the entire rope system [14]. Nevertheless, the characteristic function of rope wear (number of bends as a variable of the rope length) makes it possible to set the pulley system in such a way that a foreman or another person assessing the condition of the rope during its operation could be in the immediate vicinity of the given rope.

2.3. Modelling the operation of steel ropes used in multi-pulley systems

It is possible to determine the number of bends affecting the hoisting ropes as a function of their length using a model describing the geometry and configuration of a given lifting rope. This model assigns to each rope section a number of bends during the complete cycle of lifting and lowering the cutting wheel. This modelling is based on the assumption that each bend made by the rope on a specific pulley adds up to the successive bends that this section of the rope makes during the entire work. Based on the tests of ropes in operation, it has been proven a number of times that the maximum wear of steel ropes operating in multi-pulley systems is concentrated in several characteristic places. These are: the sections of the rope that made the greatest accumulation of the number of bends, the sections of the rope lying on the pulleys and subjected to loads due to small rope displacements in the form of fretting oscillations, and the ends of ropes. This applies to both the rope attachment in

Publisher: **KOMAG Institute of Mining Technology, Poland**

the so-called dead end and on the drum. Therefore, in the opinion of the authors of this paper, rope condition assessment should focus on those places where the potential wear may be greatest. Therefore, a special algorithm (model) was developed that allows for the given geometry of the pulley system and specific, but real, conditions of its operation to calculate the actual numbers of bends performed by each part (sections) of the rope.

3. Results - calculator of the number of bends of steel ropes working in multi-pulley systems

The program (algorithm [6]), the main screen of which is shown in Fig. 5, is the calculator of the number of bends of steel ropes operating in multi-pulley systems.

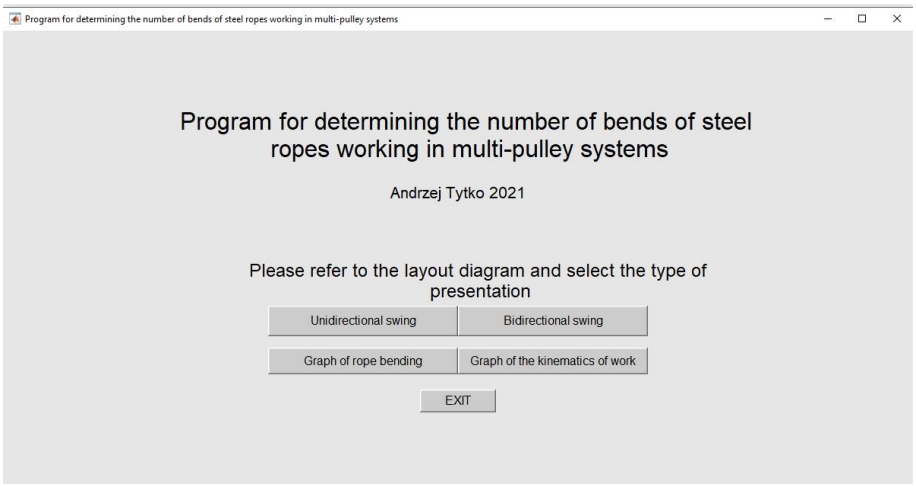

Fig. 5. Screen of the program for determining the number of bends in multi-pulley systems [6]

It enables modelling the real kinematic diagram of the working ropes by taking into account the number of pulleys of stationary and movable pulleys, the length between these pulleys in the lifting and lowering cycle. This is possible due to the active program screen shown in Fig. 6.

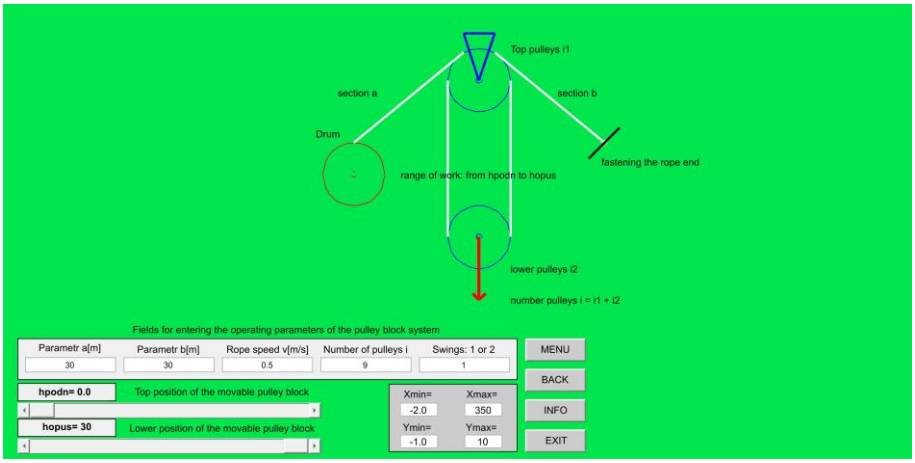

Fig. 6. Active program screen for entering geometrical parameters of the multi-pulley system as well as lifting and lowering heights of the multi-pulley system [6]

The program takes into account the lengths of rope sections between the drum and the first pulley, and the last pulley, and the rope fixation. The calculator draws a graph of the number of bends affecting each rope section during the work cycle. The cycle includes an optionally adjustable top and bottom position of the pulley system. The input data are the number of pulleys and the length of each

section of the rope, as well as the method of bending the rope on the pulleys: unidirectional or bidirectional. Changing each of the parameters results in generating a different diagram of bends. An example of such a diagram is shown in Fig. 7 for the parameters of the pulley system in Fig. 6.

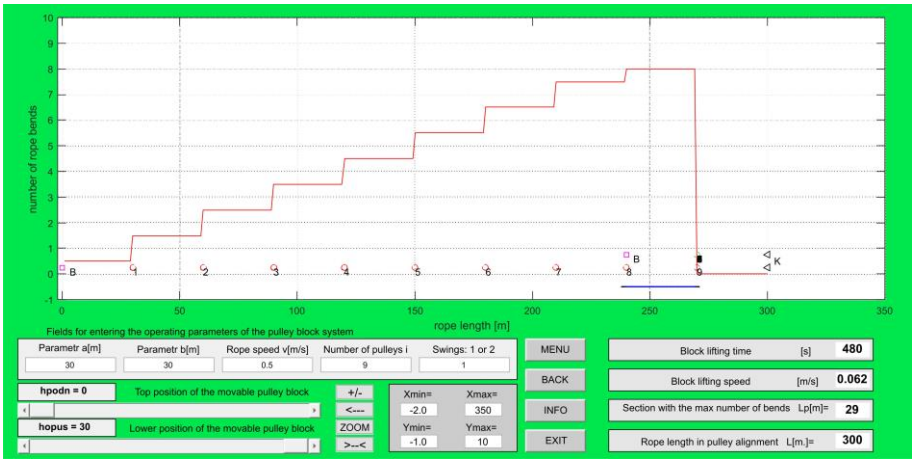

Fig. 7. An example of a diagram for the number of bends of a rope operating in a pulley system for the parameters of the system shown in Fig. 6

The calculator is a helpful tool used to determine the places of potential damage and the length of sections with a given number of bends. This tool, enables determining the places with the greatest number of damages.

On the basis of the analysis and model calculations made with the use of a calculator, it is possible to determine the sections of ropes potentially the most exposed to wear and deformations in the any pulley system. The section of the rope exposed in Fig. 7 is located near the entrance to the rope drum at the maximum lowering of the cutting drum. The drawing shows the results of the rope bends on the sheaves for individual sections of the rope during the lifting cycle of the cutting wheel boom from the position of 0 m to the position of +30 m. The presented example, for which simulations were made for various boom lifting heights, are not presented in this work, prove that the maximum level of wear, sections where damage may occur after a certain number of cycles (determined rope durability) of a rope with a length of approx. 300 m occur between pulleys 8 and 9 when the boom is raised to the level of +30 m. For the rope, it is a section of approx. 220-280 m from the fifth sheave on the side of the dead end of the rope.

The calculator is a helpful tool to indicate the places of potential fatigue damage, e.g. in the form of wire breaks.

4. Conclusions

The user of the calculator can model operation of the rope in any range of movement, both up and down. The calculator determines the rope sections with potentially greatest number of bends and shows the position of the sections, when the cutting system is in the highest or lowest position. Using the calculator's indications, the person who assesses the condition of the hoisting rope may adjust the position of the cutting wheel, so that the interesting section of the rope is within the range of observation. Opencast mining machines, as mentioned earlier, have very large dimensions and this tool allows to selecting the position of the boom in such a way that when lifting or lowering the wheel in front of the inspecting person, the rope with the potentially most worn part is wound. In the rope diagnostic practice of opencast mining machines such as multi-bucket or single-bucket dragline type, there is no similar diagnostic tool. The tool is not complicated, but it makes it possible to pinpoint potentially troublesome sections along the length of the rope. The rope examiner can focus on assessing these safety-critical several metres, rather than the entire length of the rope. This is the purpose and idea for the creation of the discussed tool. It was developed as a graphical interface in MATLAB [6], but it is possible to transfer the code to any other application and run it on any type of laptop or personal computer. The use of such a calculator should extend the working time of ropes

Publisher: **KOMAG Institute of Mining Technology, Poland**

operating in the luffing systems of opencast machines, due to identification of places on the ropes with the highest wear and on planning, through regular checks, convenient dates of tests, repairs and possible replacement of the ropes with new ones.

References

[1] https://stat.gov.pl/obszary-tematyczne/srodowisko-energia/energia/zuzycie-paliw-i-nosnikow-energii-w-2020-roku,6,15.html

[2] Tajduś, A., Kaczorowski, J., Kasztelewicz, Z., Czaja, P., Cała, M., Bryja, Z., Żuk, S. Węgiel brunatny – oferta dla polskiej energetyki. Możliwość rozwoju działalności górnictwa węgla brunatnego w Polsce do 2050 roku. Kraków: Komitet Górnictwa PAN, 2018

[3] Kasztelewicz Z.: Koparki wielonaczyniowe i zwałowarki. Technologia pracy, Fundacja Nauka i Tradycje Górnicze AGH, Kraków 2012

[4] Olszyna G., Tytko A.: Rola badań lin w procesie bezpiecznej eksploatacji kolei linowych, Przegląd Komunikacyjny, nr 3, str. 15–22, 2017

[5] Tytko A.; Liny stalowe, Budowa, własności, zastosowanie, eksploatacja, PWN, Warszawa, 2021

[6] Tytko A.: Program do wyznaczania liczby przegięć liny stalowej w układach wielokrążkowych. Kod programu MATLAB (unpublished)

[7] Frick W.: Loss of breaking load of high-strength wires during transverse pressure, [In:] M.A.R. Dohm (ed.), Exploring Opportunities – Synthetic/Steel: Proceedings of the OIPEEC Conference, Meylan, s. 247–265, 2019

[8] Gašić V., Olszyna G., Tytko A.: Some aspects on quantification of the wear at steel wire ropes. Proceedings of the Institution of Mechanical Engineers. Part J, Journal of Engineering Tribology; vol. 236 iss. 10, s. 2032–2041, 2022

[9] Gasić V., Olszyna G., Tytko A.: Methods for quantification of the abrasive wear at steel ropes used in drum devices, [w:] Vencl A. (ed.), BALKANTRIB '20: 10th international conference on Tribology: May 20–22, 2021, Belgrade, Serbia: proceedings, University of Belgrade, Belgrade, Serbian Tribology Society, Kragujevac, pp. 125–126

[10] Chaplin C.R.: Hoisting ropes for drume winders - the mechanics of degradation, Mining technology, July-August, 1994

[11] Heredia C.L.F., Olszyna G., Tytko A.: Effect of wire material properties on wire rope use. Journal of Machine Construction and Maintenance – Problemy Eksploatacji, 2018, No. 4, pp. 57–65

[12] Olszyna G., Tytko A., Sioma A.: Assessment of the condition of hoisting ropes by measuring their geometric parameters in a three-dimensional image of their surface. Archives of MiningSciences, Archiwum Górnictwa, 2013, vol. 58, No. 3

[13] Mouradi H., El Barkany A., El Biyaali A.: Steel wire ropes failure analysis: Experimental study, Engineering Failure Analysis 91 pp. 234-242, 2018

[14] Kowalski J., Tytko A.: Czynniki determinujące trwałość lin stalowych pracujących w układach wielokrążkowych. Dozór Techniczny nr 4, s. 77-81, 2006

Publisher: **KOMAG Institute of Mining Technology, Poland**

https://doi.org/10.32056/KOMAG2022.4.6

Use of pumping units equipped with oscillating hydraulic pressure intensifiers for displacement of cylinders with heavy loads over the entire stroke

Received: 04.11.2022

Accepted: 01.12.2022

Published online: 30.12.2022

Author's affiliations and addresses:

[1] National Institute of Research & Development for Optoelectronics / INOE 2000-subsidiary Hydraulics and Pneumatics Research Institute –IHP Bucharest, Romania

*** Correspondence:**

e-mail: popescu.ihp@fluidas.ro

Teodor-Costinel POPESCU [1*], Alexandru-Polifron CHIRIȚĂ [1], Ana-Maria Carla POPESCU [1], Alina-Iolanda POPESCU [1]

Abstract:

Working and moving in confined, limited and narrow spaces, specific to underground mining activities, also requires the use of hydraulically operated equipment, capable of developing large forces, with small dimensions. An example of such equipment includes pumping units comprising low-pressure electric pumps and oscillating hydraulic pressure intensifiers. They use low pressure in the primary side of the intensifier and generate high pressure in the secondary side of the intensifier. Such pumping units are usually used to achieve and maintain high pressure, either in the volumes of closed spaces (in strength tests on pipes and tanks) or at the end of the active stroke of hydraulic cylinders (in hydraulic presses). On an experimental laboratory bench, which comprises a test cylinder, powered by a pumping unit, equipped with an oscillating hydraulic pressure intensifier, and a load cylinder, powered by another pumping unit, with the possibility of load control, the authors show that: the application range of these pumping units can be extended in the third direction, too, useful for underground mining activities, namely for drive of hydraulic cylinders with low gauge / displacement speeds and constant high load (high working pressure) over the entire working stroke length; the uniformity of displacement of these cylinders, with load throughout the stroke length, which are powered and driven with such pumping units, is slightly affected by the pulsating mode of operation of the hydraulic pressure intensifier. A set of experimental measurement results is presented for a constant value of the load over the entire displacement stroke of the test cylinder.

Keywords: low-pressure pumping unit, oscillating hydraulic pressure intensifier, high pressure, hydraulic cylinder

1. Introduction

The operating regime of hydraulic drive systems includes certain work phases in which the actuated displacement engines, hydraulic cylinders and rotary hydraulic engines have to develop large static or dynamic forces and torques, and consequently have to be powered at high pressure rates.

These high pressure rates, of the order of hundreds or thousands of bars, can be generated by two types of pumping units:

a) ***pumping units*** comprising ***displacement pumps and high-pressure hydraulic equipment***; they directly supply linear or rotary displacement hydraulic engines;

b) ***pumping units*** comprising ***displacement pumps and low-pressure hydraulic equipment***; they supply pressurized closed volumes or displacement hydraulic engines by means of ***hydraulic pressure intensifiers***, which are placed between the pumping unit and the hydraulic consumers.

The first category of pumping units is more expensive and, as a rule, is suitable in dynamic applications, where linear or rotary movement of large loads with uniform speed rates is required. This category is not energy efficient for static applications, where the aim is to produce and maintain high pressure for a long time in a closed enclosure, or for dynamic applications that, for example, require high pressure rates only over a short segment of the hydraulic cylinder advance stroke, and the rest of the stroke, as well as the entire retreat stroke, must be done at high speed rates and low pressure.

The pumping units under the second category make the energy-dissipating applications of the first category more energy efficient, but they have the disadvantages of low and pulsating flow rates for high-load dynamic applications. They are developed in a wide range of construction variants, intended to offer an optimal solution, with reduced pulsations and increased flow rates for dynamic applications of short duration.

Hydraulic pressure intensifiers with oscillating pistons are known in the specialized literature under several names: *oscillating hydraulic pressure amplifiers (intensifiers)* [1,2,3], *oscillating pumping units, boosters, miniboosters* [4,5,6].

There is a diverse range of construction solutions for miniboosters, single or double acting in relation to high-pressure pumping, designed to boost the pressure of low-pressure pumping units. They have been tested experimentally [7,8,9], investigated by mathematical modeling / numerical simulations [10,11,12,13] and used in various applications of hydraulic drive systems [14,15,16,17]. They can power, for example, single-acting or double-acting hydraulic cylinders that move large loads linearly at the end of the advance stroke, or achieve and maintain high pressure in a closed enclosure. They are mounted between the pumping unit and the actuated cylinder (Fig. 1), as close to the latter as possible, and comprise: an oscillator (**OP**), consisting of two oscillating pistons of different diameters and a 3/2 bistable directional control valve; two check valves (**KV1**, **KV2**); a pilot-operated check valve (**DV**), bypassing the oscillator. The low-pressure connecting fittings **IN** (inlet) and **R** (return), in the primary side of the minibooster, are connected to consumers of the hydraulic directional control valve of the pumping unit, and the high-pressure connecting fitting **H**, in the secondary side of the minibooster, is connected to the piston chamber of the actuated cylinder.

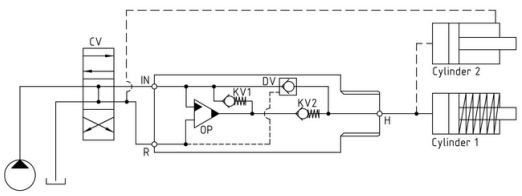

Fig. 1. Simplified hydraulic diagram of a minibooster

State of the art in technical applications related to the use of low-pressure pumping units, equipped with oscillating hydraulic pressure intensifiers (miniboosters), does not include applications involving displacements of hydraulic cylinders that have high loads over the entire working stroke length. ***The objective*** of this paper is to experimentally demonstrate the possibility of using miniboosters in such applications, too, with reasonable limits of the displacement uniformity and continuity of the actuated cylinders, under the conditions of the pulsating operation mode of these pressure intensifiers [18, 19, 20].

Publisher: **KOMAG Institute of Mining Technology, Poland**

2. Materials and Methods

To achieve the intended objective, the authors have used an experimental method by which they have monitored the dynamic behaviour of a hydraulic cylinder, which, being fed into the piston chamber through a minibooster, moves with a constant load, equivalent to the pressure of $700x10^5$ *Pa*, over the entire stroke length. The minibooster has been integrated into a low-pressure pumping unit, while the hydraulic cylinder under testing – into a test bench.

2.1. Low-pressure pumping unit equipped with minibooster

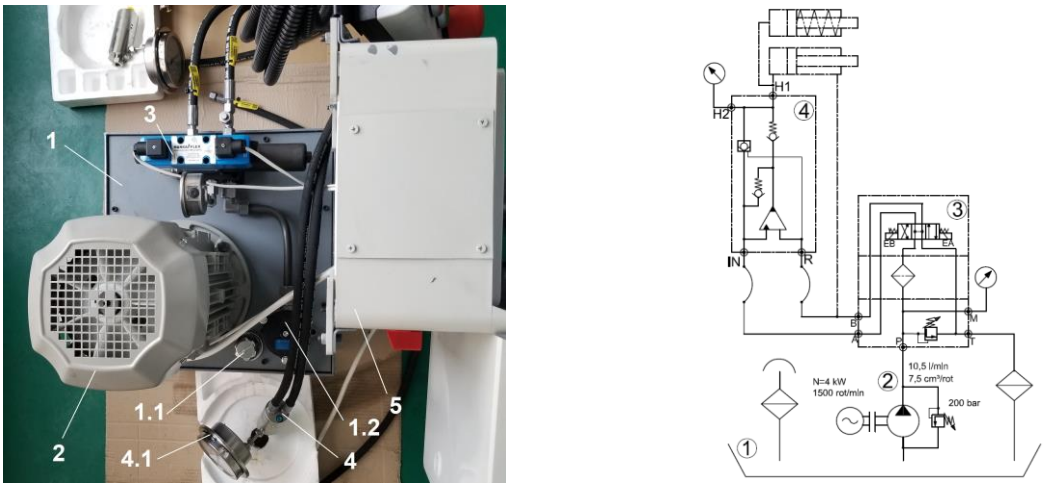

Fig. 2. Pumping unit equipped with minibooster (left side – general view; right side - hydraulic diagram)

The pumping unit in Fig. 2 comprises: **1**= oil tank ($38x10^{-3}$ m^3 volume); **1.1**= fill and vent filter; **1.2**= return filter; **2**= low-pressure electric pump (*4 kW*; *1500 rev/min*; $7{,}5x10^{-6}$ m^3/rev; $250x10^5$ *Pa*); **3**= block with hydraulic devices (pressure control valve; pressure filter; 4/3 hydraulic directional control valve, DN6, electrically actuated; $250x10^5$*Pa* pressure gauge); **4**= HC7 minibooster (*5:1* amplification ratio; $0...200x10^5$ *Pa* pressure in the primary side; $0...1000x10^5$ *Pa* pressure in the secondary side; $14x1{,}667x10^{-5}$ m^3/s low-pressure inlet maximum flow rate; $1{,}6x1{,}667x10^{-5}m^3/s$ amplified pressure outlet maximum flow rate); **4.1**= $2500\ x10^5$ *Pa* pressure gauge; **5**= electric panel.

Pressure adjustment in the circuit **H1**, which supplies the hydraulic cylinder actuated by the pumping unit, is done using the pressure control valve on the hydraulic block of the unit, and the adjusted value of this pressure can be read on the high-pressure gauge, mounted in the high-pressure connecting fitting **H2.**

2.2. Test bench for low-pressure pumping unit equipped with minibooster

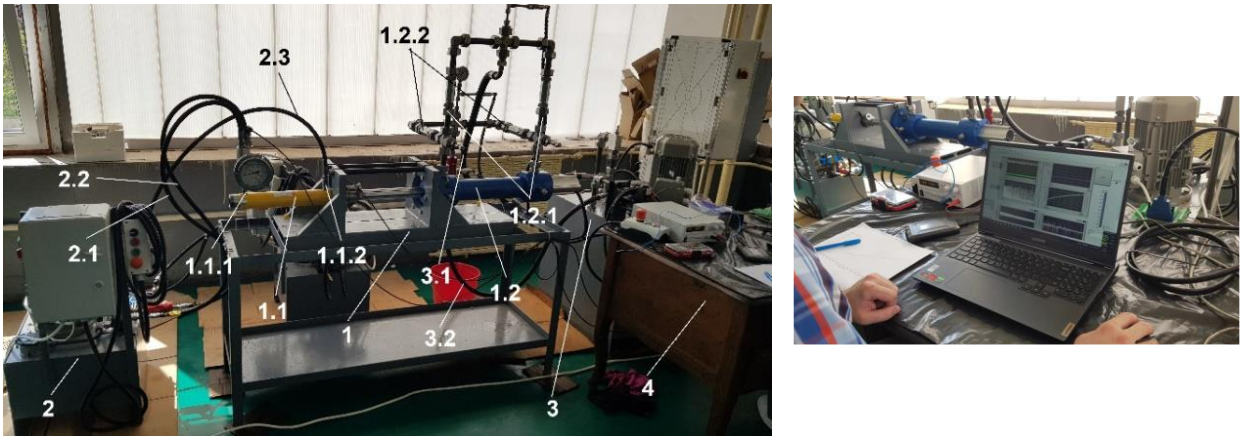

Fig. 3. Test bench for pumping unit equipped with minibooster

The structure of the test bench and the pumping unit in Fig. 3 is as follows:

1: Module for clamping the hydraulic cylinders; **1.1**= test cylinder with piston Ø= *38,1x 10^{-3} m*, rod Ø= *25x10^{-3} m*, stroke length= *257x10^{-3} m*, p_{max}= *700x10^{5} Pa*; **1.1.1**= fitting that connects cylinder piston chamber with secondary side of the minibooster; **1.1.2**= connecting fitting and hose for cylinder rod chamber; **1.2**= load cylinder with built-in stroke transducer and: piston Ø= *80x10^{-3}m*, rod Ø= *45x10^{-3} m*, stroke length= *300x10^{-3} m*, p_{max}= *300x10^{5} Pa*; **1.2.1**= cylinder chambers inlet check valves; **1.2.2**= cylinder chambers outlet check valves;

2: Low-pressure pumping unit (previously presented); **2.1, 2.2**= hoses connecting the primary side of the minibooster to the consumers of the hydraulic directional control valve of the unit;

3: Pumping station for filling the load cylinder equipped with: electric pump of *2 kW*, *10x10^{5}Pa*, *90x1,667x10^{-5} m^{3}/s* ; oil tank with V= *180x10^{-3} m^{3}*; filling pressure control valve; proportional pressure control valve (acting as load); fill and vent filter; return filter; **3.1**= cylinder chambers fill fitting and hose; **3.2**= cylinder chambers drain fitting and hose;

4: Control and data acquisition module (Fig. 3 - right side) acquiring data from the transducers of: acceleration, measured in the direction of displacement of the minibooster pistons (**Acc1**); acceleration, measured in the direction of displacement of the hydraulic cylinders on the test bench (**Acc2**); minibooster primary side pump pressure (**p1**); load cylinder pressure (**p2**); filling pump pressure (**p3**); minibooster primary side input flow rate (**Q1**); load cylinder flow rate (**Q2**); **stroke** (built into the load cylinder).

2.3. Test conditions for the pumping unit equipped with a minibooster

In the following Item the results of the experimental tests for a constant value of the test cylinder load, namely ***700x10^{5} Pa***, equivalent to the resisting force of ***80x10^{3} N***, which has been maintained throughout the advance stroke, are presented. The load value of the test cylinder has been adjusted using the proportional valve on the pumping station for filling the load cylinder.

The experimental tests have been carried out under the following conditions: on the test bench shown in Fig. 3, opening pressure of the normally closed valve with which the low-pressure pumping unit is provided, has been adjusted to ***160x10^{5} Pa*** (equivalent to max. ***800x10^{5} Pa*** in the secondary side of the intensifier); pressure to open the safety valve of the load cylinder filling pump has been adjusted to ***19x10^{5} Pa***; the tests have been carried out only during the advance stroke of the test cylinder; data acquisition has been done with a sampling frequency of ***200 samples/s*** and duration of ***20 s***, exploring a number of ***4000 samples*** for a segment of ***169,6x10^{-3} m*** from the total stroke (***257x10^{-3} m***) of the test cylinder.

3. Results

Testing the pumping unit equipped with a minibooster, presented in Item 2.1., has aimed at determining the influence of the pulsating operation mode of this type oscillating pressure intensifier on the displacement continuity and uniformity of the test cylinder which is a part of the test bench, under the conditions in which it is "loaded" with the load equivalent to the working pressure of *700x10^{5} Pa*.

To capture the physical phenomena that occur when the intensifier is fed with the full flow rate of the pump, when it bypasses the intensifier through the pilot-operated check valve DV (Fig. 1), first the data acquisition has been started, then the pumping unit. On the graph in Fig. 7, which shows the time-variation of the flow rate of the pumping unit, it can be seen that, for less than a second, the pump flow bypasses the intensifier and the average flow rate Q1 decreases from *9x1,667x10^{-5} m^{3}/s* to *7x1,667x10^{-5} m^{3}/s*.

The data from eight transducers mounted on the test bench have been acquired, and the results of their graphical processing are presented further on.

3.1. Graphical processing of data acquired with the acceleration transducers

The first factor disturbing the displacement continuity and uniformity of the test cylinder includes ***mobile parts*** of the minibooster, which have a symmetrical alternating displacement with small amplitudes (vibrations) and variable frequency rates in the range 0...20 Hz, namely: the assembly of the two (low and high pressure) pistons; the 3/2 bistable directional control valve, with bistable position and hydraulic control; the check valves for the intake and exhaust of oil into / from the high-pressure piston chamber. The accelerations generated by the vibrating parts of the minibooster have been detected with the acceleration transducer **Acc1**, mounted on the minibooster housing (perpendicular to its longitudinal axis), and the accelerations generated by the displacement of the test cylinder rod have been detected with the acceleration transducer **Acc2**, mounted on the cylinder rod.

Fig. 4 shows the time-variations of the acceleration of the vibrating parts of the minibooster (top), and of acceleration of the test cylinder rod (bottom), when it operates at the working pressure of $700x10^5$ *Pa*, linearly displacing the load of $80x10^3$ *N*.

It is found that variation of acceleration of the vibrating parts of the minibooster has an average value of ± 60 *m/s*^{2}, and variation of acceleration of the hydraulic cylinder rod - an average value of ± 80 *m/s*^{2}. The negative influence of the vibrating parts of the minibooster on the displacement continuity of the cylinder rod is found in the ± 20 *m/s*^{2} increase of its vibration amplitude.

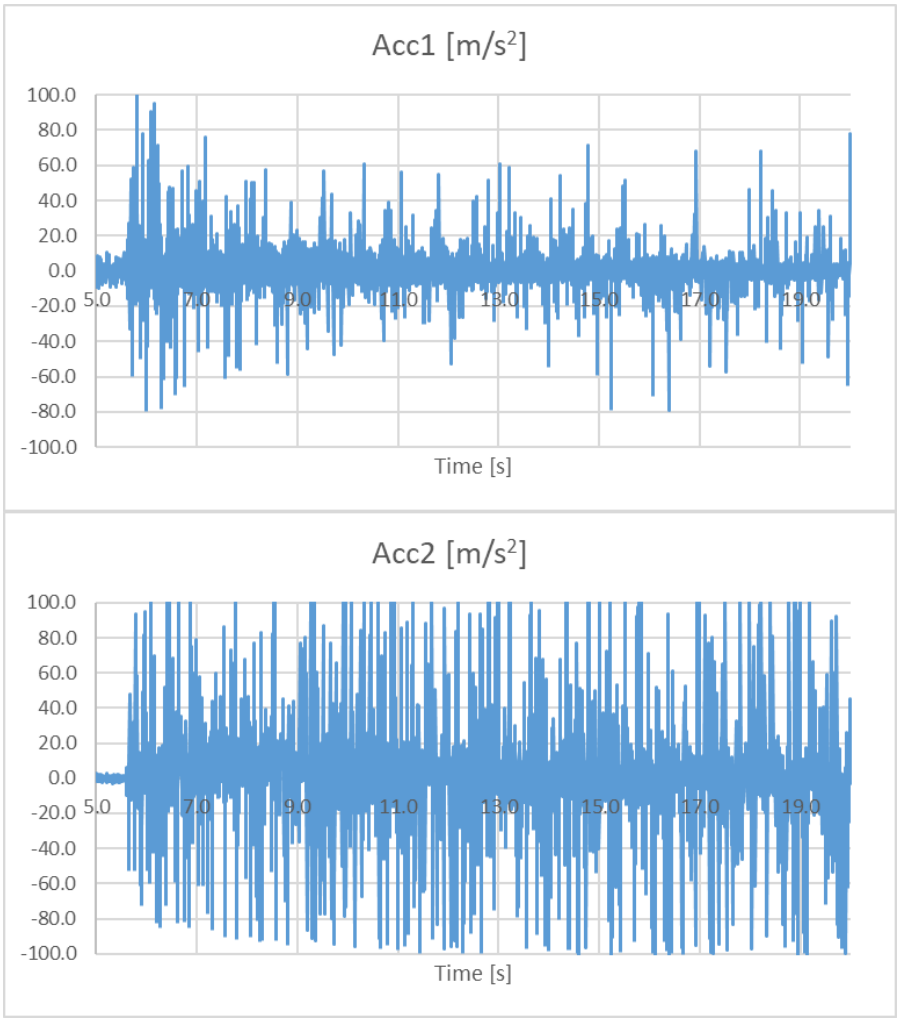

Fig. 4. Time-variation of acceleration measured with Acc1 (top) and Acc2 (bottom)

The accelerations measured with the two transducers have been processed using the power spectral density (PSD) function. The results, depicted graphically in Fig. 5, show the strength of the vibrational

energy variations as a function of frequency, variation measured in the direction of: displacement of the minibooster pistons, Fig. 5-top; displacement of the hydraulic cylinders, Fig. 5-bottom. At the maximum operating frequency of the minibooster, namely 20 Hz, it is found that the magnitude has the value of approx. 5, resulting from the Fourier transformation of the data acquired with the transducer **Acc1**, and the magnitude of approx. 40, resulting from the processing of the data acquired with the transducer **Acc2**, corresponds to the direction of displacement of the load cylinder.

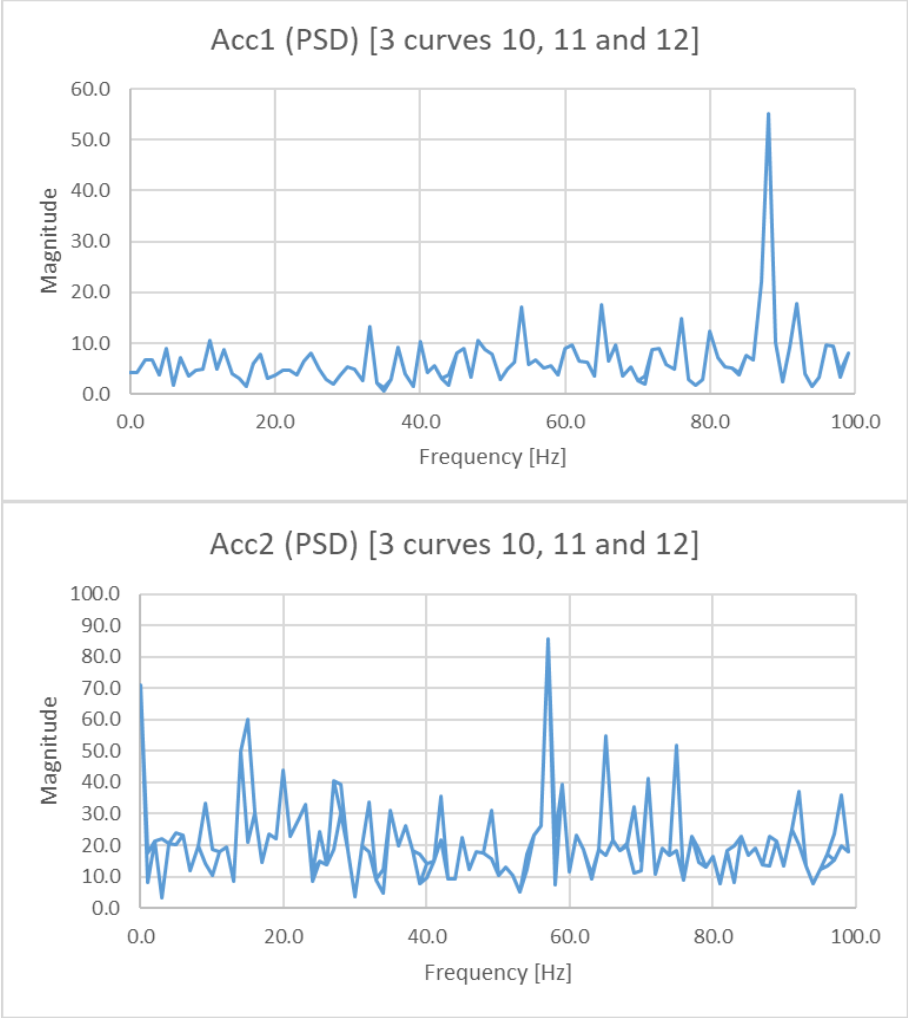

Fig. 5. Power spectral density determined with Acc1 (top) and Acc2 (bottom)

3.2. Graphical processing of data acquired with the pressure transducers

The second factor disturbing the displacement continuity and uniformity of the test cylinder is ***the time-variation of the pressure*** in the high-pressure piston chamber of the minibooster. It has a pulsating mode of operation, with symmetrical alternating cycles, of constant amplitude and variable frequency (*0...20 Hz*), for oil suction and discharge into/from its chamber.

Fig. 6 shows the time-variation of the pressure in: the primary side of the minibooster, measured with transducer **p1** (top); the load cylinder piston chamber (secondary side of the minibooster), measured with transducer **p2** (centre); the discharge circuit of the filling pump, measured with transducer **p3** (bottom). Pressure values measured with transducer **p2** are multiplied by **4.41**, which is the value of the ratio of the piston areas of the two (load and test) cylinders on the bench.

From the graphical representation, it can be seen that pressure variation in the primary side of the minibooster is around the average value of $150x10^5$ *Pa*, pressure variation in the load cylinder is around the average value of $700x10^5$ *Pa* (4,41x159), and pressure variation in the load cylinder filling

circuit is around the average value of $19x10^5$ *Pa*. ***It is found that the pressure pulsations of the minibooster are lower than those of the gear pump in the structure of the tested pumping unit.***

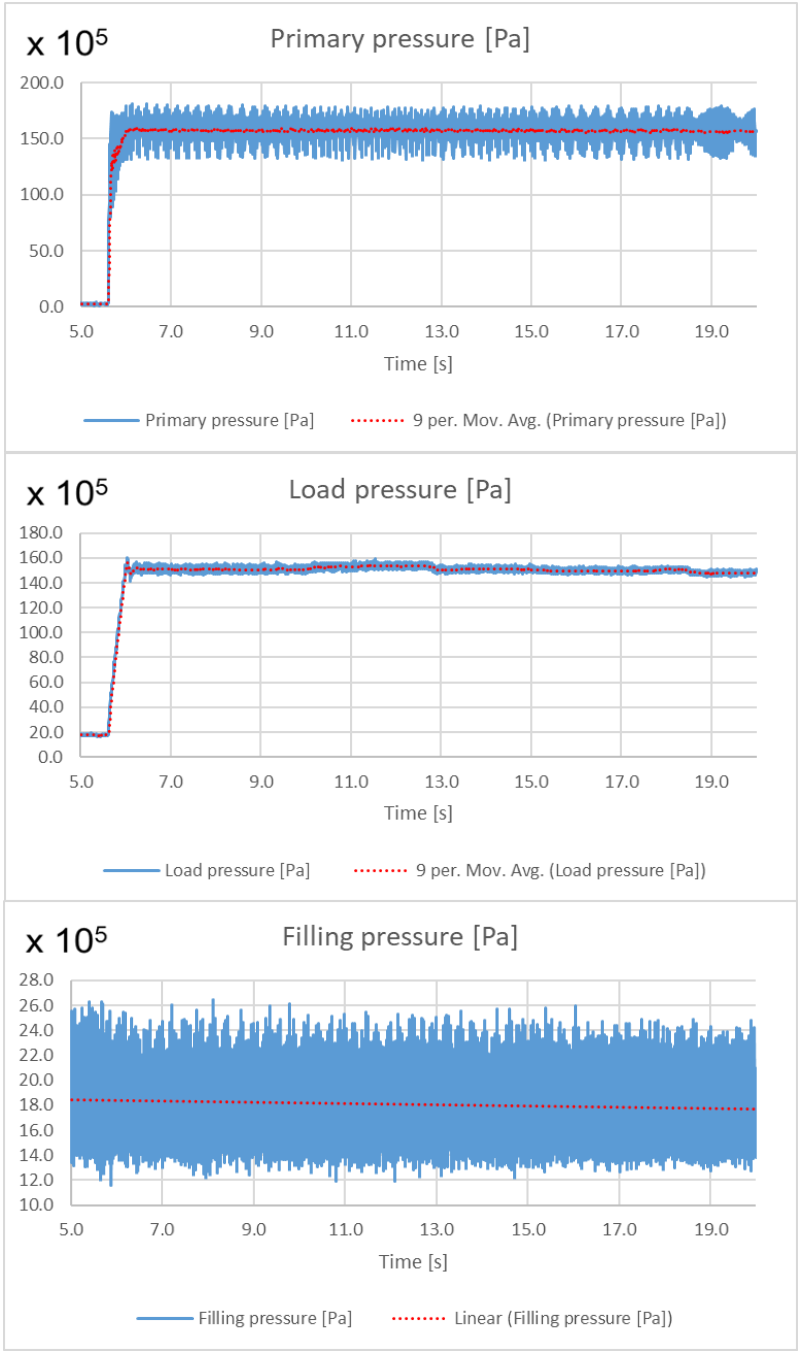

Fig. 6. Time-variation of pressure measured with p1 (top), p2 (centre) and p3 (bottom)

3.3. Graphical processing of data acquired with the flow transducers

The third factor disturbing the displacement continuity and uniformity of the test cylinder is ***the time-variation of the flow rate*** in the high-pressure piston chamber of the minibooster.

Fig. 7 shows the time-variation of the flow entering, at low pressure, the primary side of the minibooster, measured with the transducer **Q1** (top), and the variation of the flow rate in the piston chamber of the load cylinder, identical to the flow rate that comes out, at high pressure, from the secondary side of the minibooster, measured with the transducer **Q2** (bottom).

Variation of the flow rate in the primary side of the minibooster is around the average value of $7x1{,}667x10^{-5}$ m^3/s, and variation of the flow rate in the load cylinder is around the average value of $2{,}7x1{,}667x10^{-5}$ m^3/s.

During the displacement of the test cylinder under the $700x10^5$ Pa load ***it is found that variation of the flow rate coming out from the secondary side of the minibooster at high pressure is less than variation of flow rate entering the primary side of the minibooster at low pressure***.

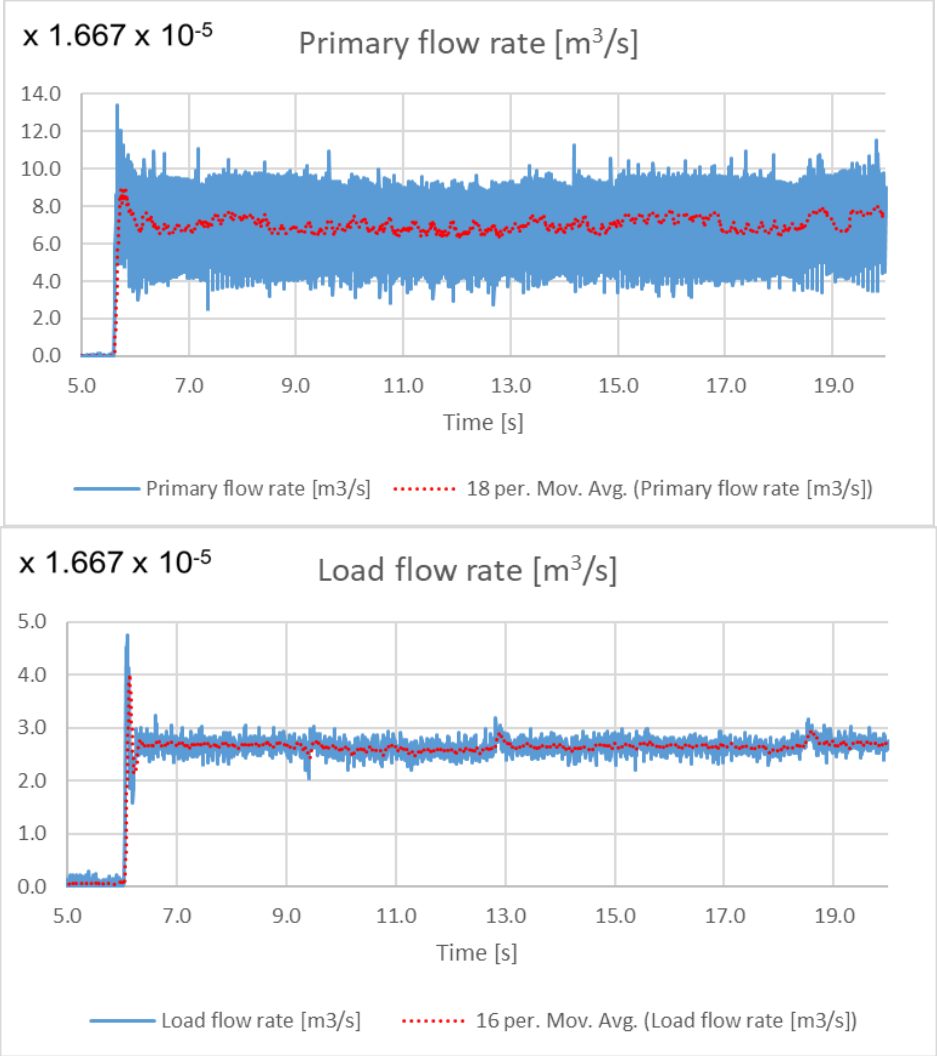

Fig. 7. Time-variation of flow rate measured with Q1 (top), and Q2 (bottom)

3.4. Graphical processing of data acquired with the displacement transducer

The cumulative effect of the three factors disturbing the displacement continuity and uniformity of the test cylinder results from the graphical processing of the data acquired with the displacement transducer. Fig. 8 shows the time-variation of the displacement of the test cylinder, and Fig. 9 – a representative detail of the deviations from the linearity of this displacement. It can be noticed that, over the entire stroke of displacement under load of the cylinder ($180x10^{-3}$ m), the maximum value of these deviations is approximately $1x10^{-3}$ m.

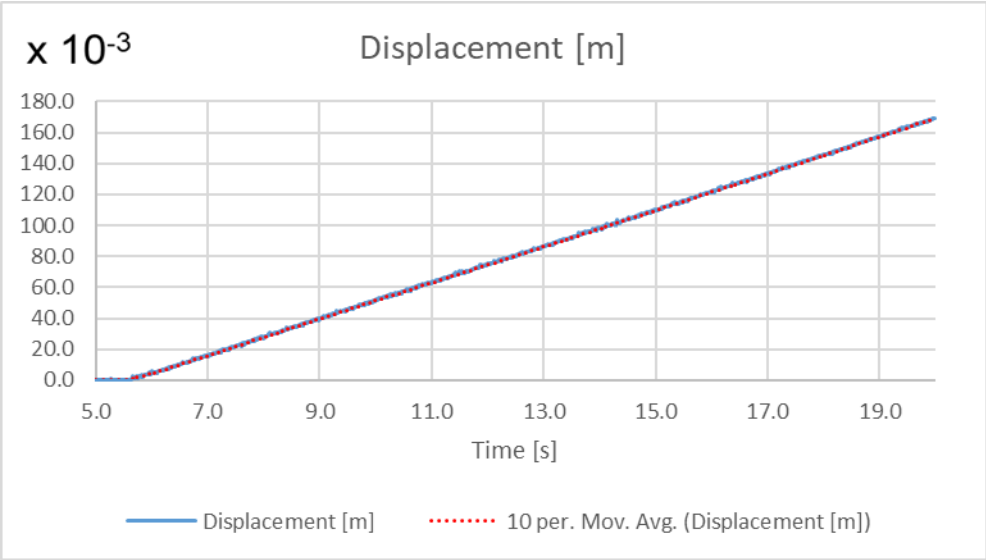

Fig. 8. Time-variation of the displacement of the test cylinder at 700 x 10^5 Pa load

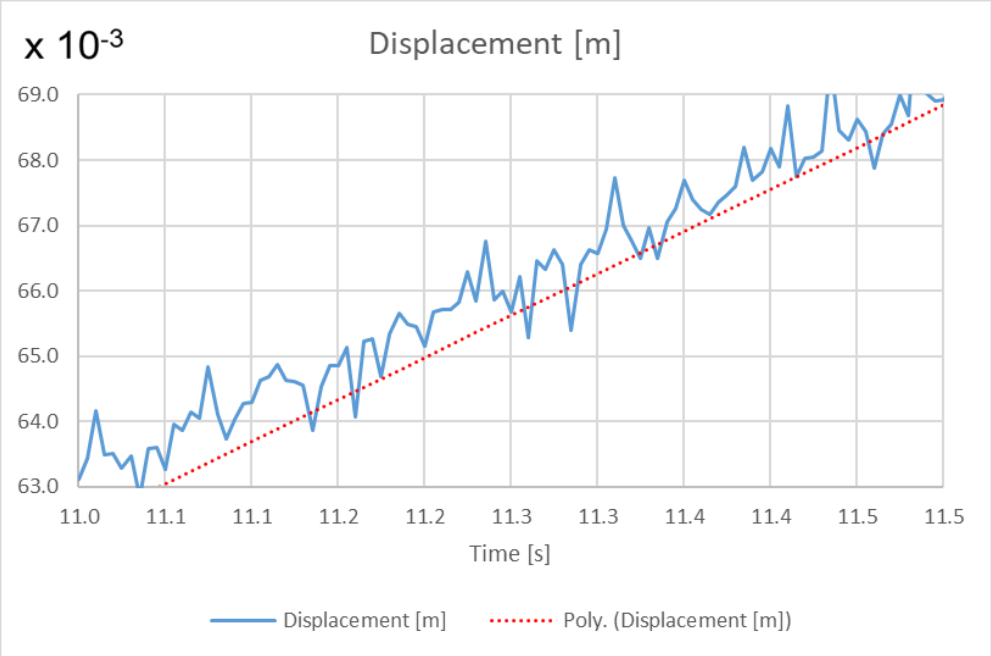

Fig. 9. Deviations from the linearity of the displacement of the test cylinder under load

4. Discussion

It is experimentally demonstrated that the compact and small size pumping units comprising low-pressure electric pump, oscillating hydraulic pressure intensifier, hydraulic directional control valve, pressure control valve and filters, can be used for safe displacement of hydraulic cylinders, with a constant load throughout the stroke, being suitable for activities in confined spaces (e.g., mining activities).

The pulsating mode of operation of the minibooster, caused by the alternating symmetrical displacement of its mobile parts, with the frequency of 0,01...20 Hz, as well as flow and pressure pulsations do not induce dangerous shocks that could affect the mechanical strength of the hydraulic cylinder and its drive system.

Publisher: **KOMAG Institute of Mining Technology, Poland**

Deviations from the linearity of the displacement are small, and the displacement speed at high loads increases if the normally closed valve of the pumping unit is adjusted to a higher opening pressure than that corresponding to the load.

The vibrating parts of the minibooster, which move linearly, bidirectionally, over short distances and with variable frequencies in the range of 0,01...20 Hz, are the main cause of deviations from the linearity of the displacement of the test cylinder under load.

Acknowledgments

The research work presented in this paper has been developed under the Financial Agreement No. 272/24.06.2020, signed by the Ministry of European Funds / Ministry of Education and Research and S.C. HESPER S.A. Bucharest for the Innovative Technological Project entitled "Digital mechatronic systems for generating pressure of 1000 bar, using hydraulic pressure intensifiers" (SMGP), project under implementation from 01.07.2020 to 30.06.2023. Financial support has also been granted under a project funded by the Ministry of Research, Innovation and Digitalization through Programme 1- Development of the national research & development system, Sub-programme 1.2 - Institutional performance - Projects financing the R&D&I excellence, Financial Agreement No. 18PFE/30.12.2021.

References

[1] Levinsen A.: Scanwill fliud power Unique hydraulic pressure intensifier solutions. https://www.luvra-hydraulik.de/fileadmin/web_data/downloads/Luvra-Hydraulik-Scanwill-0915.pdf [accessed: 29.08.2022]

[2] Gannon M.: How can hydraulic pressure intensifiers improve your system design? https://www.fluidpowerworld.com/can-hydraulic-pressure-intensifiers-improve-system-design [accessed: 29.08.2022]

[3] https://www.scanwill.com/files/documents/Scanwill-productsheet-en.pdf [accessed: 29.08.2022]

[4] Wang F., Gu L., Chen Y.: A hydraulic pressure-boost system based on high-speed On Off valves. IEEE/ASME Trans. Mechatronics 2013. 18(2), pp. 733-743. DOI: 10.1109/TMECH.2011.2182654

[5] Yang F., Tadano K., Li G., Kagawa T.: Analysis of the Energy Efficiency of a Pneumatic Booster Regulator with Energy Recovery. Applied Sciences 2017. 7(8), paper ID 816. DOI:10.3390/app7080816

[6] Nazarov F., Rakova E., Weber J., Vardini A. R.: A Novel Approach for Pneumatic Pressure Booster. In: Proceedings of 11th International Fluid Power Conference 11. IFK; 2018. vol. 3, pp. 222-235. DOI: 10.18154/RWTH-2018-224786

[7] Günaydın A.C., Halkacı M., Ateş F., Halkacı H.S.: Experimental Research of the Usability on Double Acting Intensifiers in Hydroforming. In: Proceedings of the MATEC Web of Conferences 220 ICMSC 2018. 04001.
https://www.matec-conferences.org/articles/matecconf/pdf/2018/79/matecconf_icmsc2018_04006.pdf [accesed:13.09.2021]

[8] Khandekar S., Dollinger N., Groll M.: Understanding operational regimes of closed loop pulsating heat pipes: an experimental study. Applied Thermal Engineering 2003. 23(6), pp. 707-719. DOI: 10.1016/S1359-4311(02)00237-5

[9] Fuqiang C., Rendong W., Chaolong Y., Wei W., Wei J.: Research on Velocity Fluctuation of High Pressure and High Flow Double Booster Cylinder Hydraulic System. Hindawi Mathematical Problems in Engineering 2020. Article ID 2648508, 12 pages. DOI: 10.1155/2020/2648508

[10] Zwier M. P., vanGerner H. J., Wits W. W.: Modelling and experimental investigation of a thermally driven self-oscillating pump. Applied Thermal Engineering 2017. 126, pp. 1126-1133. DOI: 10.1016/j.applthermaleng.2017.02.063

[11] Dobson R.T.: Theoretical and experimental modelling of an open oscillatory heat pipe including gravity. International Journal of Thermal Sciences 2004. 43(2), pp. 113-119. DOI: 10.1016/j.ijthermalsci.2003.05.003

[12] Zardin B., Cillo G., Zavadinka P., Hanusovsky J., Borghi M.: Design and modelling of a cartridge pressure

amplifier. In: Proceedings of the ASME/JSME/KSME Joint Fluids Engineering Conference; 2019. vol. 1, article no. UNSP V001T01A043. DOI: 10.1115/AJKFluids2019-5474

[13] Zardin B., Cillo G., Borghi M., Zavadinka P., Hanusovsky J.: Modelling and simulation of a cartridge pressure amplifier. In: Proceedings of the ASME-BATH Symposium on Fluid Power and Motion Control; 2018. Article no. V001T01A057

[14] Espersen C.: Pressure Boosters in Hydraulic Systems A Solution Which Is Often Overlooked. https://nanopdf.com/download/pressure-boosters-in-hydraulic-systems_pdf [accessed: 13.09.2021]

[15] Pioneer Machine Tools, Inc.: The increase pressure actuation system of hydraulic boosters HC series. http://www.pmt-pioneer.com/en/product-detail5.html [accessed: 13.09.2021]

[16] https://www.minibooster.com/hc7/ [accessed: 13.09.2021]

[17] Bartnicki A., Klimek A.: The research of hydraulic pressure intensifier for use in electric drive system. IEEE Access 2019. 7, pp. 20172-77. DOI 10.1109/ACCESS.2019.2897148

[18] Popescu T.-C., Chirita P.-Al., Popescu A. I.: Increasing energy efficiency and flow rate regularity in facilities, machinery and equipment provided with high operating pressure and low flow rate hydraulic systems. In: Proceedings of 18th International Multidisciplinary Scientific GeoConference SGEM; 2018. vol. 18, pp. 401-408. DOI: 10.5593/sgem2018/4.1

[19] Popescu T.C., Chiriță A.P., Popescu A.-M.C.: Research on the assessment of flow and pressure pulses in oscillating hydraulic intensifiers. Mining Machines 2020. (4), pp. 14-23. DOI: 10.32056/KOMAG2020.4.2

[20] Chiriță A.P., Popescu T.C., Popescu A.-M.C., Dincă R.-Ș., Marinescu A.D.: Research on the use of hydro-pneumatic accumulators in order to reduce the flow rate and pressure pulsations of oscillating hydraulic intensifiers. Mining Machines 2021. 39(4), pp. 37-46. DOI: 10.32056/KOMAG2021.4.4

Publisher: **KOMAG Institute of Mining Technology, Poland**

https://doi.org/10.32056/KOMAG2022.4.7

Influence of nonlinearities in sensor and actuator on the operation of the rotational speed control system of a roadheader cutting head

Received: 27.12.2022

Accepted: 29.12.2022

Published online: 30.12.2022

Author's affiliations and addresses:

[1] Silesian University of Technology, Faculty of Mining, Safety Engineering and Industrial Automation, Akademicka 2a, 44-100 Gliwice, Poland

*** Correspondence:**

e-mail: jaroslaw.joostberens@polsl.pl

Jarosław JOOSTBERENS [1*], Adam HEYDUK [1]

Abstract:

The paper presents a discussion on the selected nonlinearities existing in sensor and actuator subsystems of the roadheader cutting head speed control system. There have been concerned the most significant nonlinearities - rotational speed encoder and frequency rate limiter in the input of the power electronic converter. There has been presented a detailed analysis of the nonlinear input frequency rate limiter and the frequency-dependent input-output curves have been calculated. They enable qualitative and quantitative evaluation of system performance over a wide range of input signal frequencies and amplitudes. The measurement time of the encoder-based speed sensing should be as short as possible, or continuous measurement (like tachogenerator) should be used. The impact of encoder delay and inertia is much less significant than that of the frequency rate limiter. For better drive system performance, the frequency converter should be overmatched to ensure current overload capability – allowing an increase in the permissible rate of output voltage frequency change.

Keywords: roadheader, speed control system, rotational encoder, power electronic converter, rate limiter, describing function.

Publisher: **KOMAG Institute of Mining Technology, Poland**

1. Introduction

Roadheaders are large-power complex machines commonly used in underground mining and tunnelling [1]. Modern mining machines (including longwall shearers and roadheaders) are sophisticated mechatronic systems [2], in which the operation of the electronic control system has a significant impact on their performance and achieved production results. Thus, it is advisable to search for methods of optimizing their operation taking into account both mathematical models [3] and the results of their empirical tests [4]. The main research and development directions include arm position control [5], cutting head geometry optimization [6], sensor fusion [7], load condition identification [8,9] and the application of machine vision systems [10,11]. Methods based on artificial intelligence (neural networks) are often used [12,13]. The problem described in this paper emerged during the implementation of a research project of an innovative R-130 roadheader (manufactured by FAMUR S.A.) with an inverter-fed drive of the cutting head. As the rock cutting process is a complex combination of many stochastic (resulting from the fracture of brittle, stratified material) and deterministic factors (specified by the arrangement of the picks on the cutting head surface), the evaluation of this process, in order to determine the optimum value of rotational speed minimizing the power consumption of the process and limiting the frequency of significant dynamic overloads, can only be performed over longer periods of time (corresponding, for example, to one cutting head rotation time). This process is illustrated in Fig. 1.

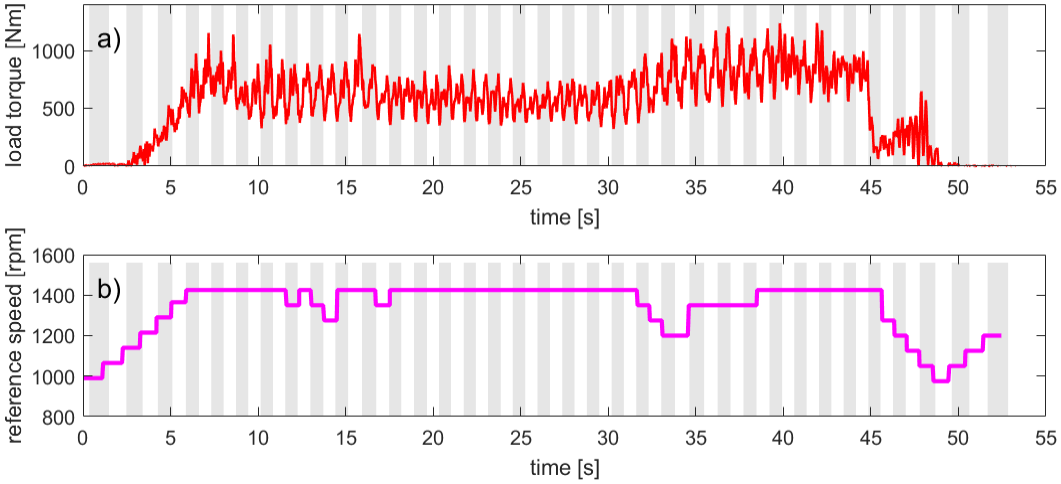

Fig. 1. An example of reference speed generator operation recorded at the laboratory stand: a) recorded load torque, b) generated reference speed

The task of the speed control system is then to track these setpoint changes established by the higher-level system. The speed controller should provide close tracking the reference signal with no static error, no oscillations and no overshoot. These oscillations and overshoots could cause significant overload or even damage to the mechanical part of the drive. For these reasons we have chosen a simple proportional-integral (PI) controller. A derivative part was omitted because of noise in the input signal. Optimum values of the proportional K_p and integral K_i gains of the controller for the laboratory stand have been selected on the basis of the simulation of the linearized model of the controlled system (inverter-fed induction motor and the mechanical inertia). Model linearization – around the rated operating point – significantly increased the simulation speed, still capturing the most important dynamical features of the original system. Detailed process of controller gain calculation has been presented in [14].

2. Materials and Methods

The squirrel-cage induction motor is, in general, a non-linear element considered over the entire speed range (from start-up to synchronous speed), but in the range of small slips (around the rated slip) corresponding to normal operating conditions under load, it is possible to linearize the mathematical model of this motor by taking into account the slope of the motor's mechanical characteristics and

Publisher: **KOMAG Institute of Mining Technology, Poland**

the electromagnetic and electromechanical time constants. This linearized model enables a relatively fast and efficient simulation of the dynamic waveforms for the purpose of determining the optimum speed controller settings. More detailed but also much more computationally demanding simulation model of motor, converter and gearbox is covered in [15,16]. Such models can be useful for hardware-in-the loop simulation of the control system hardware and software [17]. A simplified block diagram of the whole system is presented in Fig. 2.

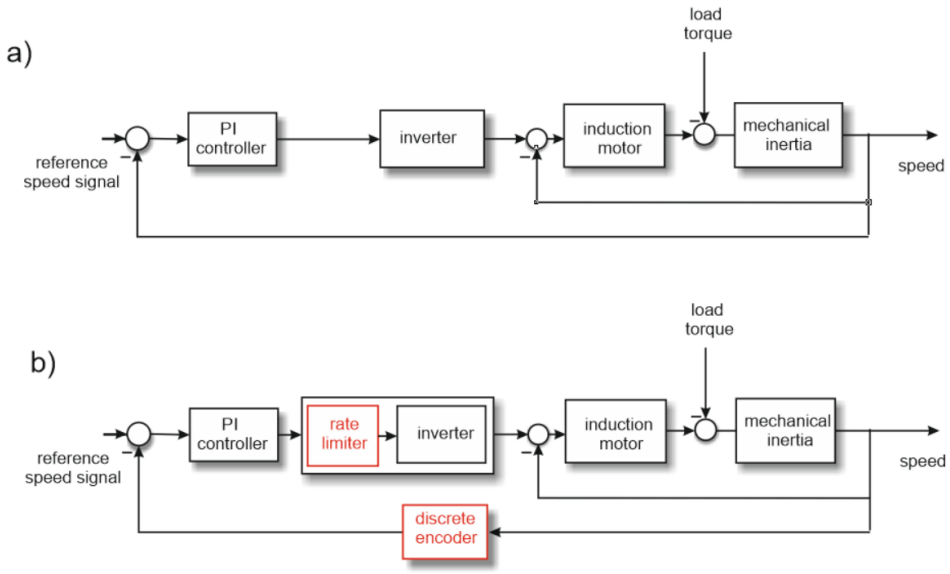

Fig. 2. General block diagram of the roadheader cutting head speed control system: a) simplified linearized model, b) linearized model with added nonlinear elements (marked in red)

Details of the diagram blocks from Fig. 2 (e.g. transfer function formulas, model coefficient values etc.) have been presented in [14].

The frequency converter can also be considered as a linear element with relatively low inertia and a delay of a few or several milliseconds, i.e. negligibly small in comparison with the inertia of the mechanical system (motor rotor, gearbox and cutting head). In this situation, one of the most important elements affecting the dynamics of the entire system is the input filter limiting the rate of the frequency change, mounted at the input of the inverter. The purpose of this filter is to limit the rate of change of the output frequency (and output voltage) of the inverter in order to avoid approaching (or even exceeding) the critical slip value and the associated current overload of the inverter transistors [18,19,20]. The influence of power supply frequency changes on induction motor torque is presented in Fig. 3. Such a rapid torque and current overload can cause the converter to shut down immediately and interrupt the drive system operation.

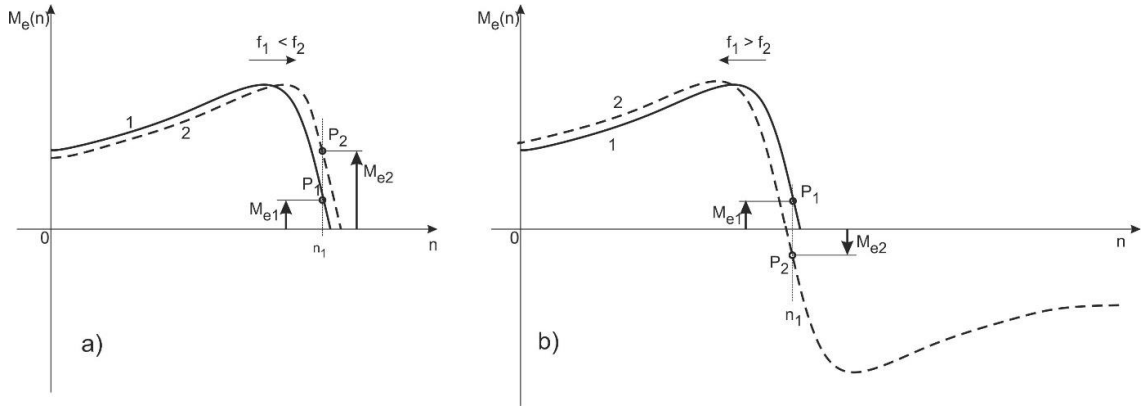

Fig. 3. Influence of power supply frequency changes on induction motor torque (M_{e1}, M_{e2} – torque values corresponding to operating points $P_1(f_1)$, $P_2(f_2)$ for different values of slip): a) at acceleration ($f_1 < f_2$), b) at deceleration ($f_1 > f_2$)

The rate-of-change limiter is a linear element in the static meaning (it carries the full range of frequency variation from zero to the rated frequency), but non-linear in the dynamic meaning (it allows slowly varying signals to pass unchanged, while limiting the variability of high-speed input signals). For an approximate analysis of the operation of a system with such an element, the harmonic linearization method (also known as the descriptive function method) can be used. In contrast to the well-known form of the descriptive function determined for elements with non-linear static characteristics, the form of the function describing dynamically non-linear elements is not reported in the relevant literature [21,22,23]. Its derivation is one of the issues addressed in this test.

The control system fitted to the laboratory stand used a rate limiter set by the inverter manufacturer to a value of $\alpha = 4$ Hz/sec. The signal passing through this limiter is deformed in terms of both amplitude (reduced) and phase (delayed). The principle of these constraints is shown in Fig. 4, and some examples of such variations are shown in Fig. 5.

Fig. 4. Rate-limiter of the input signal

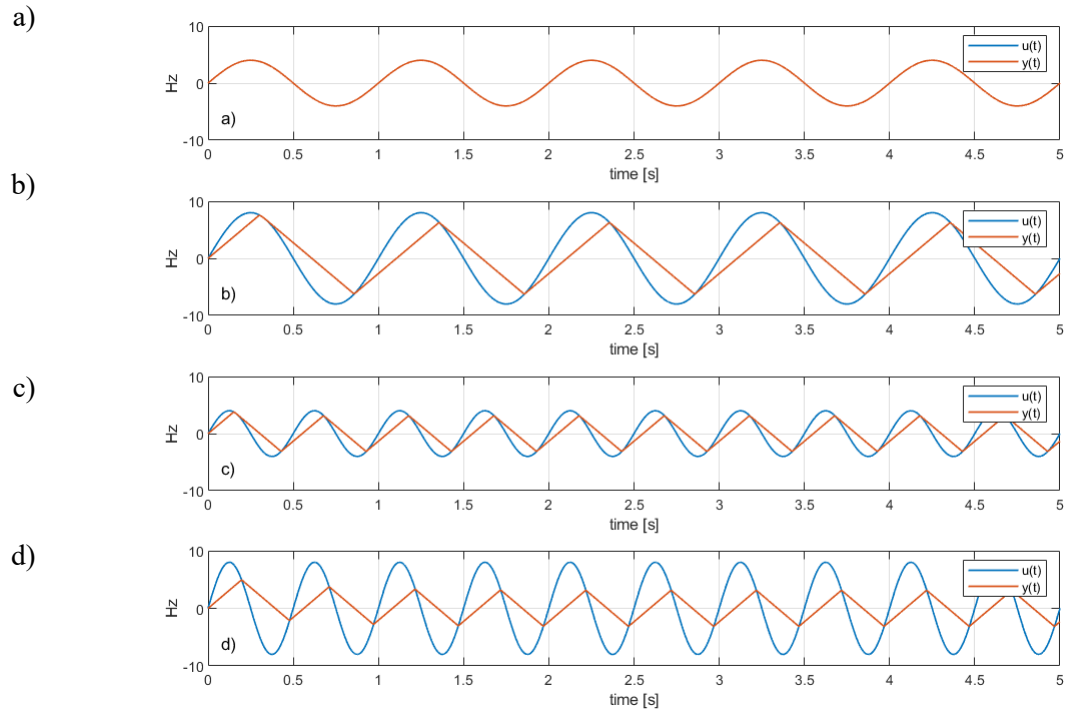

Fig. 5. Examples of the rate-limiter operation:
a) small magnitude, low frequency (no distortion), b) greater magnitude, low frequency,
c) small magnitude, higher frequency, d) higher magnitude, higher frequency

Quantitative analysis of this phenomenon can be carried out on the basis of the situation shown in Fig. 6 and the selected points of intersection of the sinusoidal (input) curve with the triangular (output) curve where α denotes a maximum permissible signal rate. This intersection point marks the peak of the triangular output waveform, so it can be used to compare against the peak of the input sinusoidal

waveform to determine both an amplitude and a phase shift of the triangular output waveform. The condtion of the intersection point can be stated as: $A \cdot \sin[\omega \cdot (t_u + \Delta t_u)]$

$$\underbrace{A \cdot \sin\left[\omega \cdot \left(t_u + \Delta t_u\right)\right]}_{u(t)} = \underbrace{\alpha \cdot \left(t_u + \Delta t_u\right) - \alpha \cdot \Delta t_u}_{y(t)} = \alpha \cdot t_u \tag{1}$$

where:

A – magnitude of the input signal,

ω– angular frequency of the input signal,

Δt_u – time interval between midpoint of the inaput of the waveforma and the intersection point,

t_u - a quarter of the input signal period,

α – maximum permissible rate of the input signal (straight-line directional coeffcient).

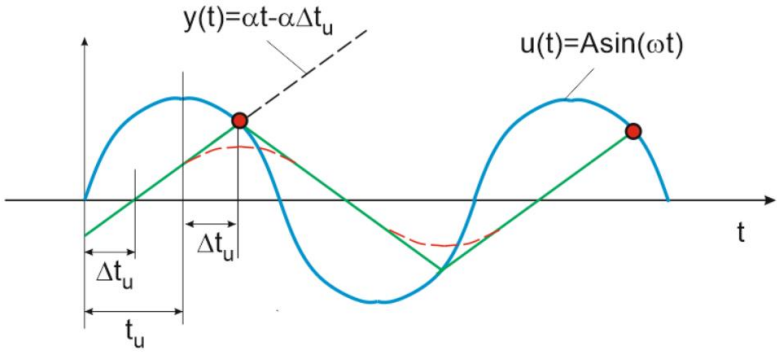

Fig. 6. Graphical analysis of the sinusoidal input waveform (blue) and the triangular output (green) waveforms and their intersection points. The red dashed waveform denotes first harmonic of the output triangular waveform

As the relationship between the time delay Δt_u and corresponding phase-shift φ can be written as:

$$\Delta t_u = \frac{\varphi}{\omega} \tag{2}$$

equation (1) can be stated as:

$$A \cdot \sin\left[\omega \cdot \left(\frac{\pi}{2\omega} + \frac{\varphi}{\omega}\right)\right] = \alpha \cdot \frac{\pi}{2\omega} \tag{3}$$

so:

$$\sin\left(\varphi + \frac{\pi}{2}\right) = \frac{\pi \cdot \alpha}{2\omega \cdot A} \tag{4}$$

and finally, the phase-shift can be expressed as:

$$\varphi(A, \omega) = \arcsin\left(\frac{\pi \cdot \alpha}{2\omega \cdot A}\right) - \frac{\pi}{2} \tag{5}$$

As any triangular function with peak value F and angular frequency ω can be decomposed into a Fourier series of the form [24,25,26]:

$$f(t) = \frac{8F}{\pi^2}\sin(\omega t) - \frac{8F}{(3\pi)^2}\sin(3\omega t) + \frac{8F}{(5\pi)^2}\sin(5\omega t) + ... \tag{6}$$

The peak value of the first harmonic of the triangular output function will therefore depend on both ω and α and will have a value of:

$$Y_m = \frac{8 \cdot (\alpha \cdot t_u)}{\pi^2} = \frac{8\alpha\left(\frac{\pi}{2\omega}\right)}{\pi^2} = \frac{4\alpha}{\omega\pi} \tag{7}$$

Therefore for a complex describing function $\underline{G}(A, j\omega)$ defined as:

$$\underline{G}(A, j\omega) = \frac{\underline{Y}(A, j\omega)}{\underline{U}(A, j\omega)} \tag{8}$$

the gain of the rate limiter calculated as the modulus (absolute value) of the function can be determined as:

$$\left|G(A, j\omega)\right| = \frac{Y_m}{A} = \frac{4\alpha}{\pi \cdot \omega \cdot A} \tag{9}$$

and the phase-shift is defined by eq. (5) as:

$$\varphi = Arg\{\underline{G}(A, j\omega)\} = \arcsin\left(\frac{\pi \cdot \alpha}{2 \cdot \omega \cdot A}\right) - \frac{\pi}{2} \tag{10}$$

Example graphs of $G(A, j\omega)$ function – both modulus (gain) and phase-shift are presented below in Fig. 7 for an example range of input signal peak values and frequencies. They are based respectively on equations (9) and (10). For small and slowly varying input signals the gain equals 1, and the phase shift is 0 – so the signal is not damped. If the input signal has greater magnitude or greater frequency, the gain decreases below 1 and simultaneously the phase delay increases.

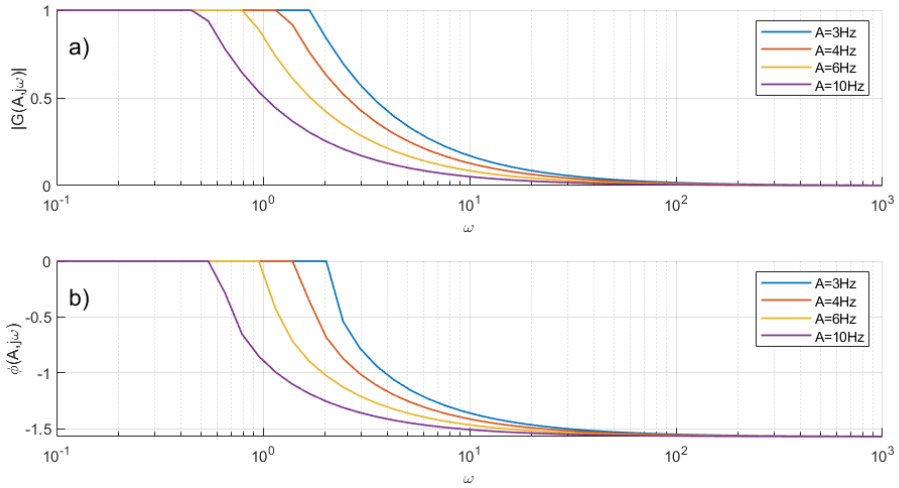

Fig. 7. Frequency input/output curves of the rate limiter (α=4Hz/s) calculated for an example range of input signal peak values: a) gain, b) phase shift

3. Results

The system has been extensively tested at the laboratory stand. There have been presented results of two typical, although qualitatively different tests. The waveform in Fig. 8. is characterized by a large variation of the signal generated by the higher-level reference setter. In this case, the primary task of the speed control system is to track these changes in the reference signal. It can be seen, however, that in many cases its response is too sluggish, which is related specifically to the limitation of the rate of frequency changes and the current overloads that occur during these changes.

Publisher: **KOMAG Institute of Mining Technology, Poland**

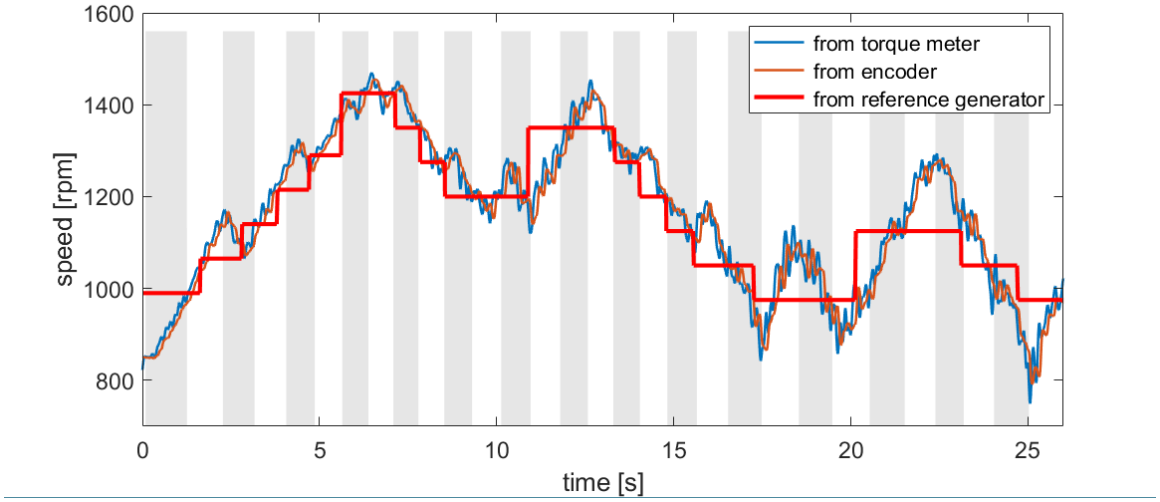

Fig. 8. Example waveform of rotational speed with high reference signal variability recorded at the laboratory stand

In the case of the waveform shown in Fig. 9, there is a distinctive long duration of steady-state operation (occurring after the end of the start-up period). The signal generated by the higher-level reference setter is then featured by a constant level for a longer period of time. Changes in cutting torque caused momentary changes in speed, but the control system maintained the average speed value at the set-point level. Thus, it can be assumed that the disturbances registered in the output signal waveform had the nature of stochastic noise, while the deterministic components have been well suppressed.

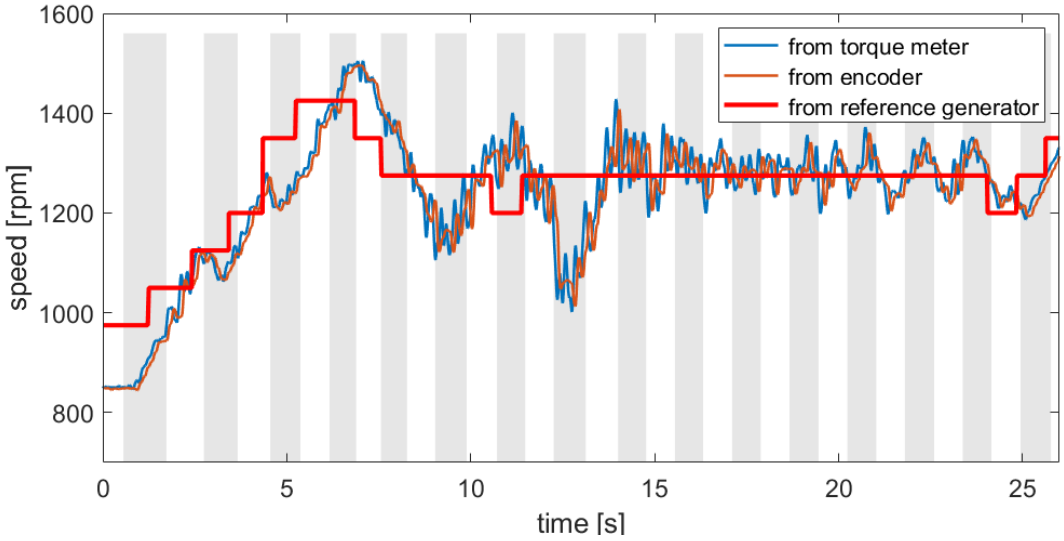

Fig. 9. Example waveform of rotational speed with longer period of constant value reference signal recorded at the laboratory stand

In both Fig. 8 and Fig. 9, there can be seen a small time shift between the speed measurement signals from the torque meter (continuous measurement) and the encoder (discrete measurement). The signal from the encoder is also smoother, which is due to the principle of its operation itself, since the encoder, instead of the instantaneous value, provides the average value of the speed calculated for one full period of rotation of the motor shaft. However, due to the much longer period of operation of the overriding load controller (resulting from the time of one full rotation of the cutting head), which acts as a speed setter, the relatively small delay described above (illustrated in detail by zooming in Fig. 10) does not significantly affect the quality and stability of the control system's operation.

Publisher: **KOMAG Institute of Mining Technology, Poland**

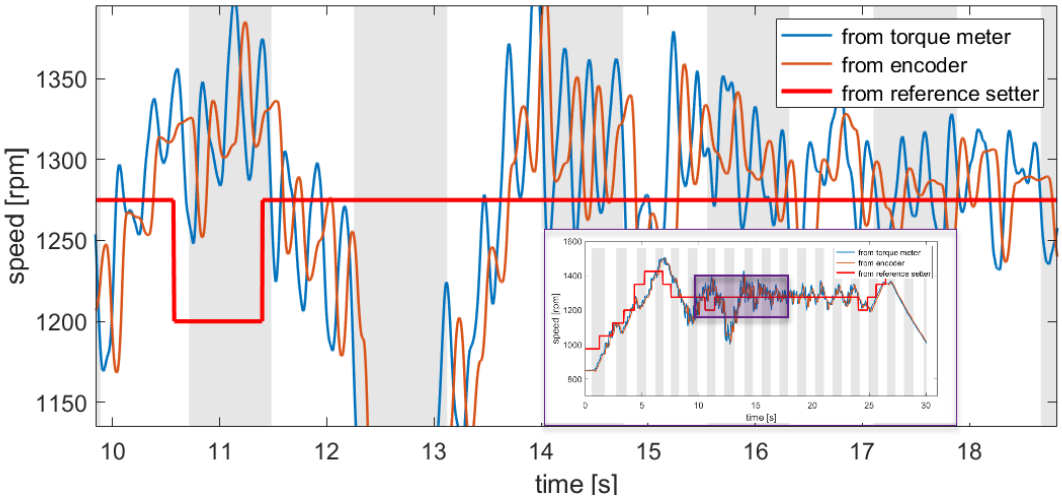

Fig. 10. Part of the recorded waveform from Fig. 8 zoomed in order to distinguish between continuous torque-meter and discrete encoder- based rotational speed signals

4. Conclusions

The PI controller settings determined by numerical optimization methods generally meet their purpose. Disturbances appearing in the system operation system are caused by the adoption of a simplified linearized motor model and the ignoring of additional linear and nonlinear feedback circuits occurring inside the frequency converter. Because of the inverter high thermal sensitivity even to short overloads, the rated power and rated current of the inverter must be greater than resulting from the motor parameters. Also, the internal frequency rate limiter on the input of the frequency converter has a deep impact on overall system dynamics and should be included in modelling, tuning and analysis of the roadheader and its control system model. The parameters of the motor model can also be affected by the change in resistance of the motor windings, caused by their heating during operation. Therefore, it seems purposeful to use other types of controllers - e.g. a robust controller with an internal model of the controlled drive. Slight improvement in following the reference speed signal can be also achieved by better (continuous and non-delayed) speed measurements.

Acknowledgements

The work has been implemented under the research project titled “Control of roadheader cutting heads movement for reduction of energy consumption of mining and dynamic loads“ co-financed by the Polish National Centre for Research and Development under the Applied Research Projects (Agreement No. PBS3/B2/15/2015).

References

[1] Deshmukh S., Raina A.K., Trivedi R.: Roadheader – A comprehensive review. Tunnelling and Underground Space Technology.Vol. 95, January 2020

[2] Jasiulek D., Świder J.: “Mechatronic systems in mining roadheaders – examples of solutions” PAR (Measurements, Automation, Robotics) vol. 17 no. 1, pp 121-127, 2013

[3] Cheluszka P., Remiorz E., Rostami J.: The Use of a Roadheader Simulator in Research of Dynamics and Energy-Consumption of Excavating Underground Roadways and Tunnels. Energies 2022, No15(18), 6673, DOI 10.3390/en15186673

[4] Torano J., Menendez M., Rodriguez R.: Experimental results of a low-power roadheader driving a gallery with .different types of rock at the face. Tunnelling and Underground Space Technology. Vol. 18, August 2003

[5] Tong M.: Kang D., Liu P.: Research on Automatic Section Cutting Control of Roadheader. IEEE

International Conference on Measuring Technology and Mechatronics Automation, 13-14 March 2010

[6] Liu X., Du Ch., Liu M.: Research on spiral angle optimization for longitudinal road header's cutting head. Proc IMechE Part C: J Mechanical Engineering Science 2020, Vol. 234(17) 3346–3359

[7] Chen H., Yang W., Ma Y.: Multi-sensor fusion method for roadheader pose detection, Mechatronics Vol. 80, December 2021

[8] Qi P, Chang J, Chen X, Wang T, Wu M.: Identification of Rock Properties of Rock Wall Cut by Roadheader Based on PSO-VMD-LSSVM. Frontiers in Earth Sci. May 2022, vol. 10

[9] Jasiulek D., Stankiewicz K., Swider J.: An adaptive control system of roadheader with intelligent modelling of mechanical features of mined rock. Journal of KONES Powertrain and Transport, Vol. 18, No. 2 2011

[10] Devy M., Orteu J.J., Mining robotics:: Application of computer vision to the automation of a roadheader. Robotics and Autonomous Systems 1993 Vol. 11

[11] Gao X.:Discussion on the remote visual control technology system of fully-mechanized heading face in mine. IOP Conference Series: Earth and Environmental Science, Vol. 508, Tianjin, 24-26th April 2020

[12] Salsani A., Daneshian J., Shariati S.: Predicting roadheader performance by using artificial neural network. Neural Computing and Applications, Vol. 24, No 7-8, June 2014

[13] Avunduk E., Tumac D., Atalay A.K.: Prediction of roadheader performance by artificial neural network. Tunnelling and Underground Space Technology, vol.44, September 2014

[14] Heyduk A., Joostberens J.: Automatic control of roadheader cutting head speed and load torque. 6th World Multidisciplinary Earth Sciences Symposium (WMESS 2020), 7-11 September 2020, Prague, Czech Republ. IOP Conference Series Earth and Environmental Science, December 2020

[15] Cheluszka P., Kaula R., Heyduk A. and Gawlik J.:Modelling the dynamics of a drive of boom-type roadheader cutting heads at adjustable angular speed. Arch. Mining Sci. vol. 63, pp. 183-204, 2018

[16] Heyduk A., Joostberens J.: Computer simulation of the roadheader cutting head speed control system. 18th International Multidisciplinary Scientific GeoConference: SGEM 2018, 2 July - 8 July 2018, Albena, Bulgaria. Conference proceedings, International Multidisciplinary Scientific GeoConference & EXPO SGEM, 2018, Sofia, STEF92 Technology

[17] Heyduk A., Joostberens J.: Hardware-in-the-Loop simulation applied to roadheader cutting head speed control system testing. Mining - Informatics Automation and Electrical Engineering 4 (532), January 2017.

[18] Jufer M.: Electric Drives: Design Methodology. Wiley-ISTE 2010

[19] Krause P., Wasynczuk P., Sudhoff S,C.: Analysis of Electric Machinery and Drive Systems. IEEE Press Wiley, 3rd Ed. 2013

[20] Razik H.: Handbook of Asynchronous Machines with Variable Speed. Wiley ISTE, London 2011

[21] Gelb A., Vander W E.: Multiple-Input Describing Functions and Nonlinear System Design. McGraw-Hill, 1968

[22] Aguilar L.T.:, Boiko I., Fridman L., Iriarte R: Self-Oscillations in Dynamic Systems: A New Methodology via Two-Relay Controllers. Birkhäuser Basel, 2015

[23] Lurie B., Enright P.: Classical Feedback Control with Nonlinear Multi-Loop Systems: With MATLAB® and Simulink®. Taylor Francis CRC Press, Boca Raton 2020

[24] Dyke P. An Introduction to Laplace Transforms and Fourier Series. Springer London, Heidelberg, 2nd ed. 2017

[25] Hsu T.: Fourier Series, Fourier Transforms, and Function Spaces. A Second Course in Analysis. AMS MAA Press, Providence 2020

[26] Serov V.: Fourier series, Fourier transform and their applications to mathematical physics. Springer London, Heidelberg, 2017

Publisher: **KOMAG Institute of Mining Technology, Poland**